

THEORETICAL STUDIES OF UNCONVENTIONAL
SUPERCONDUCTIVITY IN Sr_2RuO_4 AND RELATED
SYSTEMS

THEORETICAL STUDIES OF UNCONVENTIONAL
SUPERCONDUCTIVITY IN Sr_2RuO_4 AND RELATED
SYSTEMS

By Xin Wang, M.Sc

*A Thesis Submitted to the School of Graduate Studies in the Partial
Fulfillment of the Requirements for the Degree Doctor of Philosophy*

McMaster University © Copyright by Xin Wang November 21,
2022

McMaster University
Doctor of Philosophy (2022)
Hamilton, Ontario (Department of Physics and Astronomy)

TITLE: Theoretical studies of unconventional superconductivity in Sr_2RuO_4 and related systems

AUTHOR: Xin Wang (McMaster University)

SUPERVISOR: Dr. Catherine Kallin

NUMBER OF PAGES: ix, 95

Abstract

In this thesis, we study the unconventional superconductivity in Sr_2RuO_4 (SRO) and related systems. The superconducting state in SRO remains a puzzle after more than 28 years of study. Early experiments had pointed toward a topological non-trivial time-reversal symmetry breaking (TRSB) chiral p -wave order. This pairing candidate has attracted a large amount of attention, partly in relation to the possibility of topological quantum computation, and has stimulated studies on higher chirality superconducting systems. In the first part of this thesis, we study the spontaneous edge current in chiral d - and f -wave superconductors. We show that these currents, which vanish in the continuum limit at zero temperature, are generally non-vanishing but tiny, compared to the simplest chiral p -wave case. In the presence of strong surface roughness, the direction of the edge current in the chiral d -wave case can be reversed, compared with that of a specular ideal surface with specular scattering. However, it is shown that this current reversal is non-universal beyond the continuum limit.

The chiral p -wave scenario in SRO is overturned by recent Knight shift measurements, highlighting the importance of exploring different pairing symmetries for SRO. Recently, $d_{x^2-y^2} \pm ig_{x^2-y^2(xy)}$, $s' \pm id_{xy}$ and mixed helical p -wave pairings have been proposed as order parameter candidates. However, the stability of these states, especially of the $d_{x^2-y^2} \pm ig$ pairing, remains unclear. In the second part of the thesis, we study the leading superconducting instabilities in SRO in the presence of sizable atomic spin-orbit coupling (SOC), non-local SOC, and non-local interactions. We find that it is difficult to stabilize chiral p -wave pairing in SRO models; this is because, among the triplet p -wave states, the atomic SOC favors helical states over the chiral state. The presence of both $d_{x^2-y^2}$ - and g -wave pairings, including a $d_{x^2-y^2} \pm ig$ state, is found when the second nearest neighbor (in-plane) repulsions, together with orbital-anisotropy of the non-local interactions and/or the B_{2g} channel non-local SOC are included. We further analyze the properties, such as nodal structures, in-plane field spin-susceptibility, and spontaneous edge current, of the realized $d_{x^2-y^2} \pm ig$ pairing and find that this state is more compatible with existing experimental measurements than the $s' \pm id_{xy}$ and the mixed helical p -wave proposals.

Acknowledgements

It is a pleasure to thank those who made this thesis possible.

I owe my deepest gratitude to my supervisor, Dr. Catherine Kallin. This thesis, more precisely my Ph.D., would not have been possible without her. She is always willing to share her deep physical insight and has always been extremely patient in providing critical guidance throughout the years. She taught me not only physics but also more importantly how to conduct quality research and write up and explain things clearly and simply. Her uncompromising style of research will have a long-lasting impact on my career. Beyond this, she offered me a lot of opportunities outside McMaster. I also want to thank her for her continuous support and encouragement during my difficult times. I feel honored and privileged to be her student.

I am indebted to my committee members, Dr. Sung-Sik Lee and Dr. Erik Sorensen, for their guidance throughout my Ph.D. and the inspiring discussions during my committee meetings. I am also grateful to my early mentors and my collaborators, Dr. Zhiqiang Wang, and Dr. Wen Huang. They patiently guided me through the early stage of my Ph.D.. They have given me many suggestions and have helped me in many aspects. It is my honor to thank Dr. Jinshan Wu, who brought me into the world of physics. His support lasts till this day, long after my departure from his group.

I would like to thank the many people with whom I discussed the related work and have benefited greatly from the discussion: Laimei Nie, Soshi Mizutani, Hank Chen, Anton Borissov, Gabriel Magill, Yipeng Cai, Hao Song, and Thomas Scaffidi.

Lastly but most importantly, I wish to thank my parents, Xiaoguo Wang and Xiuyan Ma, and my husband, Bin Xu, for their unconditional support and love.

Contents

Abstract	iii
Acknowledgements	iv
preface	ix
1 Introduction	1
1.1 Historical introduction	1
1.2 Chiral superconductivity and spontaneous edge currents	5
1.3 Spin-orbit coupling and pseudospin-triplet pairings	8
1.4 Accidentally degenerate $d_{x^2-y^2} + ig_{xy}(x^2-y^2)$ pairing in the presence of longer range interactions	10
1.5 Outline of this thesis	12
2 Experimental results on the superconducting state in SRO	13
2.1 Cooper pair spin state	13
2.2 Broken time-reversal symmetry	14
2.3 Discontinuity in elastic moduli across T_c	14
2.4 Uniaxial strain response of T_c	16
2.5 Nodal structures	17
2.6 Summary	18
3 Spontaneous edge current in higher chirality superconductors	19
3.1 Preface	19
3.2 Publication	20
4 Spin-orbit coupling and spin-triplet pairing symmetry in Sr_2RuO_4	31
4.1 Preface	31

4.2	Publication	32
5	Higher angular momentum pairing states in Sr_2RuO_4 in the presence of longer-range interactions	45
5.1	Preface	45
5.2	Publication	46
6	Conclusions	61
A	Quasiclassical Eilenberger theory	64
B	Ginzburg-Landau analysis of the SOC effect on triplet p-wave pairings	67
A1	GL free energy in the absence of SOC	67
A2	SOC induced GL free energy terms	68
C	RPA effective interaction in the presence of both local and longer-range interactions	71
A1	Coulomb interactions	71
A2	Spin susceptibility and effective interactions within RPA	73
A2.1	Tree diagram contribution	74
A2.2	Ladder diagrams	75
A2.3	Bubble diagrams	77
A2.4	Summary	77

List of Figures

1.1	Layered perovskite structure of SRO	3
1.2	Fermi surface of SRO	4
A3.1	Bare- U interaction diagram in the Cooper pair channel.	74
A3.2	The second and the third order ladder diagrams in the Cooper pair channel	76
A3.3	The second and the third order bubble diagrams in the Cooper pair channel	78

List of Tables

2.1	Irreps. of the D_{4h} point group	15
2.2	Consequence of (accidentally) degenerate pairings in ultrasound ex- periments	16

preface

This sandwich thesis consists of three publications as listed below:

- Chapter 3 X. Wang, Z. Wang, C. Kallin, *Spontaneous edge current in higher chirality superconductors*, Phys. Rev. B 98, 094501 (2018).
XW performed numerical calculations; ZW and XW conducted theoretical analyses; CK supervised the project. All authors discussed and wrote the manuscript.
- Chapter 4 Z. Wang, X. Wang, C. Kallin, *Spin-orbit coupling and spin-triplet pairing symmetry in Sr_2RuO_4* , Phys. Rev. B 101, 064507 (2020).
XW performed numerical calculations; ZW conducted theoretical analyses; CK supervised the project. All authors discussed and wrote the manuscript.
- Chapter 5 X. Wang, Z. Wang, C. Kallin, *Higher angular momentum pairing states in Sr_2RuO_4 in the presence of longer-range interactions*, Phys. Rev. B 106, 134512 (2022).
XW performed all the calculations; XW and ZW carried out the RPA formalism; CK supervised the project. XW wrote the draft, and CK and ZW provided suggestions and edits for the final manuscript.

Chapter 1

Introduction

1.1 Historical introduction

Superconductivity has been one of the most extensively studied quantum mechanical phenomena in condensed matter physics since its discovery in 1911 by Kamerlingh-Onnes, who observed the resistivity of mercury becoming unmeasurably small below temperatures of $4.2K$. [1] Subsequently, superconductivity was shown to appear in a wide range of metals. [2] However, there was no satisfactory microscopic theory of this phenomenon until the advent of the celebrated Bardeen-Schrieffer-Cooper (BCS) theory in the 1950s. [3]

In the BCS theory, superconductivity is a condensate of electron pairs, called Cooper pairs, which form due to even a weak attraction among electrons close to the Fermi surface. [4] In the particular model that BCS solved, the attraction is mediated by electron-phonon coupling and the resulting Cooper pairs are in a spin-singlet state with vanishing relative orbital angular momentum, i.e. an *s*-wave pairing state. [3] This theory particularly successfully described the properties of superconductors discovered at that time, commonly known as *conventional* superconductors.

Since the 1970s, several systems have been discovered to exhibit Cooper pairing beyond the original BCS description, i.e. *unconventional* Cooper pairing. The discovery of superfluidity in ^3He in 1971 provided the first example and started the era of unconventional superconductivity. [5, 6] The pairing state in liquid ^3He

is in a spin-triplet state with relative angular momentum 1, called the p -wave state. Its pairing mechanism is non-phononic, arising from van der Waals and spin-fluctuations mediated interactions. [6, 7] Many unconventional superconductors have since been discovered. Particularly, the discovery of high-temperature (high- T_c) superconductivity in cuprate compounds in the 1980s [8] popularised the field of unconventional superconductivity. Later, the Cooper pair wave function in the cuprates was found to have $d_{x^2-y^2}$ -wave symmetry. [9, 10, 11]

It is believed that electron-electron interactions play an essential role in stabilizing the higher angular momentum pairings. [12, 13, 14] Electrons in metals interact primarily by the Coulomb interaction, which is repulsive at short distances but can be attractive at longer distances. [14] In principle, the p -, d -, or f - wave pairing with higher angular momentum can exist since their wave functions vanish at short distances, evading the short-distance repulsion. The exact mechanism for superconductivity originating from the Coulomb interaction can be rather complex. To date, no controlled many-body perturbation method (beyond infinitesimal interaction strength [15]) has been developed to address this issue. [16]

In this thesis, we will study an actual example of unconventional superconductors, Sr_2RuO_4 (SRO). Superconductivity in this material was discovered by Maeno *et al* in 1994. [17] Since then, it has been subjected to extensive experimental and theoretical studies. Therefore, in the following, we will aim to review a limited subset of the literature. For more detailed reviews, one can refer to Refs. [19, 20, 18, 21, 22, 23, 24, 25, 26, 27, 28].

SRO has the same layered perovskite structure as some of the cuprates (in Fig. 1.1), but it is quite distinct from the cuprates in both the normal and the superconducting states. [18] In many respects, SRO is an ideal testbed for microscopic theories of unconventional superconductivity. SRO behaves like a Fermi liquid below about 30K , but with considerable mass and susceptibility enhancements, indicating strong electron correlations. [18] The SRO samples are extremely clean, so the complicating factors associated with disorder or doping can often be ignored in theoretical and experimental studies. Also, because such high-quality single crystals are available, [29] the normal state Fermi liquid and Fermi surface (FS) sheets

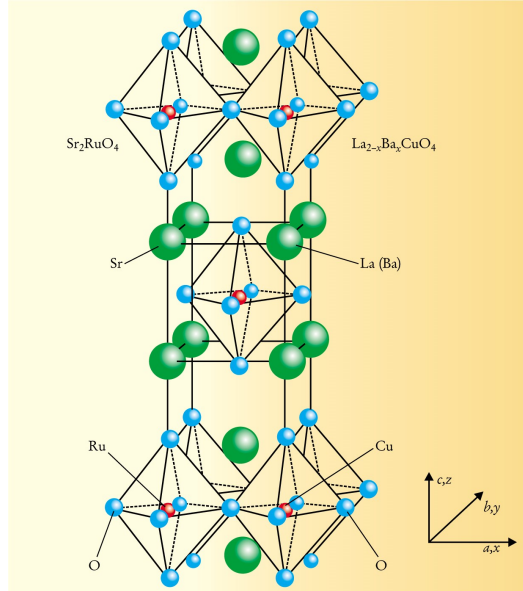


FIGURE 1.1: Layered perovskite structure of SRO and the high- T_c family $\text{La}_{2-x}\text{Ba}_x\text{CuO}_4$. Adapted from [Y. Maeno, T. M. Rice, and M. Sigrist, *Physics Today* **54**, 1, 42 (2001)], with the permission of the American Institute of Physics.

are characterized with unprecedented accuracy and precision. [30, 31, 20, 32, 18] SRO becomes superconducting below 1.5K with a mean-field, BCS-like transition. [18] The transition temperature, T_c , is extremely sensitive to non-magnetic impurities, as expected for unconventional superconductivity where the superconducting gap averages to zero around the FS. [33, 18] These have led to the widespread belief that SRO is soluble within the capacity of established theoretical frameworks and experimental techniques. Nevertheless, despite tremendous efforts over the past 28 years, an order parameter (OP) compatible with all the key experimental observations is still lacking.

Indeed, many experiments appear to infer contradictory conclusions regarding the pairing symmetry in SRO. For example, broken time-reversal symmetry (TRS) in the superconducting state has been observed in multiple experiments, [34, 35, 36] however, direct searches for the spontaneous edge currents expected in a broken TRS superconducting state (discussed below) all return null results. [37, 38, 39, 40] Also, the evidence of a two-component superconducting OP (discussed in Chap.2), [34, 35, 41, 42, 43, 44] is challenging to reconcile with the

absence of splitting in the superconducting transition temperature in specific heat measurements under uniaxial strain [45]. These contradictions pose challenges for both theorists and experimentalists.

Another feature that complicates theoretical studies for SRO is its multi-orbital nature. SRO has three FS sheets (shown in Fig.1.2), which are highly two-dimensional, reflecting the large anisotropy of this material. [18] Among them, the quasi-two-dimensional (2D) band, labelled as the γ -band, arises primarily from Ru d_{xy} orbitals, whereas the d_{xz} and d_{yz} orbitals form two quasi-1D bands which hybridize to give the α and β bands. [30] The presence of sizable spin-orbit coupling (SOC), which entangles the three orbital degrees of freedom with spin [46, 47, 48, 49, 50, 32, 51, 52], further complicates the microscopic analysis.

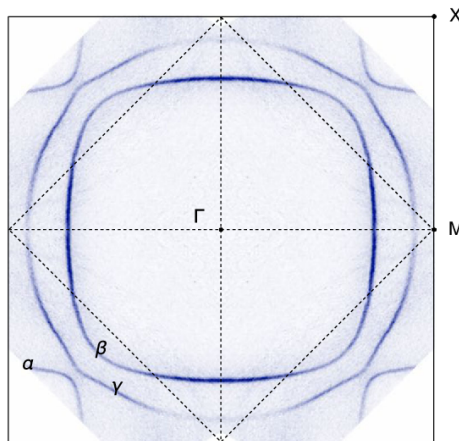


FIGURE 1.2: The three sheets of the FS of SRO, labeled α , β and γ , are shown in the ab plane from high-resolution ARPES measurements. Figure adapted from [A. Tamai et al., Phys. Rev. X 9, 021048 (2019)] under the terms of the Creative Commons Attribution 4.0 International license.

1.2 Chiral superconductivity and spontaneous edge currents

Shortly after the discovery of superconductivity in SRO, it was proposed that the material has a spin-triplet odd-parity p -wave pairing that is a 2D analog of one of the pairing states in superfluid ^3He . [53, 54] Evidence of this proposal came first in nuclear magnetic resonance (NMR) Knight shift measurements [55, 56] and separately in a polarized neutron scattering measurement [57], which both suggested an unchanged in-plane field spin susceptibility below T_c . The absence of a drop in the spin susceptibility points to spin-triplet pairing.[6] The odd-parity feature was later supported by a Josephson interference measurement. [58] These observations, combined with the further reports of broken TRS in the superconducting state in muon spin relaxation (μSR) [34] and polar Kerr effect[35] measurements, point toward chiral p -wave, $p_x \pm ip_y$, order in SRO. The “ \pm ” in the chiral order corresponds to two degenerate chiralities.

A chiral $p_x \pm ip_y$ pairing has several striking properties. [59] It spontaneously breaks TRS due to the fact that its Cooper pairs carry nonzero angular momentum $L_z = \pm\hbar$, where \hbar is Planck’s constant. This topologically non-trivial state supports localized states at the sample edges which are robust against local perturbations since they are protected by the topology of the bulk gap. The existence of the edge modes leads naturally to the expectation of spontaneous edge currents, the direction of which typically depends on the sign of chirality. [60] As a triplet superconductor, additional exotic properties arise from the spin degrees of freedom (the spin structures are discussed in more detail below), including, for example, half-quantum vortices (HQVs). [6, 59] These HQVs support zero-energy Majorana modes at vortex cores. [59] The HQV-Majorana mode composites obey non-Abelian braiding statistics when moved around each other [61] which has attracted great interest for its potential applications in quantum computing [62]. (For more details, one can refer to Refs. [59, 25] and references therein.)

There are other materials that could potentially exhibit chiral superconductivity besides SRO. SrPtAs [63] and doped Graphene [64] are two examples for possible chiral d -wave superconductors. Recently, UTe_2 has been proposed to be a 3D chiral

triplet superconductor. [65] Other uranium-based heavy fermion compounds, such as URu₂Si₂ and UPt₃, may also support 3D chiral superconductivity with higher angular momentum. [25].

Given how highly anisotropic SRO is, 2D models are commonly employed to describe its electronic and superconducting properties. In the continuum limit, the orbital part of the superconducting gap function of a 2D chiral superconductor is described as,

$$\Delta_{\mathbf{k}} = \Delta_0 \left(\frac{k_x \pm ik_y}{k_F} \right)^{|m|} = \Delta_0 \left(\frac{k}{k_F} \right)^{|m|} e^{im\theta_{\mathbf{k}}}, \quad (1.1)$$

where m denotes the orbital angular momentum of the Cooper pairs, e.g. $m = \pm 1, \pm 2$, and ± 3 for chiral p -, d -, and f -wave superconductors, respectively. Δ_0 is the magnitude of the gap, $\theta_{\mathbf{k}}$ is the angle of wavevector \mathbf{k} with respect to the x -axis and k_F is the Fermi wavevector. The quantized orbital angular momentum m coincides with the Chern number, C , a topological number given by the winding of the chiral OP around the FS [66, 67]:

$$C \equiv \frac{1}{4\pi} \int d^2k \hat{\mathbf{h}} \cdot (\partial_{k_x} \hat{\mathbf{h}} \times \partial_{k_y} \hat{\mathbf{h}}) = m, \quad (1.2)$$

where $\mathbf{h} = (\text{Re}[\Delta(\mathbf{k})], -\text{Im}[\Delta(\mathbf{k})], \epsilon(k) - \mu)$ and $\hat{\mathbf{h}} = \mathbf{h}/|\mathbf{h}|$, with $\epsilon(k) - \mu$ the normal state single-particle dispersion relative to the chemical potential, μ . The sign of the Chern number depends on the chirality and the sign of the charge carriers.

The Chern number counts the number of chiral edge modes in a chiral superconductor. [68, 69] A direct consequence of these edge modes is the spontaneous edge current. However, the chiral edge current itself is not topologically protected and can strongly depend on microscopic details [68, 69, 70, 71, 72], since charge is not conserved in a superconducting state. Furthermore, the bulk states also contribute to the edge current.[60]

For the simple chiral p -wave order and a single isotropic conduction band, the edge current is substantial [73, 60, 74]. Neglecting screening effects, the total edge current, which is localized within a coherence length of the edge, is given by $J^{\text{tot}} = eE_F/4\pi$, where e is the electron charge, $E_F = k_F^2/2m^*$ in the continuum

limit and m^* is the fermion mass. [60, 74, 68, 69] This result is consistent with the prediction of a macroscopic angular momentum of $\langle L_z^{\text{tot}} \rangle = N\hbar/2$, for N electrons. [60] The substantial edge current would be screened by diamagnetic screening currents with different length scales, generating spatially varying magnetic fields. [75] These magnetic fields are expected to be detected by high-sensitivity magnetic scanning microscopy experiments, [76] but direct searches for them have all returned null results and have placed a strict upper bound on their magnitude that is about three orders of magnitude smaller than the simplest chiral p -wave prediction. [37, 38, 39, 40] Over the years, a significant amount of work has attempted to reconcile the chiral p -wave order with the absence of edge currents in SRO. Finite temperature [60, 74], gap anisotropy [77, 69], surface disorder [78, 79] and other surface effects [80, 81, 82, 77] have been raised for reductions in the current.

In contrast to the chiral p -wave case, the edge currents in higher chirality superconductors are less studied. In the absence of Meissner screening, Refs. [68, 69] showed that the total currents of the higher chirality superconductors vanish in the semiclassical continuum limit at zero temperature, $T = 0$. On the other hand, Ref. [83] found a non-zero current for chiral d -wave in the presence of surface roughness and also noted that the direction of the current flow was reversed compared to the specular surface case.

In Chapter 3, we study the effects of finite temperature, Meissner screening, and surface roughness on edge currents in 2D chiral d - and f - wave superconductors within the quasi-classical approximation. We show that the total edge currents in the higher chirality superconductors are non-zero at finite T or with rough surfaces, although they may vanish at $T = 0$ with a specular surface. We also show that the current reversal observed in Ref.[83] in the presence of surface roughness is non-universal beyond the continuum limit.

Our results can be extended to 3D chiral superconductors since the total edge current depends only on the projection of the Cooper pair relative orbital angular momentum L_z . [68, 72] For example, the edge current for the 3D chiral d -wave state, $k_z(k_x \pm ik_y)$, is closely related to the chiral p -wave case in 2D.

1.3 Spin-orbit coupling and pseudospin-triplet pairings

Although multiple early experiments point toward chiral p -wave order in SRO, this state is difficult to reconcile with several other experiments. A prominent example is the absence of spontaneous edge current that has been discussed in Sec. 1.2. Also, splitting of the superconducting transition temperature, T_c , in the presence of an in-plane magnetic field or a uniaxial strain [84, 85, 86] is expected but not found. Furthermore, the in-plane upper critical field appears to be Pauli-limited, [87] which is not expected for triplet pairing, as one has with chiral p -wave. [88, 89, 90, 91] While some of these discrepancies can be explained within the chiral p -wave framework by invoking microscopic details or sample imperfection, this proposal is strongly challenged by recent revised Knight shift measurements [92, 93, 94]. In contrast to previous measurements [55], a substantial spin susceptibility drop in the presence of an in-plane field in the superconducting state is reported and is further confirmed by a polarized neutron scattering study [95]. This observation rules out chiral p -wave order, and reopens the debate regarding the symmetry of the superconducting OP in SRO. [27, 28, 96, 97, 98]

Which of the triplet states is more favorable in SRO had been a long-standing and unanswered question. By convention, a triplet OP can be described by a \mathbf{d} -vector as, [99]

$$\hat{\Delta}(\mathbf{k}) = \begin{pmatrix} \Delta_{\uparrow\uparrow} & \Delta_{\uparrow\downarrow} \\ \Delta_{\downarrow\uparrow} & \Delta_{\downarrow\downarrow} \end{pmatrix} = \begin{pmatrix} -d_x(\mathbf{k}) + id_y(\mathbf{k}) & d_z(\mathbf{k}) \\ d_z(\mathbf{k}) & d_x(\mathbf{k}) + id_y(\mathbf{k}) \end{pmatrix}, \quad (1.3)$$

where

$$\mathbf{d}(\mathbf{k}) = \frac{1}{2}(\Delta_{\downarrow\downarrow} - \Delta_{\uparrow\uparrow}, -i(\Delta_{\downarrow\downarrow} + \Delta_{\uparrow\uparrow}), \Delta_{\uparrow\downarrow} + \Delta_{\downarrow\uparrow}). \quad (1.4)$$

$\Delta_{ss'}(k)$ is the OP with spin indices s and s' . The Pauli exclusion principle necessarily implies odd parity for the spatial wave function of a triplet Cooper pair, i.e. $\mathbf{d}(\mathbf{k}) = -\mathbf{d}(-\mathbf{k})$. The direction of the \mathbf{d} -vector denotes the direction along which the spin of the Cooper pair state has zero spin projection.

In conjunction with the tetragonal crystal lattice structure of SRO, the \mathbf{d} -vector

has to belong to one of the five odd-parity irreducible representations (irreps.) of the underlying D_{4h} point group as shown in the last five rows in Table. 2.1. The odd-parity irreps. can be split into two groups. The four 1D irreps. give helical pairings with in-plane $\mathbf{d}(\mathbf{k})$ and do not break TRS; the 2D irrep. supports two chiral states $\hat{z}(k_x \pm ik_y)$ with out-of-plane $\mathbf{d}(\mathbf{k})$ and spontaneously broken TRS.

In the absence of SOC, and in the weak-coupling limit, all these helical and chiral p -wave states are degenerate since spin rotation symmetry is preserved. [100] The \mathbf{d} -vector could be the linear combination of all these states, allowing it to rotate freely. The degeneracy can be lifted through the spin fluctuation feedback effect due to the superconducting condensate or through the normal state SOC effect. The feedback effect has been used to stabilize the ^3He A phase [6]. However, this effect is subdominant in SRO since it only appears at fourth-order terms in a Ginzburg-Landau free energy expansion, while the SOC effect can split T_c s at quadratic order [100]

How SOC pins the \mathbf{d} -vector, thereby favoring one of the triplet states in SRO, has been investigated previously in Refs. [100, 101, 102, 103, 46, 104, 48, 105, 51, 106, 107, 108], but is not fully understood. There are also conflicting statements regarding the degeneracy among different p -wave pairing states. For example, Annett *et al.*[46], using a mean-field approach, showed that the chiral p -wave state is unlikely to be stabilized, since $\langle \mathbf{L} \cdot \mathbf{S} \rangle = 0$, unless spin-dependent pairing interactions are included. Yanase *et al.*[103], pointed out that SOC itself is insufficient to lift the degeneracy. They stabilized the chiral p -wave order by solving Eliashberg equations only for the γ band. Scaffidi *et al.*[51] found that chiral p -wave, helical p -wave, or a singlet state is favored depending on the details of the interactions using a weak-coupling renormalization group (RG) analysis. This work differs in some conclusions from the mean-field analysis of Ref. [46]. Furthermore, the weak-coupling RG analysis of Ref. [51] gives comparable gaps on all three bands, unlike in Ref. [103].

In Chapter 4, we present a complete analysis to address this issue. We show that chiral p -wave pairing is difficult to stabilize in SRO models; while helical states are generally dominant over chiral. As a result, accidentally degenerate helical states can be stabilized. Such pairings are recently proposed by Huang

et al.[96] from a phenomenological analysis to explain several key observations in SRO, including the intrinsic Hall and Kerr effects [59], the absence of spontaneous edge currents [37, 38, 39, 40], and the substantial Knight shift drop [92, 93, 94]. In Chap. 5, we further study the properties of the realized mixed helical state, to see if it can be reconciled with the experiments.

In the above discussion, spin has been discussed as a good quantum number. However, this is not the case in the presence of SOC. It is always possible to define a pseudospin and classify a pairing state into a pseudospin singlet or triplet pairing state due to the preserved time-reversal and inversion symmetries, which ensure a twofold degeneracy at each \mathbf{k} point in the Brillouin zone (BZ). [109, 52] In most circumstances, one can transfer to the pseudospin settings by replacing spin with pseudospin. For the sake of simplicity, we often drop the (pseudo)spin and call (pseudo)spin singlet/triplet pairings as singlet/triplet pairings.

1.4 Accidentally degenerate $d_{x^2-y^2} + ig_{xy}(x^2-y^2)$ pairing in the presence of longer range interactions

Recently, the debate regarding the symmetry of the superconducting OP in SRO has substantially heated up since the chiral p -wave scenario, which has been dominant in the past two decades, is ruled out by the revised Knight shift measurements. [92, 93, 94] However, identifying the pairing symmetry in SRO is rather challenging, as there have been a large number of experiments on the superconducting state in SRO, and some observations seem contradictory. [23, 26, 27, 28] It is possible that some observations may have an alternative interpretation or may be due to extrinsic effects. One practical strategy is to focus on a subset of experiments with clear implications and reconcile as many of them as possible. In Chap. 2, we briefly introduce some experiments in this subset that are relevant to determining the superconducting OP in SRO.

Recently, an accidentally degenerate $d_{x^2-y^2} \pm ig_{xy}(x^2-y^2)$ pairing was proposed from a phenomenological standpoint [27, 110] to account for a wide variety of the

experimental results for SRO. For example, a $d_{x^2-y^2} + ig$ pairing state spontaneously breaks TRS [34, 35, 36] and has symmetry-protected vertical line nodes in the (1,1,0) direction that are consistent with the experimental observations in Refs. [111, 112, 113]. It is also compatible with the observed discontinuity in the c_{66} elastic modulus [42, 43], NMR Knight shift measurements data [92, 93, 94], neutron scattering data [114] and splitting of superconducting and TRSB transitions under uniaxial strain [44].

However, the settlement of this proposal seems delicate in many aspects. First, this pairing state, as well as all other proposals with coexisting OP components associated with two distinct 1D irreps. in D_{4h} point group (in Table. 2.1), requires fine-tuning so that $T_c \approx T_{\text{trsb}}$. A recent study [115] shows that this requirement can be somewhat relaxed by considering inhomogeneous states, where, for example, the second OP is induced by inhomogeneous strains near dislocations. In addition, such inhomogeneous states [116, 115] may provide a route to explain the observation of HQVs [117] and the absence of a measurable heat capacity anomaly at the TRSB transition [45].

The second concern lies in the stability of the g -wave component. The $d_{x^2-y^2}$ state is found to be stable in previous studies of SRO models with on-site Coulomb interactions using different approaches, including the asymptotically exact weak-coupling RG [51, 106, 108, 52], random phase approximation (RPA) [106, 107, 52, 118, 119], and functional RG approach [120, 121]. However, no previous study of SRO has found the g -wave state. This is because g -wave pairing has a quite high angular momentum. For example, within a single band model on a 2D square lattice, g -wave pairing wave functions are non-vanishing only at distances longer than the third-neighbour sites. [122]

Thus, the most vexing question for this scenario is how these two symmetry-distinct components can be near degenerate without the need for fine-tuning to form a homogeneous or inhomogeneous TRSB OP. In Chap.5, we study the key effects that stabilize both $d_{x^2-y^2}$ and g -wave, including the $d_{x^2-y^2} + ig$ pairing. We show that non-local Coulomb repulsions and non-local SOC with B_{2g} symmetry are crucial to stabilizing the $d_{x^2-y^2} + ig$ pairing. We further analyze the properties, including nodal structures, spin susceptibility, and spontaneous edge current, of

the realized $d_{x^2-y^2} + ig$ state, and find that this state is in better agreement with the experiments than the realized $s' + id_{xy}$, and mixed helical pairings.

1.5 Outline of this thesis

The remainder of this thesis is organized as follows. In Chap.2, we briefly introduce some important experimental measurements on SRO and their interpretations. In Chap.3, we focus on 2D higher chirality superconductors in the continuum limit and study the spontaneous edge current in these systems in the presence of finite temperature, Meissner screening, and surface roughness effects. In Chap.4 and Chap.5, we focus on the pairing mechanism and pairing symmetry in SRO. How SOC lifts the degeneracy among different triplet p -wave pairing states is analyzed in Chap.4. The stability and the properties of $d_{x^2-y^2} + ig$ pairing in the presence of longer-range interactions are discussed in Chap.5. In Chap.6, we provide some general conclusions and outlook for future related work. Finally, some details are left to the appendices, including the quasiclassical Eilenberger formalism for chiral superconductors in App.A, the Ginzburg-Landau analysis of the SOC effect on triplet p -wave states in App.B and the derivation of the RPA effective interaction in the Cooper pairing channel in the presence of both local and longer-range interactions in App.C.

Chapter 2

Experimental results on the superconducting state in SRO

This chapter briefly discusses some key experiments on the superconducting state of SRO and their interpretations. For more detailed reviews, one can refer to Refs. [23, 26, 27, 28].

2.1 Cooper pair spin state

The spin structure of a Cooper pair can be distinguished by spin susceptibility measurements. [123] In a singlet superconductor, the spin susceptibility, χ , drops as the temperature is lowered through T_c for any direction of the applied field, whereas, for a triplet superconductor, it drops if the applied field is parallel to the direction of zero-spin projection of the Cooper pairs. More specifically, in the absence of SOC and with a single band, the residual in-plane spin susceptibility, $\chi(T = 0)/\chi_n$, is 0 for singlet states; while it is 1/2 for helical states and 1 for chiral states. [123] Although there is no experiment that measures χ directly and quantitatively, the Knight shift measurements in NMR experiments can give us information on the behavior of $\chi(T)$.

The revised NMR Knight shift measurements [92, 93] report a significant in-plane Knight shift drop below T_c . This implies a substantial drop of in-plane χ which rules out chiral p -wave order. Ref. [94] further estimates the upper bound for the residual is $\chi(T = 0)/\chi_n < 10\%$, a value that contradicts triplet pairings

of any sort. We also note that Refs. [28, 96] argue that the helical scenario is still viable in the sense that the exact temperature dependence of $\chi(T)/\chi_n$ is still unclear.

2.2 Broken time-reversal symmetry

Shortly after the discovery of superconductivity in SRO, evidence of TRSB in SRO was found in muon spin resonance (μ SR) experiments, where muon relaxation consistent with additional weak internal magnetic fields below T_c was observed.[34] Later, polar Kerr effect measurements observed a nonzero Kerr angle below T_c , providing strong and direct evidence for TRSB superconductivity.[35]. Further support comes from a Josephson interferometry measurement.[36].

The observations of TRSB superconductivity put a strong constraint on possible OPs: the OP has two degenerate components that presumably form a complex gap function. A multi-component pairing is realized if its two components belong to the 2D irreps. of the crystal point symmetry group (in Table 2.1), such as spin-triplet $p_x \pm ip_y$ pairing with E_u symmetry and spin-singlet $d_{xz} \pm id_{yz}$ pairing (E_g symmetry). Another possibility is coexisting OPs associated with distinct 1D irreps. (in Table 2.1), which usually requires fine-tuning.

Spontaneous equilibrium currents at the edges of the sample, in the absence of any externally applied fields, are generally expected due to the broken TRS. However, searches for the magnetic fields produced by the predicted edge currents have all returned null results [37, 38, 39, 40], as discussed in Sec.1.2 in Chap.1.

2.3 Discontinuity in elastic moduli across T_c

Measurements of changes in the elastic moduli near T_c using resonant ultrasound spectroscopy [42] provide symmetry-related constraints on possible OPs in SRO. Elastic moduli are second derivatives with respect to the strain, ϵ_T , of the thermodynamic free energy, \mathcal{F} : $c_T = \partial^2 \mathcal{F} / \partial \epsilon_T^2$. For a two-component superconducting OP: $\Delta = (\Delta_x, \Delta_y)$, the leading order coupling has the following form in the

irrep.	Basis function	dimension
A_{1g}	$d_0(\mathbf{k}) = 1, k_x^2 + k_y^2$	1
A_{2g}	$d_0(\mathbf{k}) = k_x^2 - k_y^2$	1
B_{1g}	$d_0(\mathbf{k}) = k_x k_y$	1
B_{2g}	$d_0(\mathbf{k}) = (k_x^2 - k_y^2)k_x k_y$	1
E_g	$d_0(\mathbf{k}) = k_z(k_x, k_y)$	2
A_{1u}	$\mathbf{d}(\mathbf{k}) = \hat{x}k_x + \hat{y}k_y$	1
A_{2u}	$\mathbf{d}(\mathbf{k}) = \hat{x}k_y - \hat{y}k_x$	1
B_{1u}	$\mathbf{d}(\mathbf{k}) = \hat{x}k_x - \hat{y}k_y$	1
B_{2u}	$\mathbf{d}(\mathbf{k}) = \hat{x}k_y + \hat{y}k_x$	1
E_u	$\mathbf{d}(\mathbf{k}) = \hat{z}(k_x, k_y)$	2

TABLE 2.1: Irreps. of the D_{4h} point group. Even-parity representations (subscript g) are described by a scalar d_0 OP, whereas odd-parity (subscript u) OPs are described by a vector \mathbf{d} . The unit vectors \hat{x} , \hat{y} and \hat{z} are along the crystal directions a , b and c . The OPs, except for the E_g states, are given for 2D models. E_u and E_g irreps. support two chiral states that spontaneously break TRS.

Ginzburg-Landau free energy, [42]

$$\delta\mathcal{F} = \left(g_1\epsilon_{A_{1g,1}} + g_2\epsilon_{A_{1g,2}}\right)|\Delta|^2 + g_4\epsilon_{B_{1g}}\left(|\Delta_x|^2 - |\Delta_y|^2\right) + g_5\epsilon_{B_{2g}}\left(\Delta_x^*\Delta_y + \Delta_x\Delta_y^*\right), \quad (2.1)$$

where g_i is the coupling constant. The independent elements of strain can be classified by irreps. of D_{4h} as, $\epsilon_{A_{1g,1}} = (\epsilon_{xx} + \epsilon_{yy})$, $\epsilon_{A_{1g,2}} = \epsilon_{zz}$, $\epsilon_{B_{1g}} = (\epsilon_{xx} - \epsilon_{yy})$, $\epsilon_{B_{2g}} = 2\epsilon_{xy}$. These couplings lead to discontinuities in the associated shear elastic moduli at T_c , depending on the bilinear OP components they couple to. A one-component OP can only couple to $\epsilon_{A_{1g}}$ strains, while coupling between OPs and B_{1g} and B_{2g} strains can be allowed for two-component OPs.

Recent ultrasound data report a discontinuity at T_c in the elastic modulus c_{66} associated with shear B_{2g} (ϵ_{xy}) strain, but no discontinuity in the elastic modulus $(c_{11} - c_{12})/2$ associated with B_{1g} ($\epsilon_{x^2-y^2}$) strain.[42, 124] These observations are most straightforwardly associated with a two-component OP that produces bilinears in the B_{2g} channel and has no bilinear components in the B_{1g} channel. Table 2.2 summarizes the experimental consequences of two-component OPs in ultrasound attenuation experiments. An accidental degeneracy between $A_{1g(u)}$ and

degeneracy	product	couples to c_{66}	couple to $\frac{c_{11}-c_{12}}{2}$
$A_{1g(u)} \oplus A_{2g(u)}$	A_{2g}	No	No
$A_{1g(u)} \oplus B_{1g(u)}$	B_{1g}	No	Yes
$A_{1g(u)} \oplus B_{2g(u)}$	B_{2g}	Yes	No
$A_{2g(u)} \oplus B_{1g(u)}$	B_{2g}	Yes	No
$A_{2g(u)} \oplus B_{2g(u)}$	B_{1g}	No	Yes
$B_{1g(u)} \oplus B_{2g(u)}$	A_{2g}	No	No
$\{A_{1g(u)}, A_{2g(u)}, B_{1g(u)}, B_{2g(u)}\} \oplus E_{g(u)}$	E_g	No	No
$E_{g(u)} \oplus E_{g(u)}$	$\{A_{1g}, A_{2g}, B_{1g}, B_{2g}\}$	Yes	Yes

TABLE 2.2: Binary products of (accidentally) degenerate irreps. in the D_{4h} point group. Here we only consider degeneracy within even- or odd-parity irreps.. The last two columns indicate whether the binary product allows for coupling to the c_{66} and $(c_{11} - c_{12})/2$ modes in ultrasound attenuation experiments. The degenerate pairings that are compatible with the recent ultrasound attenuation experiments [42, 124] are highlighted in gray.

$B_{2g(u)}$ or between $A_{2g(u)}$ and $B_{1g(u)}$ (highlighted in gray) is consistent with the experimental observations.

2.4 Uniaxial strain response of T_c

Measurements of the strain response of T_c in SRO also reveal crucial information about the symmetry of the superconducting OP. Experiments with an in-plane uniaxial strain with B_{1g} symmetry, $\epsilon_{x^2-y^2}$, find that T_c is quadratic in $\epsilon_{x^2-y^2}$, $T_c \propto \epsilon_{x^2-y^2}^2$, instead of linear, $T_c \propto |\epsilon_{x^2-y^2}|$. [84, 85, 86]

The $\epsilon_{x^2-y^2}$ strain breaks $x \leftrightarrow y$ symmetry in the D_{4h} point group of the crystal, reducing it to D_{2h} . We can make the following correspondence of Irreps: $\{A_1^{D_{4h}}, B_1^{D_{4h}}\} \rightarrow A^{D_{2h}}$, $\{A_2^{D_{4h}}, B_2^{D_{4h}}\} \rightarrow B_1^{D_{2h}}$, and $E^{D_{4h}} \rightarrow \{B_2^{D_{2h}}, B_3^{D_{2h}}\}$. This mapping suggests that there is no splitting of the superconducting transition in the presence of $\epsilon_{x^2-y^2}$, i.e. no cusp of T_c , if the two OP components belong to $\{A_i^{D_{4h}}, B_i^{D_{4h}}\}$ irreps., $i = \{1, 2\}$, since they belong to the same irrep. in D_{2h} . Thus, an accidental degeneracy between $A_{1g(u)}^{D_{4h}}$ and $B_{1g(u)}^{D_{4h}}$ or between $A_{2g(u)}^{D_{4h}}$ and $B_{2g(u)}^{D_{4h}}$ can be consistent with the $\epsilon_{x^2-y^2}$ strain experiment. However, these degeneracies

are inconsistent with ultrasound measurements, as they disallow discontinuity in the shear elastic moduli c_{66} (see Table 2.2).

According to Ref.[27], the $d_{x^2-y^2} + ig_{(x^2-y^2)xy}$ pairing, which is an accidental degeneracy between $B_{1g}^{D_{4h}}$ and $A_{2g}^{D_{4h}}$ irreps., can be compatible with the uniaxial strain experiments. This is because the g -wave component vanishes at the van Hove points, such that proximity to the Lifshitz transition favors $d_{x^2-y^2}$ -wave over g -wave. The $\epsilon_{x^2-y^2}$ strain moves the γ -band FS of SRO closer to the van Hove points [125] and lifts the accidental degeneracy between the $d_{x^2-y^2}$ and g -wave components, resulting in a single $d_{x^2-y^2}$ -wave pairing state. As a result, the dependence of T_c is a smooth and non-singular function of $\epsilon_{x^2-y^2}$. Similarly, $A_{1g(u)}^{D_{4h}} \pm iB_{2g(u)}^{D_{4h}}$ and $A_{2u}^{D_{4h}} \pm iB_{1u}^{D_{4h}}$ pairings can also explain uniaxial strain experiments, as they are composed of two OP components, one of which vanishes at the van Hove points, while the other does not.

2.5 Nodal structures

Low-lying excitations in the superconducting state of SRO have been confirmed by multiple experimental probes. Specific heat measurements find that C_e/T is perfectly linear in T , i.e. $C_e/T \propto T$, at low temperatures, where C_e is the electronic specific heat. [126, 127, 111, 128, 129] This observation corresponds to quasiparticles excited from line nodes in \mathbf{k} -space and is consistent with the thermal conductivity measurements in Refs. [130, 112]. Recent scanning tunneling microscope (STM) studies[113] further support this conclusion. It is possible that these observations can be explained by lines of deep gap minima. [108] The experiment estimates of the gap minima are less than 3% of the total gap. [131, 112, 132]

The precise location (in \mathbf{k} -space) of the lines of nodes or minima remains unclear. Deguchi *et al.* [111] proposed vertical line nodes in the (1,0,0) direction based on field-dependent specific heat measurements, while similar measurements by Kittaka *et al.* [129] suggest horizontal line nodes. On the other hand, the thermal conductivity experiments and the STM data support vertical nodes in the (1,1,0) direction.[112, 113]

2.6 Summary

Here we summarize the constraints on the OP from the experiments discussed above.

- The superconducting OP has two components forming a complex OP that spontaneously breaks TRS.
- The revised Knight shift measurements are strongly suggestive of a spin-singlet order parameter.
- Ultrasound and (1,0,0) uniaxial strain measurements can be explained by accidental degeneracy between $A_{1g(u)}$ and $B_{2g(u)}$ or between $B_{1g(u)}$ and $A_{2g(u)}$ irreps..
- The superconducting OP has lines of nodes or extremely deep gap minima, which is less than 3% of the total gap.

Chapter 3

Spontaneous edge current in higher chirality superconductors

3.1 Preface

Spontaneous edge currents in chiral p -wave superconductors have been studied extensively. These studies were motivated by attempts to reconcile the early theoretical prediction of a significant edge current [75] with the null result observed in experiments on SRO[37, 38, 39], which was thought to support chiral p -wave superconductivity. In contrast, similar studies on chiral d - and f -wave superconductors are relatively rare. Previous studies[68, 70, 71] have shown that edge currents in higher chirality superconductors vanish in the semiclassical continuum limit, in stark contrast to the chiral p -wave case. Here, we expand on previous studies on the edge current in chiral d - and f -wave superconductors by including the effects of finite temperature, Meissner screening, and surface disorder. In general, these effects can all reduce the edge current in the chiral p -wave case. [60, 74, 75, 78, 79]

For simplicity, we assume the superconductor is two-dimensional with a single cylindrical Fermi surface. We use a quasi-classical Green function formalism, which allows us to determine the superconducting OP and edge current self-consistently and which has been widely used to study inhomogeneity in superconductors. [133, 134, 135, 136, 75] (See Appendix A for details.) Semiclassical analysis, Ginzburg-Landau analysis, and lattice BdG calculations are also employed in our study.

We find that, in general, the edge currents in chiral d - and f -wave superconductors are quite small, compare to the analogous chiral p -wave case. As a result, the Meissner screening effects are much weaker in higher chirality superconductors. In the absence of Meissner screening, the integrated current is non-zero at finite temperature, T , and maximized near $T_c/2$, where T_c is the transition temperature, although it vanishes at $T = 0$. Our work provides an explanation for this unusual temperature dependence. Surface roughness suppresses the edge current in the chiral f -wave superconductor, while it can invert the direction of the current flow in the chiral d -wave case. However, we find that this current inversion is not universal beyond the continuum limit and can depend on microscopic details, such as the surface orientation and the chemical potential of the sample.

Experimentally, direct searches for edge currents have been intensively conducted on SRO, while other chiral superconducting candidate materials are less studied. [25] Scanning SQUID measurements of $\text{PrOs}_4\text{Sb}_{12}$, a 3D chiral d -wave pairing candidate, also return null results. [38] As more and more candidates for higher chirality superconductivity become available, such as SrAsPt [63], doped Graphene [64] and UPt_3 [25], similar searches for edge currents may be undertaken. Our results, especially the finite temperature behavior of the integrated current and the non-universal aspect of the current inversion in the presence of disorder in the chiral d -wave pairing case, could be important for understanding these materials.

3.2 Publication

Spontaneous edge current in higher chirality superconductorsXin Wang,¹ Zhiqiang Wang,¹ and Catherine Kallin^{1,2}¹*Department of Physics and Astronomy, McMaster University, Hamilton, Ontario L8S 4M1, Canada*²*Canadian Institute for Advanced Research, Toronto, Ontario M5G 1Z8, Canada*

(Received 26 May 2018; published 4 September 2018)

The effects of finite temperature, Meissner screening, and surface roughness on the spontaneous edge current for higher chirality quasi-two-dimensional superconductors are studied in the continuum limit using the quasiclassical Eilenberger equations. We find that the total spontaneous current is nonzero at finite temperature T and maximized near $T = T_c/2$, where T_c is the transition temperature, although it vanishes at $T = 0$. In the presence of surface roughness, we observe a surface current inversion in the chiral d -wave case that can be understood in terms of a disorder-induced s -wave pairing component in the rough surface regime. This conclusion is supported by a Ginzburg-Landau analysis. However, this current inversion is nonuniversal beyond the continuum limit, as demonstrated by self-consistent lattice Bogoliubov-de Gennes calculations.

DOI: [10.1103/PhysRevB.98.094501](https://doi.org/10.1103/PhysRevB.98.094501)**I. INTRODUCTION**

Chiral superconductors spontaneously break time-reversal symmetry and support chiral Majorana edge modes [1–3]. As a consequence, there are spontaneous supercurrents generated at edges. Although the number of chiral edge modes is protected by topology [4], the edge currents are not topologically protected and can strongly depend on microscopic details [5–8], since charge is not conserved in a superconducting state, in contrast to a quantum Hall state.

Edge currents, as well as the related total orbital angular momentum of Cooper pairs, have been studied extensively for chiral p -wave superconductors [5–9]. The major motivation is to reconcile the theoretical prediction of a large edge current [10] with the null result observed in scanning probe measurement on Sr_2RuO_4 [11–13], which is believed to be a chiral p -wave superconductor [2,3,14]. Theoretical studies have shown that, in the absence of Meissner screening, the integrated current is substantial at $T = 0$ [6,15–18] and decreases rapidly as T increases [16,18]. Previous studies [5,7,8] have shown that spontaneous supercurrents in higher chirality superconductors are different from the chiral p -wave case. In particular, the integrated edge currents of the higher chirality superconductors vanish in the semiclassical continuum limit, in stark contrast to the chiral p -wave case [5]. These studies focused on $T = 0$ and neglected Meissner screening. More recently, Ref. [19] studied finite temperature and screening effects on edge currents for higher chirality superconductors in a mesoscopic system (a very narrow cylinder).

In this paper, we generalize the study in Ref. [19] to a half-infinite system, where these effects can be separated from finite size effects and also examine more closely the explanation for and robustness of current inversion due to disorder. Following Refs. [10,19], we study the edge currents in the continuum limit for a quasi-two-dimensional chiral superconductor using the quasiclassical Eilenberger equations [20]. Interestingly, we find that, without Meissner screening, the integrated edge currents for higher chirality superconductors are nonzero at finite T , unlike at $T = 0$, although they are much

smaller than the current of the chiral p -wave case. This finite temperature current is a consequence of the superconducting order-parameter variations near a surface.

In Refs. [21–24], it has been shown that surface roughness, together with band structure effects, can lead to substantial suppression of the edge current in a chiral p -wave superconductor and potentially account for the null result of edge currents in Sr_2RuO_4 experiments. Here we study rough surface effects on higher chirality superconductors by introducing an impurity self-energy in the quasiclassical Green's function. As in Ref. [19], we find the edge current direction is reversed due to strong surface roughness for chiral d -wave pairing in the continuum limit. However, our calculations together with a Ginzburg-Landau (GL) analysis, suggest a physically more transparent explanation for the current inversion. We ascribe the inversion to a strong disorder induced subdominant s -wave component near the interface between the rough surface regime and the bulk. Near the interface, the original $d_{x^2-y^2}$ and id_{xy} components have almost identical spatial variation, due to the surface and disorder, and their contribution to the current is almost zero. On the other hand, the induced s -wave component is real and can combine with the id_{xy} component to give a sizable current near the interface if the s -wave channel is not too repulsive. The current resulting from the $s + id_{xy}$ pairing is opposite in direction to that near the specular surface.

However, the current inversion is nonuniversal beyond the continuum limit. This is supported by self-consistent lattice Bogoliubov-de Gennes (BdG) calculations, where we explicitly show that the existence of the current inversion depends on edge orientation and chemical potential or band structure effects.

The rest of the paper is organized as follows: In Sec. II we outline the self-consistent Eilenberger formalism. Then we present our results of the edge currents for a specular surface without and with Meissner screening in Secs. III and IV, respectively. Section V contains the results with surface roughness. Section VI contains the discussion and conclusions.

II. FORMALISM

We consider a semi-infinite ($x > 0$) quasi-2d superconductor with a cylindrical Fermi surface independent of k_z . The system is described by the following Eilenberger equation [20]:

$$-iv_{F_x} \frac{d}{dx} \hat{g}(\theta_{\mathbf{k}}, x; \omega_n) = [\hat{H}(\theta_{\mathbf{k}}, x; \omega_n), \hat{g}(\theta_{\mathbf{k}}, x; \omega_n)], \quad (1)$$

valid if the characteristic length scale considered is much longer than the Fermi wavelength. Here, $\hat{g}(\theta_{\mathbf{k}}, x; \omega_n)$ is the quasiclassical Green's function, $\theta_{\mathbf{k}}$ is defined by the direction of the quasiparticle momentum, $\mathbf{k} = k_F(\cos \theta_{\mathbf{k}}, \sin \theta_{\mathbf{k}})$, and $\omega_n = (2n + 1)\pi T$ is the Matsubara frequency. The Green's function does not depend on the magnitude of the momentum \mathbf{k} as all high-energy information involving $|\mathbf{k}| \neq k_F$ has been integrated out. Furthermore, since there is no variation along z , this coordinate is not shown in \hat{g} . As usual, in the Nambu particle-hole space, $\hat{g}(\theta_{\mathbf{k}}, x; \omega_n)$ is a 2×2 matrix

$$\hat{g}(\theta_{\mathbf{k}}, x; \omega_n) = \begin{pmatrix} g(\theta_{\mathbf{k}}, x; \omega_n) & if(\theta_{\mathbf{k}}, x; \omega_n) \\ -i\bar{f}(\theta_{\mathbf{k}}, x; \omega_n) & -g(\theta_{\mathbf{k}}, x; \omega_n) \end{pmatrix}, \quad (2)$$

where g and f are the normal and anomalous parts, respectively. The two components satisfy the normalization relation $g^2(\theta_{\mathbf{k}}, x; \omega_n) + f(\theta_{\mathbf{k}}, x; \omega_n)\bar{f}(\theta_{\mathbf{k}}, x; \omega_n) = 1$, which is a consequence of $\hat{g}^2(\theta_{\mathbf{k}}, x; \omega_n)$ being a position independent constant along the quasiparticle trajectory within the Eilenberger quasiclassical formalism. On the right hand side of Eq. (1), $\hat{H}(\theta_{\mathbf{k}}, x; \omega_n)$ is given by

$$\hat{H}(\theta_{\mathbf{k}}, x; \omega_n) = \begin{pmatrix} i\omega_n - ev_{F_y} A_y(x) & -\Delta(\theta_{\mathbf{k}}, x) \\ \Delta^*(\theta_{\mathbf{k}}, x) & -i\omega_n + ev_{F_y} A_y(x) \end{pmatrix}, \quad (3)$$

where, $A_y(x)$ is the y component of the vector potential satisfying $\nabla \times \mathbf{A} = B_z(x)\hat{z}$. $B_z(x)$ is the local magnetic field, which can either be generated by the spontaneous edge current or applied externally. Here, we only consider the spontaneous field and a gauge is chosen such that $A_x(x) \equiv 0$. The Fermi velocities in Eqs. (1) and (3) are defined as $\mathbf{v}_F = (v_{F_x}, v_{F_y}) = v_F(\cos \theta_{\mathbf{k}}, \sin \theta_{\mathbf{k}})$.

The off-diagonal component $\Delta(\theta_{\mathbf{k}}, x)$ in Eq. (3) is the chiral superconducting order parameter. For chiral m -wave pairing, it is given by $\Delta(\theta_{\mathbf{k}}, x) = \Delta_1(x)\cos(m\theta_{\mathbf{k}}) + \Delta_2(x)\sin(m\theta_{\mathbf{k}})$. We choose $\Delta_1(x)$ to be real and $\Delta_2(x)$ to be purely imaginary in the bulk such that the order parameter is chiral. Δ_1 and Δ_2 are determined self-consistently from the following gap equations:

$$\Delta_1(x) = \pi T N_F V \sum_{|\omega_n| < \omega_c} \langle 2 \cos(m\theta_{\mathbf{k}}) f(\theta_{\mathbf{k}}, x; \omega_n) \rangle, \quad (4a)$$

$$\Delta_2(x) = \pi T N_F V \sum_{|\omega_n| < \omega_c} \langle 2 \sin(m\theta_{\mathbf{k}}) f(\theta_{\mathbf{k}}, x; \omega_n) \rangle. \quad (4b)$$

$\langle \dots \rangle = \frac{1}{2\pi} \int_{-\pi}^{\pi} d\theta_{\mathbf{k}} \langle \dots \rangle$; ω_c is the pairing energy cutoff; N_F is the normal state density of states at the Fermi energy; and V is the pairing interaction strength. The dimensionless attractive interaction strength $N_F V$ is connected to the superconducting transition temperature T_c by

$$\frac{1}{N_F V} = \log \frac{T}{T_c} + \sum_{n, |\omega_n| \leq \omega_c} \frac{1}{n - 1/2}, \quad (5)$$

which becomes T independent in the weak coupling limit $T \ll T_c \ll \omega_c$. We will use this equation for $N_F V$ in terms of T_c and ω_c and rescale all energy quantities by T_c . In this way, we do not need to explicitly specify the value of $N_F V$.

We use the Riccati parametrization [25] to solve for the Green's function matrix, \hat{g} . The current density $J_y(x)$ is

$$J_y(x) = -ev_F N_F T \sum_{|\omega_n| < \omega_c} (-i\pi) \langle \sin(\theta_{\mathbf{k}}) g(\theta_{\mathbf{k}}, x; \omega_n) \rangle. \quad (6)$$

The spontaneous current, $J_y(x)$, gives rise to a local field, $B_z(x)$, which can be calculated from the Maxwell equation:

$$\frac{dB_z(x)}{dx} = -\mu J_y(x), \quad (7)$$

where the permeability, μ , is related to the penetration depth $\lambda_L = \sqrt{m/e^2 \mu n}$, n is the normal state electron density and m ($-e$) is the electron mass (charge). To include Meissner screening in a self-consistent manner, we solve the Eilenberger equation together with the above Maxwell equation simultaneously.

Lastly, we consider the effect of surface roughness modeled by adding a disorder-induced self-energy, $\hat{\Sigma}$, to \hat{H} in Eq. (1). Then $\hat{\Sigma}$ can be calculated within the self-consistent Born approximation from the Green's function,

$$\hat{\Sigma}(x; \omega_n) = \frac{i}{2\tau(x)} \langle \hat{g}(\theta_{\mathbf{k}}, x; \omega_n) \rangle. \quad (8)$$

Here $\tau(x)$ is the local x -dependent mean free time. As a model of roughness near the surface, we take $1/\tau(x)$ to be maximum at $x = 0$ and to decay to zero into the bulk. Note that $\hat{\Sigma}(x; \omega_n)$ does not depend on the angle $\theta_{\mathbf{k}}$, which is a consequence of the assumption that locally the disorder scattering is isotropic.

We solve the above coupled equations for the Riccati parameters, Δ_1 , Δ_2 , A_y , and $\hat{\Sigma}$ simultaneously by iteration until a stable self-consistent solution for all parameters is achieved.

III. EDGE CURRENTS WITHOUT MEISSNER SCREENING AND SURFACE ROUGHNESS

We first consider the edge currents without Meissner screening and surface roughness and focus primarily on the finite temperature results.

The spatial profiles of the $T = 0$ edge currents are similar to those obtained in Ref. [19], although not identical because of the finite system size in Ref. [19], and can be found in Appendix A. From Figs. 7(e) and 7(f), we see that the edge current $J_y(x)$ is finite for the chiral d - and f -wave pairings, although the integrated current is zero. At first glance, this seems to contradict the weak coupling GL result [5]:

$$J_y(x) \propto k_3 (\Delta_2 \partial_x \Delta_1^* - c.c.) - k_4 (\Delta_1^* \partial_x \Delta_2 - c.c.), \quad (9)$$

where $k_3 = k_4 = 0$ for all non- p -wave chiral pairing. However, there is no contradiction since Eq. (9) only accounts for the lowest order contribution in the GL expansion. Higher order terms, such as $\Delta_1^* \partial_x^3 \Delta_2 - c.c.$, can lead to a small current

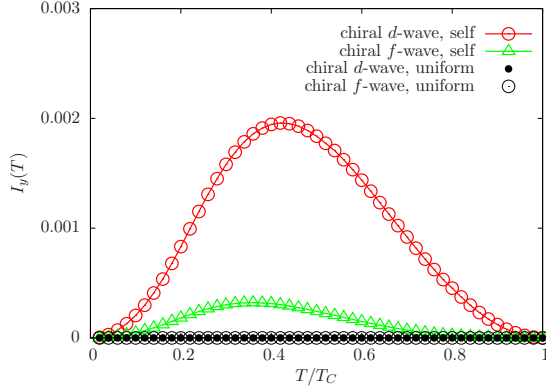


FIG. 1. Temperature dependence of the integrated edge current, $I_y(T)$, for chiral d - (red open circles) and f - (green triangles) waves with the self-consistently determined superconducting order parameter. The black dots (open circles) are numerical results for chiral d (f)-wave with a uniform order parameter $\Delta_1(x) = \Delta_2(x) \equiv \Delta(\text{bulk})$. I_y is scaled by $J_0 \xi_0$, where $J_0 = e v_F N_F T_c$ and $\xi_0 = v_F / \pi \Delta(\text{bulk})$ is the zero temperature coherence length.

density. Note that Eq. (9) implies a current along y when the order parameter, $\Delta(\theta_{\mathbf{k}}, x)$, has a spatial phase variation along x . This transverse response results from the two-component chiral nature of the order parameter, as discussed in detail in Refs. [6,26].

At finite T , the total integrated current (or more precisely, the current per-unit length along the z direction for the quasi-2d system), $I_y \equiv \int_0^\infty J_y(x) dx$, for a chiral p -wave superconductor decreases monotonically with T and vanishes at the superconducting transition temperature T_c [16,18]. The temperature dependence for chiral d - and f -wave superconductors is quite different, as shown in Fig. 1. Although $I_y(T) = 0$ at both $T = 0$ and $T = T_c$, it is nonzero at $0 < T < T_c$ and reaches its maximum just below $T = T_c/2$. By contrast, as found in Ref. [5], for a uniform superconducting order parameter, i.e., $\Delta_1(x) = \Delta_2(x) \equiv \Delta(\text{bulk})$, $I_y(T) \equiv 0$ for any T . This result can be derived from an analytical treatment of the Eilenberger equation (see Appendix B) and a semiclassical BdG analysis. The spatially varying order parameter is crucial for the nonzero I_y at finite T .

To understand the above results, we first consider the case of a uniform superconducting order parameter. In this case, the edge state dispersion can be obtained from a semiclassical BdG analysis, as given in Refs. [5,27]. It is determined by the enhanced component of the order parameter and for our geometry given by the following piecewise function [5]:

$$E^{(j)}(\theta_{\mathbf{k}}) = \begin{cases} (-1)^{(j-1)} \Delta_0 \cos(m\theta_{\mathbf{k}}), & \text{if } m = \text{even}, \\ (-1)^j \Delta_0 \sin(m\theta_{\mathbf{k}}), & \text{if } m = \text{odd}, \end{cases} \quad (10)$$

for $-\pi/2 + (j-1)\pi/m \leq \theta_{\mathbf{k}} < -\pi/2 + j\pi/m$, where the edge state branch number $j = 1, 2, \dots, m$. For the chiral d -wave case there are two edge state branches (see Fig. 2) and their dispersions, in terms of $k_y = k_F \sin \theta_{\mathbf{k}}$, are $E^{(j)}(k_y) = \pm \Delta_0 (k_F^2 - 2k_y^2)/k_F^2$. At $T = 0$, only the states with $E^{(j)}(\theta_{\mathbf{k}})$

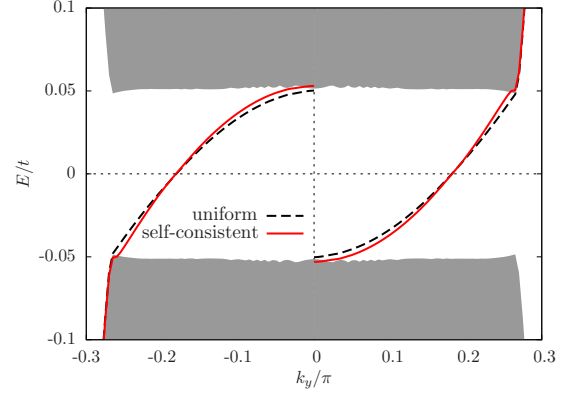


FIG. 2. Edge state energy dispersion for chiral d -wave pairing obtained from BdG calculations with a self-consistently determined superconducting order parameter (solid red lines) and a uniform order parameter (dashed black lines). The shaded regimes represent dense bulk energy spectra, whose details are not shown here. Inside the bulk superconducting gap, there are two edge state energy dispersions crossing $E = 0$ at $k_y = \pm k_F / \sqrt{2}$.

≤ 0 are occupied and their contribution to the edge current is [5]

$$I_y(T=0) \propto \sum_{j=1}^m \int \Theta(-E^{(j)}(\theta_{\mathbf{k}})) k_y dk_y \quad (11a)$$

$$\propto \int \Theta(-E^{(1)}(\theta_{\mathbf{k}})) \left\{ \sum_{j=1}^m \sin \left(2\theta_{\mathbf{k}} + (j-1) \frac{2\pi}{m} \right) \right\} d\theta_{\mathbf{k}} \quad (11b)$$

$$= 0, \quad (11c)$$

where $\Theta(x)$ is the Heaviside step function and from the first line to the second we have used the periodicity of $E^{(j)}(\theta_{\mathbf{k}})$, $E^{(j)}(\theta_{\mathbf{k}}) = E^{(j+1)}(\theta_{\mathbf{k}} + \pi/m)$.

The last equality comes from the fact that the $\{\dots\}$ factor in Eq. (11b) vanishes identically for any $|m| \neq 1$. Hence the zero $I_y(T=0)$ is a consequence of the exact cancellation between the m branch contributions. Notice that the cancellation is between m different k_y states, one from each of the m edge state branches for any allowed energy E , and it is independent of the zero-temperature occupation number $\Theta(x)$. At finite T , $I_y(T)$ is still given by the above integral in Eqs. (11a) and (11b) except that $\Theta(x)$ is replaced by the Fermi-Dirac distribution, $n_F(x) = 1/(e^{x/T} + 1)$, and the gap magnitude is T dependent. Since the factor $\{\dots\} \equiv 0$ in Eq. (11b) is independent of T , we reach the conclusion that $I_y(T) \equiv 0$ for any $|m| \neq 1$, if the order parameter is uniform, in agreement with the results in Fig. 1. We should emphasize that the edge currents not only come from edge states but also from bulk scattering states. In the following, for qualitative understanding, we only focus on the edge state contributions. However, in Appendix B, we show that if the order parameter is uniform, the bulk contribution of $I_y(T)$ also vanishes at all T .

Next we consider the case with Δ_1 and Δ_2 determined self-consistently. When the x -dependence of the superconducting order parameter near the surface is taken into account, $E^{(j)}(\theta_{\mathbf{k}})$ is no longer given by Eq. (10) and $I_y(T=0)$ cannot be expressed as Eq. (11b). However, the m integrals in Eq. (11a) still cancel at $T=0$ because they only depend on the lower and upper k_y limits of each integral but not the details of $E^{(j)}(\theta_{\mathbf{k}})$. These k_y values remain the same as in the uniform order parameter case and only depend on k_F or m , because the lower k_y limit is determined by the starting $\theta_{\mathbf{k}}$ point of each branch dispersion, $E^{(j)}(\theta_{\mathbf{k}})$, while the upper limit by $E^{(j)}(\theta_{\mathbf{k}}) = 0$.¹ This is also confirmed for the chiral d -wave case by self-consistent BdG, as shown in Fig. 2. As a consequence, from Eq. (11a), $I_y(T=0) = 0$ remains. This result is consistent with Refs. [5,7], where $I_y(T=0)$ was shown to be of order $\mathcal{O}(\Delta/E_F)$ for chiral d - or f -waves; in the semiclassical approximation, $\Delta/E_F \rightarrow 0$ (implicit in the Eilenberger formalism), and, consequently, $I_y(T=0) = 0$.

At finite T , edge states with $E^{(j)}(\theta_{\mathbf{k}}) > 0$ also contribute to the current due to thermal population and the entire $E^{(j)}(\theta_{\mathbf{k}})$ dispersion matters. Since $E^{(j)}(\theta_{\mathbf{k}})$ is no longer given by Eq. (10) and $I_y(T)$ cannot be written in the form of Eq. (11b), the exact cancellation between the m branches breaks down and gives rise to the nonzero I_y at finite T in Fig. 1. As $T \rightarrow T_c$, one approaches equal occupation of all edge states, which results in zero current. The competition between the two factors, the imbalance between the m different edge state branches and the thermal degradation of currents as one approaches T_c , results in the $I_y(T)$ peak around $T = T_c/2$ in Fig. 1. These results could have implications for future experiments on possible higher chirality superconductors, as discussed in the conclusions.

We also note that in Fig. 1, as $T \rightarrow T_c$, $I_y(T)$ vanishes faster than $I_y(T) \propto T_c - T$, in stark contrast to the chiral p -wave case [16,18]. The difference comes from the fact that the lowest order nonzero contribution to the edge current density for higher chirality superconductors comes from terms, which involve higher order spatial derivatives than those in Eq. (9) for chiral p -wave. For example, for chiral d -wave, two of these terms are $\Delta_1^2 \partial_x^3 \Delta_2 - c.c.$, which predict a scaling of the current density $J_y \propto \Delta(T)^2 / \xi(T)^3$ for $T \lesssim T_c$. Here $\Delta(T)$ and $\xi(T)$ is the temperature-dependent gap magnitude and coherence length, respectively. This leads to $I_y(T) \propto J_y \xi(T) \propto (T - T_c)^2$ for T near T_c .²

Although we have focused on higher chirality superconductors in the above, the same conclusion that the self-consistency of the order parameter does not change the

¹At these k_y (or $\theta_{\mathbf{k}}$) points, edge states for positive chirality are degenerate in energy with those of negative chirality, which occurs when one component of the order parameter, $\Delta(\theta_{\mathbf{k}}, x) = \Delta_1(x) \cos(m\theta_{\mathbf{k}}) + \Delta_2(x) \sin(m\theta_{\mathbf{k}})$, vanishes for a general x . Therefore, the degenerate k_y (or $\theta_{\mathbf{k}}$) points are completely fixed by the pairing symmetry of the two components, either $\cos(m\theta_{\mathbf{k}}) = 0$ or $\sin(m\theta_{\mathbf{k}}) = 0$, regardless of whether Δ_1 and Δ_2 are uniform or self-consistently determined.

²In Fig. 1, the T dependence of $I_y(T)$ for chiral d -wave may slightly deviate from the quadratic prediction at $T \approx T_c$ due to the finite $\theta_{\mathbf{k}}$ - and x -grid sizes used in numerics and the diverging $\xi(T)$ as $T \rightarrow T_c$.

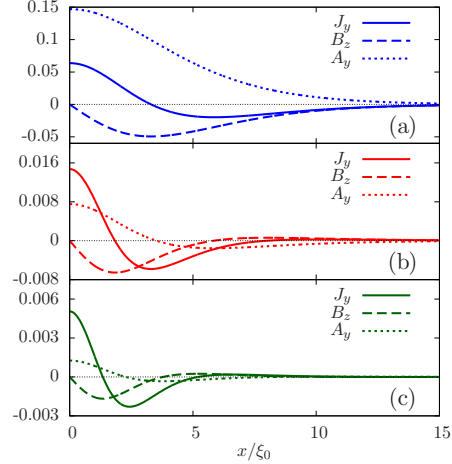


FIG. 3. (a)–(c) Spatial dependencies of the edge current density, $J_y(x)$, induced magnetic field, $B_z(x)$, and vector potential, $A_y(x)$, with Meissner screening taken into account for chiral p -, d - and f -wave pairings, respectively. GL ratio $\kappa \equiv \lambda_L/\xi_0 = 2.5$. $J_y(x)$, $A_y(x)$ and $B_z(x)$ are scaled by $J_0 = ev_F N_F T_c$, $\Delta(\text{bulk})/ev_F$ and $B_c = \Phi_0/2\sqrt{2}\pi\xi_0\lambda_L$, respectively, where $\Phi_0 = h/2e$ and $T = 0.02T_c$.

$I_y(T=0)$ but has an effect on the finite temperature $I_y(T)$ applies to the chiral p -wave case as well. Since, for the chiral p -wave case, $I_y(T)$ is already large for a uniform order parameter, the self-consistency of the order parameter only changes the finite temperature result by a relatively small amount.

Finally, in a more general lattice model with anisotropy, $I_y(T=0)$ does not need to vanish for higher chiralities. The above argument breaks down, since the k_y positions of $E^{(j)}(k_y) = 0$ are not protected by any bulk band topology.

IV. MEISSNER SCREENING EFFECT ON THE EDGE CURRENTS

Meissner screening is included by solving the Eilenberger equations and the Maxwell equation simultaneously and self-consistently. The results are shown in Fig. 3. As expected, the induced magnetic field $B_z(x)$ vanishes into the bulk in all cases. Comparing Figs. 3(a)–3(c) with Figs. 7(d)–7(f) (in Appendix A) we see that, although screening reduces the edge current magnitude by a significant fraction in the chiral p -wave case, the magnitude of the edge currents in the higher chirality cases is much less affected. This is expected since the unscreened edge currents for higher chirality have contributions from different edge state branches with different signs as well as spatial variations at different length scales (see Appendix A, Fig. 8). The resulting oscillating (with sign changes) unscreened current is, effectively, partially self-screened. Screening also introduces one additional node in the spatial dependence of $J_y(x)$ for all chiral pairing channels due to the different length scales of the diamagnetic current (λ) and the spontaneous current (ξ_0).

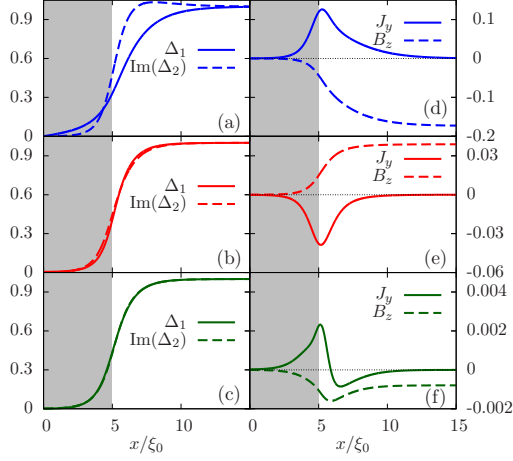


FIG. 4. (a)–(c) Spatial dependence of Δ_1 and $\text{Im}(\Delta_2)$ in the presence of surface roughness for chiral p -, d - and f -waves, respectively. (d)–(f) Spatial dependence of the edge current $J_y(x)$ and the induced $B_z(x)$ in the presence of surface roughness for different chiral pairing channels. The effective rough regime with width $W = 5\xi_0$ is shaded in grey. The strength of the roughness is characterized by the shortest mean free path, $\ell_p \equiv v_F \tau(x=0)$, in the rough regime, which is $\xi_0/\ell_p = 1.0$ for the results shown. The two order parameter components have been already scaled by their bulk values. Meissner screening is not taken into account. $T = 0.02T_c$.

V. ROUGH SURFACE EFFECT

We now discuss the effect of the surface roughness on the edge currents. The surface roughness is modeled with a spatially dependent local scattering rate given by

$$\frac{1}{\tau(x)} = \frac{1}{\tau(0)} \left(\frac{1 - \tanh[(x-W)/\xi_0]}{2} \right), \quad (12)$$

which is maximal at $x=0$ and decays into the bulk. W is the effective width of the rough regime.

To simplify the discussion, we first ignore Meissner screening. The order parameter and edge current density computed are shown in Fig. 4 for different pairing channels and strong surface roughness with a local mean free path $\ell_p \equiv v_F \tau(x=0) = \xi_0$. The superconductivity is completely suppressed at the vacuum-superconductor interface and is nonzero in the rough regime only near $x=W$, where the surface roughness gradually disappears.

Aside from a suppression of the edge current, the most prominent feature in Fig. 4(e) is that the edge current for the chiral d -wave pairing case flows in a direction opposite to that of the specular surface [see Fig. 7(e)], while the edge current direction of odd-angular momentum channels remains unaltered in the presence of the surface roughness. The edge current inversion for the chiral d -wave pairing has been observed and discussed in Refs. [19,28] previously. The explanation there is that the outer edge current of the clean system, the positive part of $J_y(x)$ in Fig. 7(e), is suppressed by surface roughness because it is closer to $x=0$, while the inner current, the negative part of $J_y(x)$ in Fig. 7(e), survives. The net

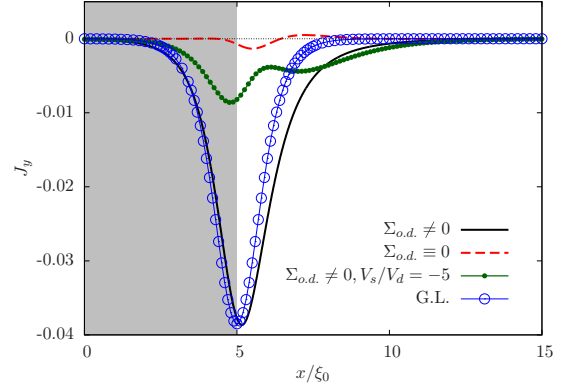


FIG. 5. Comparison of $J_y(x)$ obtained with (solid black line) and without (dashed red line) the off-diagonal impurity self energy, $\Sigma_{o,d}$, discussed in the text. The current from the GL free-energy analysis in Eq. (18) (blue open circles) is plotted. Green line with dots shows that the inverted current is greatly reduced when an s -wave repulsive interaction $V_s = -5V_d$ is present. Here V_d is the bulk d -wave attractive interaction.

result is then a current direction inversion. In the following, we provide an alternative explanation for the current inversion near $x=W$ for the chiral d -wave pairing and analyze the robustness of this effect.

We ascribe the currents near $x=W$ in Fig. 4(e) to a disorder-induced s -wave pairing self-energy. Namely, $\hat{\Sigma}(x; \omega_n)$ defined in Eq. (8) has a nonzero component off-diagonal in particle-hole space. Let us denote it as $\Sigma_{o,d}(x; \omega_n)$. $\Sigma_{o,d}$ has s -wave symmetry and is independent of θ_k . Numerically if we set $\Sigma_{o,d}(x; \omega_n) \equiv 0$ by hand, i.e., drop the off-diagonal term in calculating $\hat{\Sigma}$ from Eq. (8), then the current near $x=W$ is almost completely suppressed, as shown in Fig. 5.

Effectively, we can interpret $\Sigma_{o,d}$ as an additional s -wave “order parameter”, Δ_s , induced by the disorder. This is possible because, although $\Sigma_{o,d}$ depends on the Matsubara frequency, ω_n , it is even in ω_n in the even parity $d+id$ pairing case; on the contrary, if the bulk pairing has an odd parity, then $\Sigma_{o,d}$ is an odd function of ω_n . The s -wave pairing self-energy term is allowed to mix with the original order parameter, which is non- s -wave, because the edge breaks inversion symmetry.

From Eq. (8), we see that the s -wave $\Sigma_{o,d}$ comes from the anomalous Green’s function $f(\theta_k, x; \omega_n)$ having a nonzero s -wave component. This s -wave component is subdominant to the bulk $d+id$ pairing and induced by the suppression of the $d+id$ pairing near $x=W$, which is in turn due to the edge and the disorder. In weak-coupling GL theory, this can be seen from the following mixed gradient term [29,30] in free energy:

$$+4A_4(D_x \Delta_s^* D_x \Delta_1 + c.c.), \quad (13)$$

derived in Appendix D. Here $A_4 > 0$, $D_x \equiv \frac{v_F}{2} \partial_x$ and Δ_s is the subdominant s -wave order parameter induced near $x=W$. This term favors a nonzero Δ_s where Δ_1 has a spatial variation, which is most significant near $x=W$. The sign of Δ_s can be determined by minimizing Eq. (13). Given that Δ_1 is real and

$\partial_x \Delta_1 > 0$ near $x = W$ (see Fig. 4), Δ_s is real as well and also $\partial_x \Delta_s < 0$, which leads to $\Delta_s > 0$ since $\Delta_s = 0$ in the bulk. In other words, the sign of Δ_s is the same as that of Δ_1 .

Using Δ_s , we can now understand the spontaneous current $J_y(x)$ near $x = W$ in Fig. 5. Since the spatial variations of Δ_1 and Δ_2 are almost identical near $x = W$, the spontaneous current due to the original $d + id$ components is greatly suppressed. As a consequence, the current mainly comes from the $s + id_{xy}$ pairing components. This current can be derived from another mixed gradient term [29,30] in the GL free energy:

$$\mathcal{F}_{\text{mix}} \equiv +A_4 v_F^2 \{ \partial_x \Delta_2 \partial_y \Delta_s^* + \partial_y \Delta_2 \partial_x \Delta_s^* + c.c. \}. \quad (14)$$

For the half-infinite geometry, the spontaneous current is along y direction. J_y can be obtained by minimal coupling \mathcal{F}_{mix} to the vector potential A_y and taking a functional derivative of \mathcal{F}_{mix} with respect to A_y . The result is

$$J_y \propto -2e i \{ \Delta_2 \partial_x \Delta_s^* - \Delta_s^* \partial_x \Delta_2 - c.c. \}, \quad (15)$$

with a positive proportionality constant. $e > 0$ is the magnitude of an electron charge. To a good approximation, the spatial variation of Δ_s follows that of the local scattering rate since $\Delta_s \sim \Sigma_{o.d.} \propto 1/\tau(x)$. So we can take

$$\Delta_s(x) = \Delta_s \operatorname{sgn}(\Delta_1) \frac{\tau(0)}{\tau(x)}, \quad (16)$$

where $\Delta_s > 0$ is the overall magnitude and we have made the sign dependence of Δ_s on $\operatorname{sgn}(\Delta_1)$ explicit. Here Δ_1 is the bulk value of the $d_{x^2-y^2}$ component order parameter. The spatial variation of the id_{xy} in Fig. 4(b) can be approximated by

$$\Delta_2(x) = i \operatorname{Im}(\Delta_2) \frac{\tanh[(x - W)/\ell_h] + 1}{2}, \quad (17)$$

where ℓ_h is the healing length of the id_{xy} component near $x = W$ and it can be roughly taken as the maximal local mean free path: $\ell_h \approx \ell_p = \xi_0$. Then from the expression of J_y in Eq. (15) we have

$$J_y(x) = -J_0 \operatorname{sgn}(\Delta_1 \operatorname{Im}(\Delta_2)) \operatorname{sech}^2 \frac{x - W}{\xi_0}, \quad (18)$$

where $J_0 > 0$ is a constant that sets the maximal $|J_y(x)|$ magnitude. Using $J_0 \approx 0.04$, this gives a current profile in Fig. 5 (open circles) very similar to that from the numerical Eilenberger solution (black solid line). Note that $J_y(x)$ is still odd in the chirality of the $d + id$ order parameter, as expected. The dependence on $\operatorname{sgn}(\Delta_1)$ is inherited from the disorder-induced $\Delta_s(x)$.

The GL explanation presented here, as well as the lattice BdG results, depends only on frequency-independent order parameters and their spatial derivatives, but in the Eilenberger calculation the spontaneous current can also be related to odd-frequency pairing components of the anomalous Green's functions [19]. The odd-frequency pairing appears as derivatives of an order parameter in the GL analysis after the frequency is integrated over. So the two, GL and Eilenberger odd frequency pairing, are connected, but the GL analysis is physically more transparent. For instance, the GL formulation shows that the current inversion depends not only on the presence of Δ_s but also on the relative phase between Δ_s

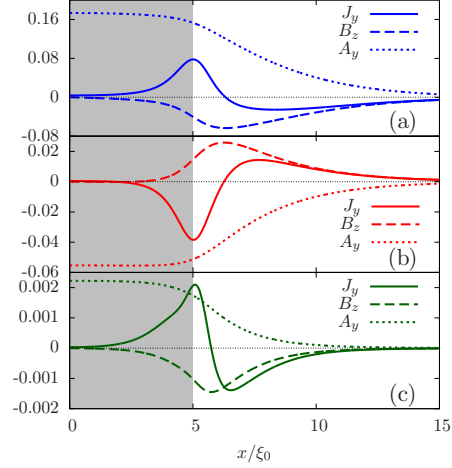


FIG. 6. Spatial dependencies of $J_y(x)$, $B_z(x)$, and $A_y(x)$ with Meissner screening for chiral p -, d - and f -wave pairing (from top to bottom), in the presence of a rough surface in a region of width $W = 5\xi_0$ and with $\ell_p = \xi_0$.

and the bulk $d + id$ order parameter components. The phase is determined in GL by minimizing the free-energy term in Eq. (13). Also, for a spontaneous edge current discussion the frequency independent GL analysis seems more natural.

The noninversion of current in the chiral p -wave case [Fig. 4(d)] can also be understood within the GL framework. In the chiral p -wave case, without strong surface roughness, the GL current is dominated by $J_y \propto k_3(\Delta_2 \partial_x \Delta_1^* - c.c.) - k_4(\Delta_1^* \partial_x \Delta_2 - c.c.)$ with coefficients $k_3, k_4 > 0$ [5]. This remains true in the presence of strong surface disorder as disorder does not introduce any new frequency-independent order parameters since $\Sigma_{o.d.}(\omega_n)$ is completely odd in frequency. Disorder enhances the order parameter derivative term $\partial_x \Delta_1$, that also has an s -wave symmetry. Due to this enhancement, the magnitude of k_3 and k_4 become different ($k_3 = k_4$ without surface disorder) such that $k_3(\Delta_2 \partial_x \Delta_1^* - c.c.)$ dominates the current. Then, with the spatial profiles of Δ_1 and Δ_2 given in Fig. 4(a), it is easy to see that J_y remains positive in the presence of strong surface roughness, so there is no current inversion. The current in the chiral f -wave case can be understood similarly, but the analysis is more involved as order parameter derivatives higher than the first order are needed and therefore we do not elaborate on this here.

However, we should emphasize that the edge current inversion seen for chiral d -wave pairing in the continuum limit is not universal. Away from the continuum limit, the direction of the current can depend on surface orientation and microscopic details. For example, for chiral d -wave pairing on a triangular lattice, with the edge along the zigzag direction and the chemical potential near half-filling (see Appendix C), the current in the absence of disorder is opposite to that in the continuum limit. In this case, there is no current inversion due to the surface disorder. Furthermore, since the current inversion requires an induced s -wave component, even in the continuum limit with strong edge disorder, the effect is reduced if the s -wave channel is repulsive. In physical systems, unconventional

pairing is usually accompanied by a sufficiently strong short-range Coulomb interaction that leads to repulsive interactions in the s -wave channel. In Fig. 5 (green line with dots), we show the result of including s -wave repulsion self-consistently.

Finally, we discuss the effect of Meissner screening, which so far has been neglected. Figure 6 shows the $J_y(x)$, $B_z(x)$, and $A_y(x)$ obtained in the presence of Meissner screening. The major effect of the Meissner screening is to induce an additional sign change in $J_y(x)$ due to the diamagnetic current such that the total integrated current $\int_0^\infty J_y(x)dx \propto B_z(x = \infty) = 0$, as required by Eq. (7).

VI. CONCLUSION

To summarize, we have considered the effects of finite temperature, Meissner screening, and surface roughness on the spontaneous edge current for higher chirality superconductors in the continuum limit using the quasiclassical Eilenberger formalism. We find that the integrated edge current for higher chirality superconductors is finite at finite T , although it vanishes at $T = 0$ [5]. It achieves its maximum near $T = T_c/2$. The self-consistency of the superconducting order parameter was found to be crucial for understanding this temperature dependence. We also find that Meissner screening effects on the edge current are much weaker for the higher chirality superconductor, compared with that for the chiral p -wave case.

Furthermore, we have studied the rough surface effects on the edge current by modeling the surface roughness as an effective disorder scattering. Similar to Ref. [19], we have found that the edge current direction is inverted by the surface roughness in the chiral d -wave case. We ascribe the inverted edge current to a disorder induced subdominant s -wave pairing “order parameter” in the rough surface regime and explain the current inversion using the GL analysis.

However, we find that this current inversion is not universal beyond the continuum limit and can depend on microscopic details, such as the surface orientation and the filling level of the sample, as seen from our self-consistent lattice BdG calculations. Furthermore, since the current inversion requires the presence of an induced s -wave order parameter, the effect is suppressed by any repulsion in the s -wave channel. In general, s -wave repulsion is expected to be quite large for most unconventional superconductors. Consequently, the primary feature of edge currents in disordered chiral d -wave (as well as higher chirality) superconductors is that they are expected to be quite small, relative to the analogous chiral p -wave case, and the direction of the current is sensitive to microscopic details.

Experimentally, a direct study of the edge currents has been conducted only for the chiral p -wave superconductor candidate material Sr_2RuO_4 so far. However, as more and more candidate materials for higher chirality superconductivity, such as SrAsPt , doped Graphene, UPt_3 , and URu_2Si_2 , become available, similar searches for edge currents may be undertaken. Our results, especially the finite temperature behavior of the integrated current $I_y(T)$ and the nonuniversal aspect of the current inversion in the presence of disorder in the chiral d -wave pairing case, could be important for understanding these materials.

ACKNOWLEDGMENTS

We would like to thank John Berlinsky and Wen Huang for helpful discussions. This work is supported by Natural Sciences and Engineering Research Council of Canada (NSERC) and Canadian Institute for Advanced Research (CIFAR).

APPENDIX A: SPATIAL PROFILE OF THE EDGE CURRENT WITHOUT MEISSNER SCREENING

In this Appendix, we show the spatial profiles of the $T = 0$ spontaneous edge currents for different pairing channels. Since at $T = 0$, the number of Matsubara frequencies in the numerical calculation diverges, we use $T = 0.02T_c$ to approximate $T = 0$. Unless specified otherwise, the pairing energy cutoff is chosen to be $\omega_c = 10T_c$. The spatial profile of the pairing components are shown in Figs. 7(a)–7(c). In all cases, the pairing component that is odd under $k_x \rightarrow -k_x$ drops to zero at the edge while the other component (even under x inversion), is enhanced near the edge [10].

Figures 7(d)–7(f) show the spatial profile of the spontaneous edge current density and the induced local magnetic field. For chiral m -wave pairing, the current density changes sign $|m| - 1$ times along the x direction [the second sign change for the chiral f -wave can not be resolved in Fig. 7(f) because the current magnitude is too small]. This results from the $|m|$ branches of edge states carrying the edge current with different signs and different length scales (see Fig. 8 for the chiral d -wave pairing, for example). Since chiral p -wave has a single edge mode, its edge current does not change sign and the integrated edge current can be sizable; while for higher chirality, the integrated edge current is negligible due to the multiple sign changes and vanishes at $T = 0$. This fact has been emphasized in previous studies [5,7]. The edge currents

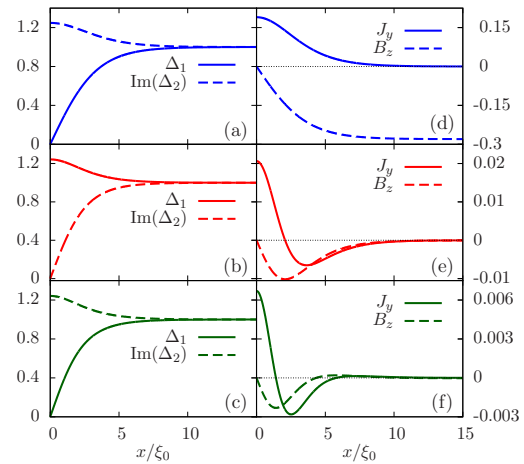


FIG. 7. (a)–(c) Spatial dependence of Δ_1 and $\text{Im}(\Delta_2)$ with specular surface for chiral p -, d - and f -waves, respectively. (d)–(f) Spatial dependence of the edge current $J_y(x)$ and the induced $B_z(x)$ with specular surface for different chiral pairing channels. Note the different vertical scales in (d)–(f). Meissner screening is not taken into account. $T = 0.02T_c$.

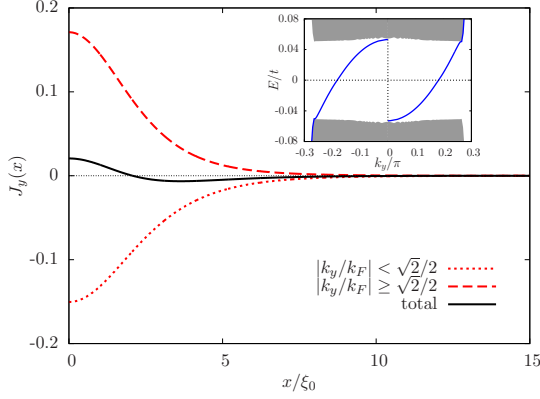


FIG. 8. Decomposition of the current density for the chiral d -wave pairing into different branches (i.e., different k_y ranges). Inset: edge state energy dispersion for a chiral d -wave superconductor obtained from a lattice BdG calculation; the horizontal axis is k_y/π ; the two blue solid lines are edge state dispersions while the grey shaded regime represent the bulk state energy spectrum.

are carried not only by the chiral Majorana edge modes but also by the bulk scattering states, which partially cancel the edge mode current [17]. However, for a qualitative understanding of the edge current, one often can focus on the edge mode contributions only.

Figures 7(d)–7(f) also shows that the bulk magnetic field induced by the edge current vanishes at $T = 0$ for chiral d - and f -waves. This is consistent with the total current integrating to zero at $T = 0$.

APPENDIX B: INTEGRATED EDGE CURRENTS FOR A UNIFORM SUPERCONDUCTING ORDER PARAMETER AND NO SCREENING

For a uniform superconducting order parameter and no vector potential \mathbf{A} , the Eilenberger equation can be solved analytically [6,10,18,31–33]. Decomposing the quasiclassical Green’s function matrix \hat{g} in terms of Nambu particle-hole Pauli matrices, we can write $\hat{g} = g_1 \hat{\tau}_1 + g_2 \hat{\tau}_2 + g_3 \hat{\tau}_3$, with [6,18,32]

$$g_3(\theta_{\mathbf{k}}, x; \omega_n) = \frac{\omega_n}{\lambda} + \frac{\Delta_1}{\lambda} \frac{\omega_n \Delta_1 - i s \lambda \Delta_2}{\omega_n^2 + \Delta_2^2} e^{-2 \frac{\lambda}{|v_{F_x}|} x}, \quad (\text{B1})$$

where $s \equiv \text{sgn}(v_{F_x}) = \text{sgn}(\cos \theta_{\mathbf{k}})$, and $\lambda = \sqrt{\omega_n^2 + \Delta^2}$, $\Delta_1 \equiv \Delta_1(\theta_{\mathbf{k}})$ and $\Delta_2 \equiv \Delta_2(\theta_{\mathbf{k}})$ are the vanishing and enhanced superconducting order parameter components, respectively. For example, for chiral p -wave, $\Delta(\theta_{\mathbf{k}}) = \Delta(\cos \theta_{\mathbf{k}} + i \sin \theta_{\mathbf{k}})$, $\Delta_1 = \Delta \cos \theta_{\mathbf{k}}$, and $\Delta_2 = \Delta \sin \theta_{\mathbf{k}}$; while for chiral d -wave, $\Delta(\theta_{\mathbf{k}}) = \Delta(\cos 2\theta_{\mathbf{k}} + i \sin 2\theta_{\mathbf{k}})$, $\Delta_1 = \Delta \sin 2\theta_{\mathbf{k}}$ while $\Delta_2 = \Delta \cos 2\theta_{\mathbf{k}}$. Note that the definitions of Δ_1 and Δ_2 here are different from those used elsewhere in the paper.

The local current density $J_y(x, T)$ can be computed from Eq. (6) with the energy cutoff ω_c sent to infinity and the integrated current is $I_y(T) = \int_0^\infty J_y(x, T) dx$. In Ref. [5], it was shown that $I_y(T = 0) = 0$ for any nonchiral- p -wave

pairing. Here we give the expression of $I_y(T)$. This finite T expression of $I_y(T)$ has been derived for the chiral p -wave pairing in Ref. [18]. Our derivations parallel those and we only give the final result here:

$$\frac{I_y(T)}{e N_F v_F^2 / 8} = 2 \left\langle \frac{v_{F_x} v_{F_y}}{v_F v_F} \Delta_1 \Delta_2 \left\{ \pi \frac{\tanh\left(\frac{|\Delta_2|}{2T}\right)}{|\Delta_1| |\Delta_2|} - 2 \int_0^\infty dy \frac{\tanh\left(\frac{|\Delta|}{2T} \cosh y\right)}{\Delta_2^2 \sinh^2 y + \Delta_1^2 \cosh^2 y} \right\} \right\rangle_{\theta_{\mathbf{k}}}. \quad (\text{B2})$$

Inside the $\{\dots\}$, the first term comes from a complex contour integral around the pole on the complex ω_n plane at $\omega_n = i|\Delta_2|$, and represents the edge mode contribution; while the second term originates from the branch cut on the complex ω_n plane running from $\omega_n = i|\Delta|$ to $\omega_n = i\infty$. The branch cut contribution comes from the bulk scattering states with quasiparticle energies $\geq |\Delta|$. In general, the two contributions can both be nonzero.

In Eq. (B2), whether $I_y(T) = 0$ or not is solely determined by the rotational symmetry of the integrand with respect to $\theta_{\mathbf{k}}$. For pairing with $\Delta_{\mathbf{k}} = \Delta(\cos m\theta_{\mathbf{k}} + i \sin m\theta_{\mathbf{k}})$, in the integrand of Eq. (B2), the combination of $\Delta_1 \Delta_2 \{\dots\}$ is invariant under $2|m|$ -fold rotation of $\theta_{\mathbf{k}}$; on the other hand, the velocity product $v_{F_x} v_{F_y}$ is twofold rotation symmetric. Hence, the entire integrand can be decomposed into a sum of two terms which are invariant under either $2|m| + 2$ or $2|m| - 2$ fold $\theta_{\mathbf{k}}$ rotation. Since the integral vanishes as long as $2|m| + 2 \neq 0$ and $2|m| - 2 \neq 0$, we conclude that, for any $|m| \neq 1$, $I_y(T) \equiv 0$ at any finite T , for the case of a uniform superconducting order parameter.

Although the above results in this section are derived for a uniform order parameter, we note that, at $T = 0$, the bulk scattering state contribution of $I_y(T = 0)$, I_y^{bulk} , remains zero even when the order parameter is self-consistently determined. This is because I_y^{bulk} can be written as $I_y^{\text{bulk}} \propto \int_{-\pi/2}^{\pi/2} Q_m(\theta_{\mathbf{k}}) \sin \theta_{\mathbf{k}} \cos \theta_{\mathbf{k}} d\theta_{\mathbf{k}}$ [5], where the factor $\sin \theta_{\mathbf{k}} \cos \theta_{\mathbf{k}} d\theta_{\mathbf{k}}$ comes from $k_y dk_y$ and $Q_m(\theta_{\mathbf{k}})$ is the accumulated charge near the surface due to the phase shift of all filled bulk scattering states at $\theta_{\mathbf{k}}$. As shown in Refs. [17,34], $Q_m(\theta_{\mathbf{k}})$ only depends on the asymptotic phase of the order parameter in the bulk, which is unaffected by the presence of the surface. Therefore, $I_y^{\text{bulk}}(T = 0) = 0$ remains even when the spatial variations of the order parameter near the surface is taken into account.

APPENDIX C: SELF-CONSISTENT BDG CALCULATION OF EDGE CURRENT WITH SURFACE ROUGHNESS FOR CHIRAL d -WAVE PAIRING

Here, we show that the current inversion due to the surface roughness seen in the continuum limit for the chiral d -wave pairing is nonuniversal and is not always present when lattice effects are included. The existence of the current inversion depends on microscopic details, such as the edge orientation, band structure and carrier doping levels.

We consider a two-dimensional triangular lattice with the following BdG Hamiltonian

$$H = \sum_{(\mathbf{r}, \mathbf{r}')} [-t c_{\mathbf{r}}^\dagger c_{\mathbf{r}'} + \Delta_{\mathbf{r}, \mathbf{r}'} c_{\mathbf{r}}^\dagger c_{\mathbf{r}'}^\dagger + h.c.] - \sum_{\mathbf{r}} \mu_{\mathbf{r}} c_{\mathbf{r}}^\dagger c_{\mathbf{r}}, \quad (\text{C1})$$

where $(\mathbf{r}, \mathbf{r}')$ means only nearest-neighbor (NN) hopping, t , and pairing, $\Delta_{\mathbf{r}, \mathbf{r}'}$, are considered and $\mu_{\mathbf{r}}$ is the local chemical potential. For the clean system without edges, the normal state energy dispersion is given by $\epsilon_{\mathbf{k}} = -2t[\cos k_x + 2 \cos(\sqrt{3}k_y/2) \cos(k_x/2)]$, where the lattice spacing is set to unity. We have chosen the x direction along one of the three lattice bond directions.

The chiral d -wave superconducting order parameter is defined on each NN bond, $\frac{\mathbf{r}+\mathbf{r}'}{2}$, as $\Delta_{\mathbf{r}, \mathbf{r}'} = \Delta(\frac{\mathbf{r}+\mathbf{r}'}{2}) e^{i2 \text{Arg}[(x'-x)+i(y'-y)]}$. Without edges and disorder, $\Delta(\frac{\mathbf{r}+\mathbf{r}'}{2}) \equiv \Delta_0$ (a constant), and the order parameter in \mathbf{k} space is $\Delta_{\mathbf{k}} = \Delta_0[\cos k_x - \cos(\sqrt{3}k_y/2) \cos(k_x/2)] + i\Delta_0\sqrt{3} \sin(\sqrt{3}k_y/2) \sin(k_x/2)$. In the presence of edges, the order-parameter magnitude $\Delta(\frac{\mathbf{r}+\mathbf{r}'}{2})$ becomes position dependent; however, we keep the phase $e^{i2 \text{Arg}[(x'-x)+i(y'-y)]}$ the same to ensure the pairing is chiral d -wave. $\Delta_{\mathbf{r}, \mathbf{r}'}$ is determined self-consistently within BdG (details can be found in Refs. [6,23]).

Surface roughness is modeled by adding a random impurity potential $V_{\mathbf{r}}^{\text{imp}}$ ($\mu_{\mathbf{r}} = \mu + V_{\mathbf{r}}^{\text{imp}}$) to sites within a width W of the edge. The impurity density in the rough regime is $n_{\text{imp}} = 0.2$ per lattice site and $V_{\mathbf{r}}^{\text{imp}}$ is uniformly distributed in the range $[-V^{\text{imp}}, V^{\text{imp}}]$. The current calculated is averaged over different impurity configurations.

We consider two different types of edges of the triangular lattice, straight and zigzag, and use periodic boundary conditions for the direction parallel to the edges. The current along each type of edge, denoted as J_{\parallel} , is calculated for two different filling levels, $\mu = 0$ (half-filling) and $\mu = -3t$; the results are shown in Fig. 9. For straight edges, there is an edge current inversion due to the surface roughness at both $\mu = 0t$ and $\mu = -3t$; while for zigzag edges, the current inversion is seen only at $\mu = -3t$, not at $\mu = 0$. In the specular surface (right edge of Fig. 9) case, the $\mu = 0$ edge current of the straight edge and that of the zigzag edge flow in opposite directions. Similar results have been observed for chiral p -wave pairing in Ref. [35]. Consequently, the direction of the current for an ideal edge and the presence of current inversion due to disorder both are sensitive to microscopic details.

APPENDIX D: GINZBURG-LANDAU ANALYSIS OF $d_{x^2-y^2} + id_{xy}$ WITH SUB-DOMINANT s -WAVE PAIRING

To understand the role in current reversal of subdominant s -wave pairing Δ_s induced near the surface of the $d_{x^2-y^2} + id_{xy}$ superconductor, we derive the GL free energy from the anomalous Green's functions, f and \bar{f} , obtained from the Eilenberger equations. For the half-infinite plane, the derivation closely follows that for $p_x + ip_y$ pairing in Ref. [10]. Hence, in the following, we only give key steps that are different from Ref. [10].

The GL free energy is an expansion in terms of

$$\frac{|\Delta|}{T} \equiv \frac{\max\{|\Delta_s|, |\Delta_1|, |\Delta_2|\}}{T}, \quad \frac{D}{T} \equiv \frac{|v_{Fx}| \partial_x}{T}, \quad (\text{D1})$$

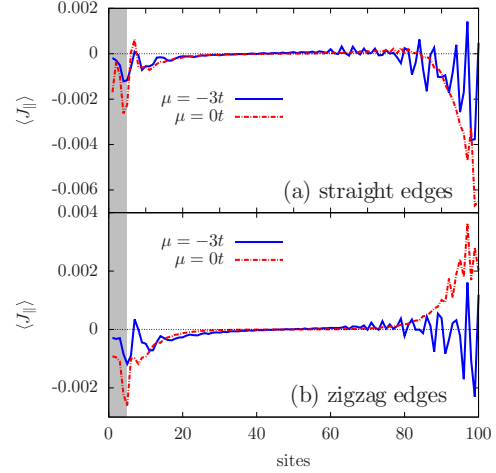


FIG. 9. Edge currents for the chiral d -wave pairing obtained from self-consistent BdG on a triangular lattice with different edge directions and chemical potentials. The shaded regime on the left has surface roughness, while the right surface is specular without disorder. We choose the rough regime width to be $W = 5$ lattice sites. A relatively larger temperature $T = 0.1T_c$ has been chosen to reduce the Friedel oscillations in the current. The impurity potential strength, $V^{\text{imp}} = 15t$, and the impurity density, $n_{\text{imp}} = 0.2$ per site, are large such that the effective local mean free path is short, same as in the Eilenberger calculation, where current reversal is seen.

near $T = T_c$, where both ratios are small. However, we expect qualitative features, such as the relative phase of Δ_s , to survive at low temperature. f and \bar{f} can be expanded in powers of $|\Delta|/T$ and D/T and has been done up to the fifth order in Eq. (A.6) of Ref. [10]. The derivation here becomes different starting at the form of the order parameter

$$\Delta = \Delta_s + \Delta_1 \cos 2\theta_{\mathbf{k}} + \Delta_2 \sin 2\theta_{\mathbf{k}}, \quad (\text{D2})$$

where Δ_s , Δ_1 , and Δ_2 are the $\theta_{\mathbf{k}}$ independent parts of the s , $d_{x^2-y^2}$, and id_{xy} order parameters. They are complex and spatially dependent. They satisfy the following BCS gap equations,

$$\begin{pmatrix} \Delta_s \\ \Delta_1 \\ \Delta_2 \end{pmatrix} = \pi T \sum_{0 < \omega_n < \omega_c} \int_{-\pi}^{\pi} \frac{d\theta_{\mathbf{k}}}{2\pi} \begin{pmatrix} V_s \\ 2V_d \cos 2\theta_{\mathbf{k}} \\ 2V_d \sin 2\theta_{\mathbf{k}} \end{pmatrix} [f(\theta_{\mathbf{k}}, x; \omega_n) + \bar{f}^*(\theta_{\mathbf{k}}, x; \omega_n)], \quad (\text{D3})$$

where $V_s > 0$ and $V_d > 0$ are the attractive interactions for s and $d + id$, respectively. Substituting the expressions of f and \bar{f} from Eq. (A.6) of Ref. [10] into the above BCS gap equations, we obtain three coupled equations for Δ_s , Δ_1 , and Δ_2 up to third order in the total power of $|\Delta|/T$ and D/T . These equations should be reproduced by the GL free-energy \mathcal{F} through a Euler-Lagrange equation [10].

Omitting derivation details, the final results for \mathcal{F} are $\mathcal{F} \propto \mathcal{F}_2 + \mathcal{F}_4$ with

$$\begin{aligned} \mathcal{F}_4 = & +4A_4 \{ |\Delta_s|^4 + \frac{3}{8}(|\Delta_1|^4 + |\Delta_2|^4) + 2|\Delta_s|^2(|\Delta_1|^2 + |\Delta_2|^2) + \frac{1}{2}|\Delta_1|^2|\Delta_2|^2 \\ & + \frac{1}{2}(\Delta_s^*)^2[\Delta_1^2 + \Delta_2^2] + \frac{1}{2}\Delta_s^2[(\Delta_1^*)^2 + (\Delta_2^*)^2] + \frac{1}{8}[\Delta_2^2(\Delta_1^*)^2 + (\Delta_2^*)^2\Delta_1^2] \\ & + 2|D_x\Delta_s|^2 + |D_x\Delta_1|^2 + |D_x\Delta_2|^2 + (D_x\Delta_s^*D_x\Delta_1 + D_x\Delta_sD_x\Delta_1^*) \}, \end{aligned} \quad (\text{D4a})$$

with $D_x \equiv \frac{\partial}{\partial x}$ and $A_4 \equiv \frac{1}{4} \frac{2^3-1}{2^3} \frac{\zeta(3)}{(\pi T)^3}$. Here $\zeta(z)$ is the Riemann zeta function. \mathcal{F}_2 is the second-order term which is not shown, as it is irrelevant to our discussion. In \mathcal{F}_4 , the last term involves mixed gradients of Δ_s and Δ_1 . This term has been discussed in Refs. [29,30,36]. This term can induce a nonzero Δ_s where $\partial_x \Delta_1 \neq 0$ and determines the phase of Δ_s relative to Δ_1 and Δ_2 . In addition to the mixed gradient term, there are other terms in \mathcal{F}_4 , such as $\Delta_s^2(\Delta_1^*)^2 + c.c.$, that can also affect the phase of Δ_s . However, they are higher order for a small, spatially varying Δ_s .

There are additional mixed gradients terms that are absent for a y -translational invariant system. However, they enter

in the current and can be obtained from the one in \mathcal{F}_4 by fourfold rotation symmetries or can be derived as in Ref. [36]. From Ref. [36], these additional mixed gradient terms are

$$\begin{aligned} & -4A_4(D_y\Delta_s^*D_y\Delta_1 + D_y\Delta_sD_y\Delta_1^*), \\ & +4A_4(D_x\Delta_s^*D_y\Delta_2 + D_y\Delta_s^*D_x\Delta_2 + c.c.). \end{aligned} \quad (\text{D5})$$

The important terms for the spontaneous current discussion in the main text are those from the second line. Other mixed gradient terms do not contribute a spontaneous current along the y direction for the half-infinite geometry that we considered.

-
- [1] C. Beenakker, *Annu. Rev. Condens. Matter Phys.* **4**, 113 (2013).
[2] C. Kallin, *Rep. Prog. Phys.* **75**, 042501 (2012).
[3] C. Kallin and J. Berlinsky, *Rep. Prog. Phys.* **79**, 054502 (2016).
[4] X.-L. Qi and S.-C. Zhang, *Rev. Mod. Phys.* **83**, 1057 (2011).
[5] W. Huang, E. Taylor, and C. Kallin, *Phys. Rev. B* **90**, 224519 (2014).
[6] W. Huang, S. Lederer, E. Taylor, and C. Kallin, *Phys. Rev. B* **91**, 094507 (2015).
[7] Y. Tada, W. Nie, and M. Oshikawa, *Phys. Rev. Lett.* **114**, 195301 (2015).
[8] G. E. Volovik, *JETP Lett.* **100**, 742 (2015).
[9] T. Scaffidi and S. H. Simon, *Phys. Rev. Lett.* **115**, 087003 (2015).
[10] M. Matsumoto and M. Sigrist, *J. Phys. Soc. Jpn.* **68**, 994 (1999).
[11] J. R. Kirtley, C. Kallin, C. W. Hicks, E.-A. Kim, Y. Liu, K. A. Moler, Y. Maeno, and K. D. Nelson, *Phys. Rev. B* **76**, 014526 (2007).
[12] C. W. Hicks, J. R. Kirtley, T. M. Lippman, N. C. Koshnick, M. E. Huber, Y. Maeno, W. M. Yuhasz, M. B. Maple, and K. A. Moler, *Phys. Rev. B* **81**, 214501 (2010).
[13] P. J. Curran, S. J. Bending, W. M. Desoky, A. S. Gibbs, S. L. Lee, and A. P. Mackenzie, *Phys. Rev. B* **89**, 144504 (2014).
[14] A. P. Mackenzie, T. Scaffidi, C. W. Hicks, and Y. Maeno, *Quantum Mater.* **2**, 40 (2017).
[15] M. Ishikawa, *Prog. Theor. Phys.* **57**, 1836 (1977).
[16] T. Kita, *J. Phys. Soc. Jpn.* **67**, 216 (1998).
[17] M. Stone and R. Roy, *Phys. Rev. B* **69**, 184511 (2004).
[18] J. A. Sauls, *Phys. Rev. B* **84**, 214509 (2011).
[19] S.-I. Suzuki and Y. Asano, *Phys. Rev. B* **94**, 155302 (2016).
[20] G. Eilenberger, *Z. Phys. A Hadrons Nucl.* **214**, 195 (1968).
[21] P. E. C. Ashby and C. Kallin, *Phys. Rev. B* **79**, 224509 (2009).
[22] Y. Nagato, S. Higashitani, and K. Nagai, *J. Phys. Soc. Jpn.* **80**, 113706 (2011).
[23] S. Lederer, W. Huang, E. Taylor, S. Raghu, and C. Kallin, *Phys. Rev. B* **90**, 134521 (2014).
[24] S. V. Bakurskiy, N. V. Klenov, I. I. Soloviev, M. Y. Kupriyanov, and A. A. Golubov, *Supercond. Sci. Technol.* **30**, 044005 (2017).
[25] N. Schopohl, *arXiv:cond-mat/9804064* (1998).
[26] M. Sigrist and K. Ueda, *Rev. Mod. Phys.* **63**, 239 (1991).
[27] B. Horovitz and A. Golub, *Phys. Rev. B* **68**, 214503 (2003).
[28] S.-I. Suzuki and Y. Asano, *J. Phys.: Conf. Ser.* **807**, 102001 (2017).
[29] P. I. Soininen, C. Kallin, and A. J. Berlinsky, *Phys. Rev. B* **50**, 13883 (1994).
[30] A. J. Berlinsky, A. L. Fetter, M. Franz, C. Kallin, and P. I. Soininen, *Phys. Rev. Lett.* **75**, 2200 (1995).
[31] M. Matsumoto and H. Shiba, *J. Phys. Soc. Jpn.* **64**, 3384 (1995).
[32] M. Matsumoto and H. Shiba, *J. Phys. Soc. Jpn.* **64**, 4867 (1995).
[33] M. Matsumoto and H. Shiba, *J. Phys. Soc. Jpn.* **65**, 2194 (1996).
[34] J. Goldstone and F. Wilczek, *Phys. Rev. Lett.* **47**, 986 (1981).
[35] A. Bouhon and M. Sigrist, *Phys. Rev. B* **90**, 220511 (2014).
[36] Q.-H. Wang, Z. D. Wang, and Q. Li, *Phys. Rev. B* **60**, 15364 (1999).

Chapter 4

Spin-orbit coupling and spin-triplet pairing symmetry in Sr_2RuO_4

4.1 Preface

Spin-orbit coupling (SOC) plays a crucial role in determining the pseudospin-triplet pairing states, an issue of importance to superconducting SRO, where the pairing symmetry is still an open question. A systematic and complete treatment of this issue in SRO has been lacking. Here we present a thorough study of how SOC lifts the degeneracy among different p -wave pairing states in a widely used microscopic model for SRO.

We first present a complete Ginzburg-Landau (GL) free energy analysis of the SOC effect on the pseudospin-triplet state for a general 2D model with D_{4h} point group. The presence of SOC breaks both the full pseudospin $SU(2)$ rotation and spatial D_{4h} symmetries. As a result, there are five possible SOC-induced GL free energy terms in quadratic order of the superconducting OP. See Appendix B for details. Depending on the symmetries of detailed microscopic models, some of these terms may or may not appear.



We then focus on a widely used 2D microscopic model for SRO and identify

the terms that lift the degeneracy among different p -wave states based on a symmetry analysis. A theme that emerges from this study is that the breaking of $SU(2)$ rotation symmetry in pseudospin space depends on not only the presence of SOC but also other ingredients of the microscopic Hamiltonian, for example, the interorbital hybridization, t''' , and/or Hund's coupling, J . We find that the dominant pairing is always helical rather than chiral. The analytic results are further supported by our weak-coupling RG and RPA numerical calculations. In addition, our numerical calculations show that nodal s' - or $d_{x^2-y^2}$ -wave pairing would take over the helical state beyond the weak-coupling limit.

We also generalize our analysis to a 3D model for SRO and show that the interorbital hybridizations, in addition to the t''' in the 2D model, do not help stabilize chiral p -wave pairing states.

Our analysis resolves the discrepancies regarding the relative stability between helical and chiral p -wave pairing states in previous studies. Since the analysis is based on the symmetries of the model, it can provide a guide to future studies. Subsequent studies on the leading superconducting instabilities of SRO in Refs.[118, 97, 137, 119, 138] based on similar SRO models in both 2D and 3D are consistent with this study. Furthermore, our analysis can be adapted to study the effect of SOC on other multi-orbital spin-triplet superconductors.

4.2 Publication

Spin-orbit coupling and spin-triplet pairing symmetry in Sr₂RuO₄Zhiqiang Wang ^{1,2}, Xin Wang ¹, and Catherine Kallin¹¹*Department of Physics and Astronomy, McMaster University, Hamilton, Ontario, Canada L8S 4M1*²*James Franck Institute, University of Chicago, Chicago, Illinois 60637, USA*

(Received 6 November 2019; revised manuscript received 20 January 2020; accepted 22 January 2020; published 7 February 2020)

Spin-orbit coupling (SOC) plays a crucial role in determining the spin structure of an odd parity pseudospin-triplet Cooper pairing state. Here, we present a thorough study of how SOC lifts the degeneracy among different p -wave pseudospin-triplet pairing states in a widely used microscopic model for Sr₂RuO₄, combining a Ginzburg-Landau (GL) free energy expansion, a symmetry analysis of the model, and numerical weak-coupling renormalization group (RG) and random phase approximation (RPA) calculations. These analyses are then used to critically re-examine previous numerical results on the stability of chiral p -wave pairing. The symmetry analysis can serve as a guide for future studies, especially numerical calculations, on the pairing instability in Sr₂RuO₄ and can be useful for studying other multiband spin-triplet superconductors where SOC plays an important role.

DOI: [10.1103/PhysRevB.101.064507](https://doi.org/10.1103/PhysRevB.101.064507)**I. INTRODUCTION**

Understanding an unconventional superconductor requires identifying and understanding both its superconducting order parameter symmetry and the pairing mechanism. The two are intimately connected. In Sr₂RuO₄, both of these are still not well understood. Early experiments, including muon spin relaxation [1], NMR [2], Polar Kerr effect [3] measurements, point toward a spin-triplet chiral p -wave pairing [4,5], which is a two-dimensional (2D) analog of the A phase of helium ³He [6] and is potentially useful for topological quantum computing [7,8].

However, it is difficult to reconcile the spin-triplet chiral p -wave picture with several other experiments [9]. Chiral edge currents have been predicted for the chiral p -wave pairing state but not detected [10,11]; splitting of the superconducting transition temperature T_c in the presence of an in-plane magnetic field or a uniaxial strain [12,13] is expected but not found. Recent NMR experiments [14,15] report a significant drop of the spin susceptibility in the superconducting phase measured in an in-plane magnetic field, which contradicts previous measurements [2] and suggest either spin-triplet helical or singlet pairing, although strong spin-orbit coupling [16,17] can complicate the interpretation of the experimental data.

Most theoretical studies [18,19] on the pairing mechanism are connected to spin or charge fluctuation mediated superconductivity, inspired by work on ³He [6]. However, spin fluctuations in Sr₂RuO₄ are complicated due to the multi-orbital nature of its normal state. The normal state of Sr₂RuO₄ contains two quasi-1D α and β bands, derived mainly from the Ru t_{2g} d_{xz} , d_{yz} orbitals, and one quasi-2D band from the d_{xy} orbital. Although early on it was proposed that the superconductivity is dominated by one set of the three bands [20], more recent calculations suggest that superconductivity on the three bands is comparable and indicate that the three orbitals should

be treated simultaneously. A further complication in a microscopic analysis comes from the sizable spin-orbit coupling (SOC) which entangles the three orbital degrees of freedom with spin. The effect of SOC on the normal state Fermi surface (FS) has been emphasized previously in Ref. [16] and was recently found to be larger than previously thought [17]. However, the effect of SOC on the superconducting state is still poorly understood.

Understanding the effect of SOC on the superconducting phase is crucial to address the relative stability of chiral p -wave and helical p -wave pairing states. This is because in the absence of SOC, and in the weak-coupling limit, all spin-triplet p -wave pairing states are degenerate due to the unbroken spin rotation symmetry [21]. A mechanism to lift the degeneracy in the absence of SOC is to consider the spin fluctuation feedback effect due to the superconducting condensate itself, which spontaneously breaks the spin rotation symmetry and modifies the pairing interaction. This mechanism is responsible for the stability of the ³He A phase [6] and has been used to stabilize the chiral state in theories of Sr₂RuO₄. However, in a Ginzburg-Landau free energy expansion in terms of the superconducting order parameter near T_c , the feedback effect only appears at fourth-order; while the SOC effect can split T_c of different spin triplet states at quadratic order [21]. Therefore it is important to understand how the normal state SOC affects the stability of different pairing states.

The effect of SOC on the spin triplet pairing states in Sr₂RuO₄ has been studied previously in Refs. [21–28] semi-analytically to various degrees and included in different numerical calculations [18,29–31], using different models and approaches. However, a systematic and more complete treatment is lacking. Also, conflicting statements have been made regarding the degeneracy among different p -wave pairing states in the presence of SOC. In this paper, we present a complete Ginzburg-Landau free energy analysis of the

SOC effect on the superconducting state at quadratic order in the order parameter. Then we focus on a 2D three-band microscopic model with SOC and identify the terms that lift the degeneracy among different p -wave states based on a symmetry analysis of the model. The results are supplemented with numerical weak-coupling RG and RPA calculations [18,26]. This model has been adopted in different numerical calculations [18,24,26,27,29–33] under different approximations to determine the dominant pairing instability for Sr₂RuO₄. Our analysis shows that some of the previous numerical results obtained in certain parameter regimes are incorrect. Since our results are obtained largely based on symmetries of the model, they also apply beyond weak-coupling and provide a guide to future numerical calculations. Furthermore, some of the conclusions and analysis here can be applied to other multiband spin-triplet superconductors, where SOC is important for the pairing.

The rest of the paper is organized as follows. In Sec. II, a complete GL analysis of SOC effects on triplet states is presented. In Sec. III, we study the SOC induced GL free energy terms for Sr₂RuO₄ based on a widely studied 2D three-band microscopic model using analytical symmetry analyses and numerical weak-coupling RG calculations. In Sec. IV, we reexamine the chiral p -wave instability in Sr₂RuO₄, where we provide a new phase diagram calculated within the RPA for the microscopic model, and also generalize the 2D analysis to 3D. Sec. V contains our conclusions. Some details of the derivations are relegated to Appendices, including details on the extension of this work to 3D models of Sr₂RuO₄.

II. GENERAL GINZBURG-LANDAU ANALYSIS

In the presence of SOC, spin is not a good quantum number. However, time reversal and inversion symmetries still ensure a twofold degeneracy at each \mathbf{k} point in the Brillouin zone, which can be used to define a pseudospin and to classify all possible pairing states into pseudospin singlet and triplet sectors. Here, we focus on pseudospin triplet p -wave pairing states.

For a general pseudospin triplet state the order parameter is a 2×2 matrix,

$$\hat{\Delta}(\mathbf{k}) \equiv \sum_{\mu=\{x,y,z\}} \sum_{j=\{x,y\}} d_j^\mu \sigma_\mu i\sigma_y \psi_j(\mathbf{k}). \quad (1)$$

where σ_μ are Pauli matrices in pseudospin space; $\psi_j(\mathbf{k})$ are two basis functions in \mathbf{k} space that transform like k_x and k_y under the D_{4h} point group.

In the absence of SOC, the GL free energy at quadratic order in the superconducting order parameter is

$$f_2^0 = \alpha^0(T) \left\langle \frac{1}{2} \text{Tr}[\hat{\Delta}^\dagger(\mathbf{k})\hat{\Delta}(\mathbf{k})] \right\rangle_{\text{FS}} \quad (2a)$$

$$= \alpha^0(T) \sum_{\mu=\{x,y,z\}} \sum_{j=\{x,y\}} |d_j^\mu|^2, \quad (2b)$$

where the superscript “0” indicates quantities defined for zero SOC. $\alpha^0(T) \propto (T_c^0 - T)$ and $\langle \dots \rangle_{\text{FS}}$ means averaged over the FS. The trace, $\text{Tr}[\dots]$, is performed in pseudospin space.

In general, the presence of SOC breaks both the full pseudospin SU(2) rotation and spatial D_{4h} symmetries. The

TABLE I. All possible SOC induced GL free energy terms at quadratic order in $\hat{\Delta}$ for pseudospin triplet pairing states of a 2D model. For 3D models there are additional terms, which can be found in Appendix C.

GL terms	Expressions in terms of d_j^μ
$f_2^{\text{SOC},1}$	$ d_x^z ^2 + d_y^z ^2$
$f_2^{\text{SOC},2}$	$(d_x^x)^* d_y^y + (d_y^y)^* d_x^x$
$f_2^{\text{SOC},3}$	$(d_y^x)^* d_x^y + (d_x^y)^* d_y^x$
$f_2^{\text{SOC},4}$	$ d_x^x ^2 + d_y^y ^2$
$f_2^{\text{SOC},5}$	$ d_x^y ^2 + d_y^x ^2$

remaining symmetry group for a 2D model of Sr₂RuO₄ is $D_{4h}^{\hat{\Delta}+\hat{S}} \otimes U(1)^C$, where $D_{4h}^{\hat{\Delta}+\hat{S}}$ is the D_{4h} point group whose symmetry operations act simultaneously on the spatial \mathbf{k} and pseudospin spaces. $U(1)^C$ is the charge U(1) gauge symmetry. Time-reversal and inversion symmetries are also assumed, although they might be spontaneously broken in the ground state. To derive the most general form of the GL free energy terms at quadratic order we consider all possible contractions of $(d_j^\mu)^* d_j^\nu$, viewed as a rank-4 tensor, such that the contracted results are a scalar that is invariant under all symmetry operations of $D_{4h}^{\hat{\Delta}+\hat{S}} \otimes U(1)^C$. This leads to five terms in the GL free energy, which are tabulated in Table I. Details of the derivation can be found in Appendix A.

We can also write the SOC induced terms in terms of $\hat{\Delta}$. When the pseudospin rotation symmetry is broken, order parameter products other than $\hat{\Delta}^\dagger \hat{\Delta}$, such as $\hat{\Delta}^\dagger \sigma_i \Delta$ and $\hat{\Delta}^\dagger \sigma_i \Delta \sigma_j$, can also appear in Eq. (2a) [34]. Considering all such combinations that are invariant under the symmetry group $D_{4h}^{\hat{\Delta}+\hat{S}} \otimes U(1)^C$ leads to the same conclusion that there are five independent terms in the GL free energy at quadratic order. The results can be found in Table IV of Appendix A.

Some of the terms in Table I have been identified previously [21–26,28], but Table I provides the most complete form of all possible SOC induced terms at quadratic order. These terms in general lift the degeneracy among different p -wave states, which belong to the five irreducible representations of the D_{4h} group and are classified in Table II. Depending on the symmetries of microscopic models, some of these terms may or may not appear. In the following, we focus on a particular 2D three-band interaction model [18], identify the

TABLE II. Irreducible representations (irrep.) of the $D_{4h}^{\hat{\Delta}+\hat{S}}$ point group. The order parameters are given for 2D models. Only the pseudospin triplet p -wave pairing states are considered. The first four irrep., $\{A_{1u}, A_{2u}, B_{1u}, B_{2u}\}$, give helical pairings that do not break time reversal symmetry; while the E_u irrep. supports two chiral states, $\hat{z}(k_x \pm ik_y)$, that spontaneously break time reversal symmetry.

irrep.	Order parameter
A_{1u}	$\mathbf{d}(\mathbf{k}) = \hat{x}k_x + \hat{y}k_y$
A_{2u}	$\mathbf{d}(\mathbf{k}) = \hat{x}k_y - \hat{y}k_x$
B_{1u}	$\mathbf{d}(\mathbf{k}) = \hat{x}k_x - \hat{y}k_y$
B_{2u}	$\mathbf{d}(\mathbf{k}) = \hat{x}k_y + \hat{y}k_x$
E_u	$\mathbf{d}(\mathbf{k}) = \hat{z}(k_x, k_y)$

SOC induced terms, and analyze how they affect the relative stability of different p -wave pairing states.

III. MICROSCOPIC DETERMINATION OF THE SOC INDUCED TERMS

We consider the microscopic model Hamiltonian,

$$H = H_K + V, \quad (3)$$

where H_K is the kinetic energy part that gives rise to the normal state Fermi surfaces, and V is the interaction. In addition to hopping terms, H_K contains a SOC term, which, written in \mathbf{k} space, is

$$2\eta \mathbf{L} \cdot \mathbf{S} = \eta \sum_{\ell, m, n=1,2,3} i \epsilon_{\ell mn} c_{\mathbf{k}, m, s}^\dagger \sigma_{ss}^\ell c_{\mathbf{k}, n, s'}, \quad (4)$$

where $\{1, 2, 3\} = \{d_{yz}, d_{xz}, d_{xy}\}$ orbitals, and $\{s, s'\}$ are the actual spins, not the pseudospins to be defined below. $\epsilon_{\ell mn}$ is the fully antisymmetric tensor and η is the SOC strength. c^\dagger (c) is the electron creation (annihilation) operator.

Following Ref. [18], we write H_K in the basis $\Psi(\mathbf{k}) = [c_{\mathbf{k}, 1, \uparrow}; c_{\mathbf{k}, 2, \uparrow}; c_{\mathbf{k}, 3, \downarrow}; c_{\mathbf{k}, 1, \downarrow}; c_{\mathbf{k}, 2, \downarrow}; c_{\mathbf{k}, 3, \uparrow}]^T$, such that it is block diagonal

$$H_K(\mathbf{k}) = \begin{pmatrix} H_{\uparrow\uparrow}(\mathbf{k}) & 0 \\ 0 & H_{\downarrow\downarrow}(\mathbf{k}) \end{pmatrix}, \quad (5)$$

where

$$H_{ss}(\mathbf{k}) = \begin{pmatrix} \epsilon_{yz}(\mathbf{k}) & g(\mathbf{k}) + is\eta & -s\eta \\ g(\mathbf{k}) - is\eta & \epsilon_{xz}(\mathbf{k}) & i\eta \\ -s\eta & -i\eta & \epsilon_{xy}(\mathbf{k}) \end{pmatrix}. \quad (6)$$

ϵ_{yz} , ϵ_{xz} , and ϵ_{xy} describe intraorbital hoppings; while $g(\mathbf{k})$ is the only interorbital hopping for a 2D model.

The interaction [18] we consider is a multiorbital on-site Kanamori-Hubbard type interaction

$$\begin{aligned} V = & \frac{U}{2} \sum_{i,a} n_{i,a,\uparrow} n_{i,a,\downarrow} + \frac{U'}{2} \sum_{i,a \neq b,s,s'} n_{i,a,s} n_{i,b,s'} \\ & + \frac{J}{2} \sum_{i,a \neq b,s,s'} c_{ias}^\dagger c_{ibs'}^\dagger c_{ias'} c_{ibs} \\ & + \frac{J'}{2} \sum_{i,a \neq b,s \neq s'} c_{ias}^\dagger c_{ias'}^\dagger c_{ibs'} c_{ibs}. \end{aligned} \quad (7)$$

$n_{i,a,s} \equiv c_{i,a,s}^\dagger c_{i,a,s}$ is the spin and orbital resolved electron density operator at site i . U (U') is the intraorbital (interorbital) repulsive Hubbard interaction. J is the Hund's coupling, and J' the pair hopping. The Hund's coupling term can be also written as [35] $-J \sum_{i,a \neq b} (\mathbf{S}_{i,a} \cdot \mathbf{S}_{i,b} + n_{i,a} n_{i,b}/4)$, where $\mathbf{S}_{i,a}$ is the orbital resolved electron spin vector operator at site i and $n_{i,a} = n_{i,a,\uparrow} + n_{i,a,\downarrow}$. The Kanamori-Hubbard interaction V is derived from the Coulomb interaction and is invariant under $SO(3)$ rotations in the t_{2g} d -orbital space, provided $J' = J$ and $U' = U - 2J$ [35]. Crystal field splitting in Sr_2RuO_4 in general lowers the symmetry of the interaction in the orbital space, which, however, does not affect our following discussions. Each of the four terms of V is $SU(2)$ spin rotational invariant. The repulsive V can give rise to Cooper pairing instabilities in non- s -wave channels [36].

A. Hamiltonian in the pseudospin basis

Using $a_{i,a,\sigma}^\dagger$ ($a_{i,a,\sigma}$) for electron creation (annihilation) operators with the pseudospin σ and orbital a at site i , we define

$$(a_{i,1,\sigma}^\dagger, a_{i,2,\sigma}^\dagger, a_{i,3,\sigma}^\dagger) \equiv (c_{i,1,\sigma}^\dagger, c_{i,2,\sigma}^\dagger, c_{i,3,\sigma}^\dagger), \quad (8)$$

where $\bar{\sigma} = \downarrow$ (\uparrow) if $\sigma = \uparrow$ (\downarrow). Written in the pseudospin basis, $\tilde{\Psi}(\mathbf{k}) = [a_{\mathbf{k},1,\uparrow}; a_{\mathbf{k},2,\uparrow}; a_{\mathbf{k},3,\uparrow}; a_{\mathbf{k},1,\downarrow}; a_{\mathbf{k},2,\downarrow}; a_{\mathbf{k},3,\downarrow}]^T$, the kinetic energy part $H_K(\mathbf{k})$ remains the same as in Eq. (6), whose $H_{\uparrow\uparrow}$ ($H_{\downarrow\downarrow}$) block can be identified with pseudospin \uparrow (\downarrow).

Rewriting the interaction V in Eq. (7) in terms of $\{a^\dagger, a\}$ and denoting the new interaction by \tilde{V} , we have

$$\tilde{V} = \tilde{V}_U + \tilde{V}_{U'} + \tilde{V}_J + \tilde{V}_{J'}, \quad (9)$$

where

$$\tilde{V}_U = \frac{U}{2} \sum_{i,a} n_{i,a,\uparrow} n_{i,a,\downarrow}, \quad (10a)$$

$$\tilde{V}_{U'} = \frac{U' - J/2}{2} \sum_{i,a \neq b,\sigma,\sigma'} n_{i,a,\sigma} n_{i,b,\sigma'}, \quad (10b)$$

$$\tilde{V}_J = -J \sum_i \left\{ \sum_{a \neq b} \mathbf{S}_{i,a} \cdot \mathbf{S}_{i,b} - 2 \sum_{a=\{1,2\}} [S_{i,a}^y S_{i,3}^y + S_{i,a}^z S_{i,3}^z] \right\}, \quad (10c)$$

$$\begin{aligned} \tilde{V}_{J'} = & \frac{J'}{2} \sum_{i,\sigma \neq \sigma'} \left\{ \sum_{a \neq b=\{1,2\}} - \sum_{a \neq b=\{2,3\}} - \sum_{a \neq b=\{1,3\}} \right\} \\ & a_{iao}^\dagger a_{iao'}^\dagger a_{ibo'} a_{ib\sigma}. \end{aligned} \quad (10d)$$

In these equations, all operators are in terms of $\{a^\dagger, a\}$: $n_{i,a,\uparrow} = a_{i,a,\uparrow}^\dagger a_{i,a,\uparrow}$, etc. In the following, we identify the terms in the Hamiltonian $H_K + \tilde{V}$ that breaks the pseudospin rotational symmetry.

B. Degeneracy at $g(\mathbf{k}) = J = J' = 0$

Although the presence of H_{SOC} breaks spin rotation symmetry in the normal state, it does not necessarily lead to a symmetry breaking in the pseudospin space and, therefore, the degeneracy among different pseudospin triplet p -wave pairing states may remain intact. In the current model, this is the case when both $g(\mathbf{k}) \equiv 0$ and $J = J' = 0$. This has been pointed out previously in Ref. [24] by a direct expansion of the effective interaction in the Cooper pairing channel in terms of the SOC constant η up to quadratic order. Here, we provide a proof purely based on symmetry.

First notice that H_K can be brought into a pseudospin $SU(2)$ invariant form by the following unitary transformation (written in the \mathbf{k} space)

$$\mathcal{U} : \{a_{\mathbf{k},1,\downarrow}^\dagger, a_{\mathbf{k},1,\downarrow}\} \rightarrow \{-a_{\mathbf{k},1,\downarrow}^\dagger, -a_{\mathbf{k},1,\downarrow}\}, \quad (11)$$

if there is no interorbital hopping term, i.e., $g(\mathbf{k}) \equiv 0$ in Eq. (6). In this case, under the \mathcal{U} transformation,

$$\tilde{H}_K \equiv \mathcal{U}^\dagger H_K \mathcal{U} = H_{\uparrow\uparrow} \otimes \sigma_0, \quad (12)$$

where σ_0 is the identity matrix in the pseudospin space.

When $J = J' = 0$, the \mathcal{U} transformation leaves \tilde{V} in Eq. (9) unchanged, which is pseudospin SU(2) rotational invariant since \tilde{V} and V share the same form. Therefore, if both $g(\mathbf{k}) \equiv 0$ and $J = J' = 0$, the whole microscopic Hamiltonian after the \mathcal{U} transformation,

$$\tilde{H} = \tilde{H}_K + \tilde{V}, \quad (13)$$

is pseudospin SU(2) invariant. Consequently, all p -wave pseudospin triplet pairing states resulting from the microscopic Hamiltonian are degenerate. This conclusion does not depend on how the microscopic model is treated, i.e., whether the pairing states are calculated in weak-coupling RG [18], RPA [29,30], or other methods.

C. SOC induced terms due to finite $g(\mathbf{k})$ but with $J = J' = 0$

When $g(\mathbf{k}) \neq 0$, after the \mathcal{U} transformation, the kinetic energy part of the Hamiltonian can be written as $\tilde{H}_K + \delta\tilde{H}_K$ with \tilde{H}_K given in Eq. (12) and

$$\delta\tilde{H}_K(\mathbf{k}) \equiv 2g(\mathbf{k})\{S_{12}^z(\mathbf{k}) + \text{H.c.}\}, \quad (14)$$

where $S_{12}^z(\mathbf{k}) \equiv 1/2 \sum_{\sigma,\sigma'} a_{\mathbf{k},1,\sigma}^\dagger \sigma_{\sigma,\sigma'}^z a_{\mathbf{k},2,\sigma'}$ is the interorbital pseudospin operator along the z direction. For $g(\mathbf{k})$, to be specific, we consider the nearest-neighbor interorbital hybridization as in Ref. [18], $g(\mathbf{k}) = -4t''' \sin k_x \sin k_y$, where t''' is the corresponding hopping integral.

Clearly, $\delta\tilde{H}_K(\mathbf{k})$ breaks the full pseudospin rotational symmetry. It contributes to the GL free energy a term which, to the first order in t'''/t , is

$$\delta\mathcal{F} = \langle \delta\tilde{H}_K(\mathbf{k}) \rangle = a_2 [f_2^{\text{SOC},2} - f_2^{\text{SOC},3}]. \quad (15)$$

$a_2 \propto t'''/t$, and the expressions of $f_2^{\text{SOC},2}$ and $f_2^{\text{SOC},3}$ are given in Table I. The average $\langle \dots \rangle$ is performed in a mean-field p -wave pairing state obtained at $t''' = 0$ and over the \mathbf{k} space. In arriving at this equation, we have used: (1) because of the $\sin k_x \sin k_y$ dependence in $g(\mathbf{k})$, only $(d_x^\mu)^* d_y^\nu$ type terms can appear in $\delta\mathcal{F}$, so that $\langle \dots \rangle$ does not vanish after the \mathbf{k} average; (2) $\delta\tilde{H}_K(\mathbf{k})$ has a remaining symmetry in the pseudospin space; it is invariant under pseudospin rotations about the z axis. Written in terms of the components of the $\hat{\Delta}$ matrix, $\delta\mathcal{F} = a_2(-i/2)\{\Delta_{\uparrow\uparrow,x}\Delta_{\uparrow\uparrow,y}^* - \Delta_{\downarrow\downarrow,x}\Delta_{\downarrow\downarrow,y}^* - \text{c.c.}\}$. The subscript ‘ x ’ indicates that the quantity transforms as k_x under the spatial D_{4h} group. This term has been identified in Refs. [24,28] using a quite different approach. Our derivation makes the microscopic symmetry origin of the term manifest.

Since $\delta\mathcal{F}$ in Eq. (15) preserves the pseudospin rotation symmetry in the xy plane, it splits the four p -wave helical states into two groups, $\{A_{1u}, A_{2u}\}$ and $\{B_{1u}, B_{2u}\}$. The two states in each group are related to each other by a fourfold pseudospin rotation about z . To leading order in t'''/t , the splitting of T_c between the two groups is $\delta T_c \propto |a_2| \propto |t'''/t|$. Since $\delta\mathcal{F}$ does not have any term that splits chiral states from helical states, the transition temperature of the chiral states, $T_c^{E_u}$, stays half way in between that of the two helical state groups, $T_c^{A_{1u}/A_{2u}}$ and $T_c^{B_{1u}/B_{2u}}$. We confirm these conclusions with a numerical weak-coupling RG calculation following Refs. [18,26]. The results are shown in Fig. 1. At larger t'''/t , the splitting between helical and chiral states has deviations from the linear dependence on t'''/t arising from higher

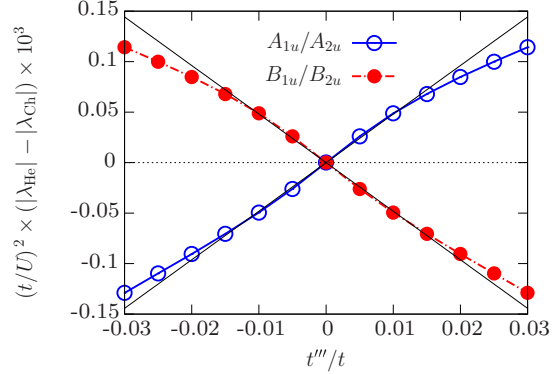


FIG. 1. Differences between eigenvalues of the effective two-particle interaction in the Cooper pairing channel computed within weak-coupling RG. Thin black lines are guides for the eye to show the linear behavior at small t'''/t . λ_{He} (λ_{Ch}) is the eigenvalue for p -wave helical (chiral) pairing states. The splitting, δT_c , of T_c between chiral and helical states is given by $\delta T_c/T_c \propto (|\lambda_{\text{He}}| - |\lambda_{\text{Ch}}|)$, to linear order in $\delta T_c/T_c$. The normal state band parameters, other than t''' and η , here and elsewhere, are identical to those in Ref. [18]. Here, we choose $\eta = 0.1t$ and $J/U = 0$.

order contributions of $\delta\tilde{H}_K(\mathbf{k})$ to $\delta\mathcal{F}$, which lead to terms, $f_2^{\text{SOC},4} + f_2^{\text{SOC},5}$ and $f_2^{\text{SOC},1}$, in $\delta\mathcal{F}$. These terms leave the degeneracy in each of two helical state groups intact since the pseudospin rotational symmetry around z remains; however, they make the relation $T_c^{E_u} = \{T_c^{A_{1u}/A_{2u}} + T_c^{B_{1u}/B_{2u}}\}/2$ only an approximation. Since in Sr_2RuO_4 , $|t'''|/t \sim \eta/t$ is small, we expect $T_c^{E_u} \approx \{T_c^{A_{1u}/A_{2u}} + T_c^{B_{1u}/B_{2u}}\}/2$ to hold, as seen in Fig. 1.

One conclusion of the above analysis is that the chiral pairing states are never stabilized by the t''' induced terms. A similar conclusion was obtained in Ref. [25] for a different interaction model within a mean-field analysis.

Since the relative stability between chiral and helical states will be affected by other SOC induced terms, which will be analyzed in detail in Sec. III D, it is important to understand the SOC dependence of $\delta\mathcal{F}$ in Eq. (15). Following Ref. [25], we go back to the original Hamiltonian before the \mathcal{U} transformation in terms of actual spin. To linear order in η/t , the change of the GL free energy due to nonzero SOC is given by $\delta\mathcal{F} = 2\eta(\mathbf{L} \cdot \mathbf{S})$, where the average $\langle \dots \rangle$ is evaluated in a mean field pairing state obtained at zero SOC. From the analysis of $\delta\tilde{H}_K(\mathbf{k})$ in pseudospin space, we know that $\delta\mathcal{F}$ is invariant under pseudospin rotations about z ; it is also invariant under actual spin rotations about z since the pseudospin and actual spin z directions are the same. Therefore, in $(\mathbf{L} \cdot \mathbf{S})$, $\langle L^x S^x + L^y S^y \rangle \equiv 0$. Hence,

$$\delta\mathcal{F} = 2\eta(L^z S^z) = i\eta(n_{12}^{\uparrow\uparrow} - n_{12}^{\downarrow\downarrow} - n_{21}^{\uparrow\uparrow} + n_{21}^{\downarrow\downarrow}), \quad (16)$$

where $n_{12}^{\uparrow\uparrow} \equiv \sum_i \langle c_{i1\uparrow}^\dagger c_{i2\uparrow} \rangle$ are the single-particle density matrices off-diagonal in the orbital index. At zero order in η , the mean field Hamiltonian for the chiral pairing states are symmetric with respect to spin $\uparrow \leftrightarrow \downarrow$. Consequently, the linear in η term in $\delta\mathcal{F}$ vanishes and $\delta\mathcal{F} \sim \mathcal{O}(\eta^2)$. On the other hand, for the four helical pairing states, $\delta\mathcal{F} \sim \mathcal{O}(\eta)$ in general, if

the superconducting order parameters on the α and β bands are not identically zero when $\eta = 0$. This linear dependence has been emphasized in Ref. [25].

We calculate the η dependence of $\delta\mathcal{F}$ for our model in weak-coupling RG. In the case of $J = 0$, we actually find that $\delta\mathcal{F} \propto (\eta/t)^2$ rather than $\propto \eta/t$. This comes from a complete decoupling between the $\alpha + \beta$ and γ bands when $J = J' = \eta = 0$, which makes all the density matrices in Eq. (16) identically zero and invalidates the above argument for the linear in η dependence (for details see Appendix B). When $J \neq 0$, the three bands are coupled and, indeed, we find the leading η/t dependence of $\delta\mathcal{F}$ linear, as shown in Fig. 5.

To summarize, the presence of $g(\mathbf{k})$ and η induces a pseudospin SU(2) symmetry breaking term in the GL free energy, given in Eq. (15), which lifts the degeneracy among different p -wave states. This term always favors helical states over the chiral states. It is invariant under the pseudospin rotations along z that preserves the degeneracy between A_{1u} and A_{2u} , and that between B_{1u} and B_{2u} . The splitting between the two helical state groups is $\delta T_c \propto t''' \eta/t$, to leading order in t'''/t and η/t . In the special case of $J = J' = 0$, the splitting is $\propto t''' \eta^2/t^2$. Interestingly, the necessary ingredients, t''' and η , for the splitting identified here are the same as those responsible for a spin Hall effect discussed in Ref. [37], suggesting that the two may be intimately connected.

D. SOC induced terms due to finite $J = J'$ but with $g(\mathbf{k}) = 0$

In this section, we analyze the pseudospin rotational breaking terms due to finite J and η , while keeping $g(\mathbf{k}) = 0$.

1. Pseudospin SU(2) breaking terms

When $J \neq 0$, applying the \mathcal{U} transformation in Eq. (11) to \tilde{V} in Eq. (9) changes the form of \tilde{V} and leads to

$$\tilde{V} \equiv \mathcal{U}^\dagger \tilde{V} \mathcal{U} = \tilde{V}_{\text{inv}} + \tilde{V}_J + \tilde{V}_{J'}, \quad (17)$$

where $\tilde{V}_{\text{inv}} = \mathcal{U}^\dagger (\tilde{V}_U + \tilde{V}_{U'}) \mathcal{U} = \tilde{V}_U + \tilde{V}_{U'}$ is still pseudospin SU(2) invariant. The other two terms are

$$\begin{aligned} \tilde{V}_J = \mathcal{U}^\dagger \tilde{V}_J \mathcal{U} = & -J \sum_i \{ [S_{i2}^x S_{i3}^x + S_{i1}^y S_{i3}^y + S_{i1}^z S_{i2}^z] \\ & - [S_{i1}^x S_{i2}^x + S_{i1}^x S_{i3}^x + S_{i1}^y S_{i2}^y + S_{i2}^y S_{i3}^y + S_{i1}^z S_{i3}^z + S_{i2}^z S_{i3}^z] \}, \end{aligned} \quad (18a)$$

$$\begin{aligned} \tilde{V}_{J'} = \mathcal{U}^\dagger \tilde{V}_{J'} \mathcal{U} = & \frac{J'}{2} \sum_{i, \sigma \neq \sigma'} \left\{ - \sum_{\alpha \neq b = \{1,2\}} - \sum_{\alpha \neq b = \{2,3\}} + \sum_{\alpha \neq b = \{1,3\}} \right\} \\ & \times a_{i\alpha\sigma}^\dagger a_{i\alpha\sigma}^\dagger a_{i\beta\sigma'} a_{i\beta\sigma'}. \end{aligned} \quad (18b)$$

The \mathcal{U} transformation shifts the SOC induced effect of spin rotational symmetry breaking from the kinetic energy part of the Hamiltonian to the interaction part. Note that the kinetic energy part becomes pseudospin SU(2) invariant after the transformation. Since each term of the original interaction V in Eq. (7) is SU(2) spin rotational invariant, we can identify the pseudospin SU(2) rotational symmetry breaking terms in

\tilde{V} as

$$\begin{aligned} \delta \tilde{V} = & -2J \sum_i [S_{i2}^x S_{i3}^x + S_{i1}^y S_{i3}^y + S_{i1}^z S_{i2}^z] \\ & + J' \sum_{i, \sigma \neq \sigma'} \sum_{\alpha \neq b = \{1,3\}} a_{i\alpha\sigma}^\dagger a_{i\alpha\sigma}^\dagger a_{i\beta\sigma'} a_{i\beta\sigma'}. \end{aligned} \quad (19)$$

In this equation the J' term alone does not lift the degeneracy among different p -wave pairing states. This can be proved within weak-coupling RG and RPA approximations by examining diagrammatic contributions to helical and chiral states at each order in interaction. There is a one-to-one correspondence between the two contributions that contain J' , if $J = 0$. This result is consistent with Ref. [24], where a direct perturbation, up to second order in both interaction and SOC, shows that the SOC induced terms to the effective interaction in the Cooper pairing channel necessarily depend on J when $g(\mathbf{k}) = 0$. We have also verified the above conclusion in our numerical weak-coupling RG and RPA calculations. Therefore, within linear order in $J (= J')$, we can drop the J' term in Eq. (19).

2. GL free energy terms due to $\delta \tilde{V}$

$\delta \tilde{V}$ in Eq. (19) does not completely break the pseudospin SU(2) rotational symmetry. Mirror reflections about the xz and yz planes, denoted as \mathcal{M}_{xz}^δ and \mathcal{M}_{yz}^δ respectively, leave $\delta \tilde{V}$ invariant. This holds even if the J' term in Eq. (19) is taken into account. \mathcal{M}_{xz}^δ and \mathcal{M}_{yz}^δ are therefore symmetries of the whole microscopic Hamiltonian. In Table 1, the only terms compatible with these symmetries are $f_2^{\text{SOC},1}$, $f_2^{\text{SOC},4}$, and $f_2^{\text{SOC},5}$. Therefore, in general, the GL free energy due to $\delta \tilde{V}$ is given by

$$\begin{aligned} \delta \mathcal{F} = & a_1 f_2^{\text{SOC},1} + a_4 f_2^{\text{SOC},4} + a_5 f_2^{\text{SOC},5} \\ = & \frac{2a_1 + a_4 + a_5}{4} [f_2^{\text{SOC},1} + f_2^{\text{SOC},4} + f_2^{\text{SOC},5}] \\ & + \frac{2a_1 - a_4 - a_5}{4} (f_2^{\text{SOC},1} - f_2^{\text{SOC},4} - f_2^{\text{SOC},5}) \\ & + \frac{a_4 - a_5}{2} (f_2^{\text{SOC},4} - f_2^{\text{SOC},5}), \end{aligned} \quad (20)$$

where $\{a_1, a_4, a_5\}$ are three coefficients that shift the T_c away from T_c^0 . In $\delta \mathcal{F}$, $(f_2^{\text{SOC},1} + f_2^{\text{SOC},4} + f_2^{\text{SOC},5})$ is trivial and shifts the T_c of all p -wave pairing states equally. To leading order in J/U , $\{a_1, a_4, a_5\} \propto J^1 (f_2^{\text{SOC},1} - f_2^{\text{SOC},4} -$

¹The leading order contribution to $\delta \mathcal{F}$ in a weak-coupling theory comes from a second order perturbation result, $\delta \mathcal{F} = \langle \tilde{V}_{\text{inv}} \tilde{G}_4 \delta \tilde{V} \rangle$, which is second order in \tilde{V} but first order in J/U . Here, $\langle \dots \rangle$ means being averaged in a mean-field p -wave pairing state obtained at $J = 0$, and \tilde{G}_4 is the four-point Green's function defined for the normal state Hamiltonian after the \mathcal{U} transformation, \tilde{H}_K given in Eq. (12). Note that the first order perturbation contribution, $\langle \delta \tilde{V} \rangle$, is identically zero for a p -wave pairing state because the interaction $\delta \tilde{V}$ is purely on-site. However, because the pseudospin rotational symmetry property of $\delta \mathcal{F}$ is completely dictated by $\delta \tilde{V}$, in the main

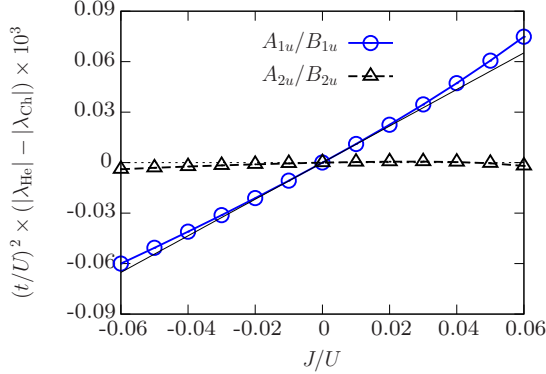


FIG. 2. J/U dependence of the splitting between helical and chiral p -wave pairing states in weak-coupling RG. $t''' = 0$ and $\eta = 0.1t$. The splitting is linear in J/U at small J/U . Note that the two helical states, $\{A_{2u}, B_{2u}\}$, are almost degenerate with the chiral state, which is accidental and not robust to band parameter changes.

$f_2^{\text{SOC},5}$ splits the chiral state away from helical ones, while $(f_2^{\text{SOC},4} - f_2^{\text{SOC},5})$ breaks the degeneracy among the four helical p -wave states, splitting them into two groups, $\{A_{1u}, B_{1u}\}$ and $\{A_{2u}, B_{2u}\}$. Within each group the two states are connected by \mathcal{M}_{xz}^S and \mathcal{M}_{yz}^S , and therefore remain degenerate. In terms of the components of the order parameter matrix $\hat{\Delta}$, $f_2^{\text{SOC},4} - f_2^{\text{SOC},5} = (-1/2)[\Delta_{\uparrow,x}^* \Delta_{\downarrow,x} - \Delta_{\uparrow,y}^* \Delta_{\downarrow,y}] + \text{c.c.}$. This term was identified in Refs. [24,28] using a direct expansion in the SOC, while our analyses here are based on symmetries of the model.

Again, it is important to understand the SOC dependence of $\delta\mathcal{F}$ in Eq. (20). For that we go back to the original Hamiltonian written in terms of the actual spin. As mentioned previously, the linear order in η/t contribution to the GL free energy comes from $\delta\mathcal{F} = 2\eta(\mathbf{L} \cdot \mathbf{S})$, where \mathbf{S} is the actual spin operator, not pseudospin. However, $\langle \mathbf{L} \cdot \mathbf{S} \rangle \equiv 0$ because of the three remaining mirror reflection symmetries in the pseudospin space, $\{\mathcal{M}_{xz}^S, \mathcal{M}_{yz}^S, \mathcal{M}_{xy}^S\}$, which imply the same symmetries for the actual spin, since the $\{x, y, z\}$ directions are identical in the pseudospin and actual spin spaces. On the other hand, these symmetries do not prohibit a second order in η/t term, $\delta\mathcal{F} \propto \langle (2\eta \mathbf{L} \cdot \mathbf{S})^2 \dots \rangle$, where \dots here stands for η independent operators that have a dimension of energy inverse. Therefore, in Eq. (20), the GL expansion coefficients $\{a_1, a_4, a_5\} \propto (\eta/t)^2$ to leading order in η/t .

3. Numerical results

We confirm the above conclusions with weak-coupling RG calculations, where the details of the calculation follow Refs. [18,26]. Figure 2 shows the numerical results of the splitting between helical and chiral states as a function of J/U for fixed $\eta/t = 0.1$. At $J/U = 0$, all p -wave pairing states are

text we simply focused on $\delta\tilde{V}$, rather than the more complicated $\tilde{V}_{\text{inv}}, \tilde{G}_4, \tilde{\delta V}$

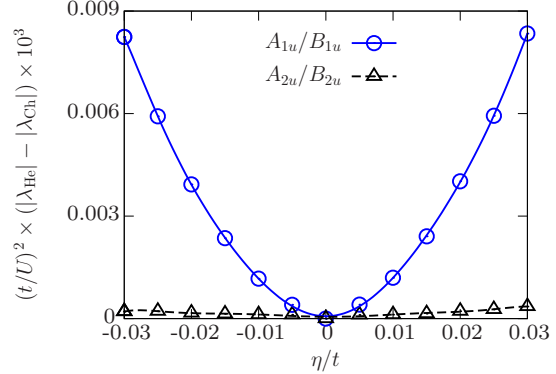


FIG. 3. η/t dependence of the splitting between helical and chiral states in weak-coupling RG. $t''' = 0$ and $J/U = 0.06$. The splitting is $\propto (\eta/t)^2$ to leading order in η/t . Again, due to the near-degeneracy between the $\{A_{2u}, B_{2u}\}$ and chiral states for these band parameters, the quadratic dependence of the splitting in η/t is difficult to discern.

degenerate, even though $\eta \neq 0$, consistent with the conclusion obtained in Sec. III B. At finite J/U , the degeneracy between chiral and helical states is lifted. The four helical states are split into two groups of two degenerate states. The splitting of T_c between the chiral states and the $\{A_{1u}, B_{1u}\}$ group is indeed $\propto J/U$ to leading order, as predicted. Interestingly, the other group, $\{A_{2u}, B_{2u}\}$, remains almost degenerate with the chiral states even at finite J/U , which is, however, not robust to changes of normal state band dispersions.

Figure 3 shows our weak-coupling RG results for the SOC dependence of $|\lambda_{\text{He}}| - |\lambda_{\text{Ch}}|$. Within numerical errors, $|\lambda_{\text{He}}| - |\lambda_{\text{Ch}}| \propto (\eta/t)^2$, in agreement with the above analytical analysis.

A summary of the main results obtained in this section is: finite $J = J'$ and η induce pseudospin rotational breaking terms in the GL free energy as given in Eq. (20), which lift the degeneracy among different p -wave pairing states. The splitting of T_c between different p -wave states is $\delta T_c \propto (J/U)\eta^2/t$, to leading order in J/U and η/t . The degeneracy between A_{1u} and B_{1u} , and that between A_{2u} and B_{2u} , remains due to pseudospin mirror reflection symmetries in the xz and yz planes. The terms in Eq. (20) can favor either chiral or helical states, depending on the magnitudes of the two coefficients, $(2a_1 - a_4 - a_5)/4$ and $(a_4 - a_5)/2$, which in turn depend on the normal state band structures. If $a_1 < \min\{a_4, a_5\}$, then $(2a_1 - a_4 - a_5)/4 < -(a_4 - a_5)/4$ and the chiral states are stabilized.

E. Results for both $g(\mathbf{k}) \neq 0$ and $J \neq 0$

When both $g(\mathbf{k})$ and $J = J'$ are nonzero, the SOC induced GL free energy is given by the sum of Eqs. (15) and (20). However, the GL free energy expansion coefficients for each $f_2^{\text{SOC},j}$ are different from those in Eqs. (15) and (20) because of additional contributions that depend on both t''' and J . The degeneracy among all p -wave pairing states is lifted except the one between the two chiral states with opposite chirality

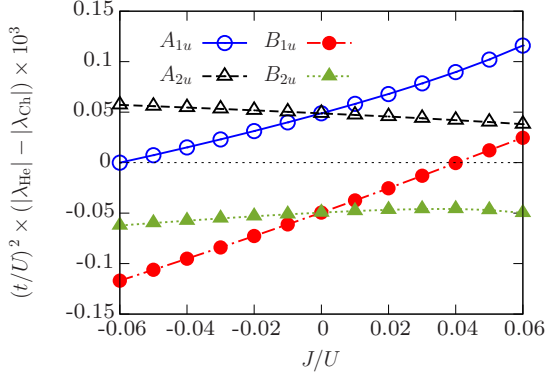


FIG. 4. J/U dependence of the splitting between different helical and chiral p -wave states. $t''' = 0.01t$ and $\eta = 0.1t$. The splitting at small J/U is dominated by the linear in t''' effect discussed in Sec. III C, which always stabilizes helical states.

within the E_u representation, as seen in Fig. 4. Because of the near-degeneracy seen in Fig. 2, the splitting between A_{2u} (or B_{2u}) and chiral states is dominated by the t''' term at small J/U . An implication is that, with both J and t''' present, the dominant p -wave pairing state in the small J/U and t'''/t parameter space regime will be always helical, rather than chiral, regardless of whether the splitting, $|\lambda_{\text{He}}| - |\lambda_{\text{Ch}}|$, for the other two helical states, $\{A_{1u}, B_{1u}\}$, is $\propto AJ/U$ with a positive slope $A > 0$, as seen in Fig. 4, or with $A < 0$. When t'''/t becomes larger, the splitting between $\{A_{2u}, B_{2u}\}$ and chiral states can pick up a significant J/U linear dependence because of cross dependent terms.

Some of the conclusions derived in Secs. III C and III D still hold when both t''' and J are present. For example, the leading SOC dependence of the splitting between different p -wave pairing states is linear due to the $g(\mathbf{k})$ induced terms, as shown in Fig. 5. These terms are $\propto t''' \eta/t^2$ to leading order in t'''/t .

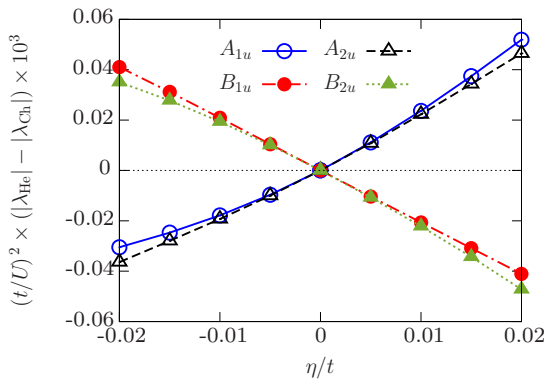


FIG. 5. η/t dependence of the splitting between helical and chiral p -wave states in weak-coupling RG. $t''' = 0.1t$ and $J/U = 0.11$. The leading SOC dependence is linear at small η/t .

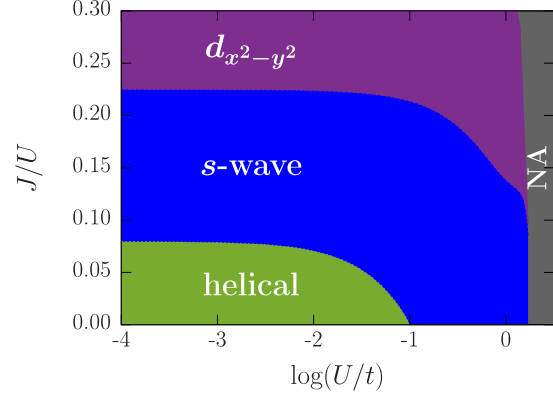


FIG. 6. Phase diagram obtained within RPA for different J/U and U/t . The RPA breaks down in the “NA” regime. The three intraorbital hoppings in Eq. (6) are $\epsilon_{xz(yz)}(\mathbf{k}) = -2t \cos k_x(y)$ $- 2t^\pm \cos k_y(x) - \mu$, $\epsilon_{xy}(\mathbf{k}) = -2t'(\cos k_x + \cos k_y) - 4t'' \cos k_x \cos k_y - 2t'''(\cos 2k_x + \cos 2k_y) - \mu$. We choose the band parameters, $(t, t^\pm, t', t'', t''', \mu, \eta) = (1, 0.1, 0.8, 0.3, 0.05, -0.015, 1.075, 0.2)$, such that the resulting Fermi surfaces fit recent ARPES data [17].

IV. STABILITY OF CHIRAL p -WAVE PAIRING

The analysis of Sec. III shows that, within the current 2D three-band model with an on-site Kanamori-Hubbard interaction, the dominant pairing is always helical, rather than chiral, at small J/U and U/t where p -wave pairing is favored within the weak-coupling approximation [18,29,31]. On the other hand, at large J/U , pseudospin singlet pairing takes over [18,29,31]. Therefore we expect the phase diagram, in the parameter space spanned by J/U and U/t , to be dominated by helical p -wave and singlet pairing states for physical band parameters describing Sr_2RuO_4 , where interorbital hybridization between d_{xz} and d_{yz} orbitals can not be neglected. This expectation is confirmed by our RPA calculations, which give the phase diagram shown in Fig. 6. Details of the RPA calculation follow those found in Refs. [29,30]. The RPA breaks down for $U/t \gtrsim \mathcal{O}(1)$ due to an instability inherent in this approximation,² but can give reliable results even beyond the weak-coupling regime, $U/t \ll 1$ [38]. In Fig. 6, there is no trace of chiral pairing even at an intermediate value of J/U . In this phase diagram, the helical state order parameter realized is $\mathbf{d}(\mathbf{k}) = \hat{x}k_x + \hat{y}k_y$ (A_{1u}), and the s and $d_{x^2-y^2}$ wave order parameters belong to the irreducible representation A_{1g} and B_{1g} , respectively, of the D_{4h} group. However, they are not simple lowest harmonic functions, but are highly anisotropic, similar to those found in Refs. [18,29]. In each phase of the phase diagram, the ratio of the gap magnitude on different bands depends on both J/U and U/t . However, unlike

²The eigenvalue of the effective interaction in the Cooper pairing channel, λ , diverges where RPA breaks down and for Fig. 6, we cut off the phase diagram at $(t/U)^2 |\lambda| = 0.2$. The boundary is insensitive to the choice of a cutoff [provided it is $\gtrsim \mathcal{O}(1)$], since λ diverges rapidly in this region

Ref. [18] where the $\alpha + \beta$ always dominate when the favored pairing symmetry is helical, we find that the dominant band in the helical phase is γ when both J/U and U/t are small, while it changes to $\alpha + \beta$ at larger J/U or U/t .

Since chiral p -wave pairing states have been previously found in various numerical calculations using the same model [18,24,29,30], we comment on these. In Ref. [24], the dominant pairing instability was calculated by solving Eliashberg equations with an effective pairing interaction derived from a perturbation theory up to second order in the bare interaction. Chiral p -wave was found to be the dominant channel when the Eliashberg equations were solved only for the γ band, while the coupling between γ and $\alpha + \beta$ bands due to the effective interaction was neglected. However, this coupling can have significant effects on the ratio between the gap magnitudes of the two sets of bands [18,29], which in turn can impact the relative stability between helical and chiral p -wave pairing states. This can explain the difference between our numerical results and those in Ref. [24]. Ref. [18] is a weak-coupling RG calculation, where chiral p -wave states have been found near $J/U = 0$ with a nonzero $t'''/t = 0.01$. However, this is inconsistent with our analytical analyses of the t''' effect in Sec. III C and also inconsistent with our numerical results in Fig. 6. Reference [29] is an RPA calculation based on the same model. The phase diagrams obtained in the weak-coupling limit are similar to those in Ref. [18]. In particular, there is a significant portion of the phase diagram at small J/U and U/t , where chiral p -wave pairing dominates. However, we note that Eq. (S13) of Ref. [29] takes the real part of the effective interaction. In the presence of SOC, this suppresses the t''' induced terms that we have identified in Eq. (15), which favors helical over chiral states. This may explain the discrepancy between our RPA phase diagram in Fig. 6 and those in Ref. [29]. In Ref. [30], a similar RPA calculation was performed at relatively large U for different Fermi surface geometries. Chiral p -wave pairing has been found only at large SOC for the Fermi surface geometry where the γ band touches the zone boundary. However, in that calculation, the interorbital hybridization t''' was set to zero, which completely leaves out the terms in Eq. (15). Physically we do not expect this hybridization to be vanishingly small, given that it is between orbitals on two next-nearest neighboring sites. Including a small $t''' = 0.01t$ suppresses the chiral p -wave pairing, giving way to helical states. We have verified this with RPA calculations in a parameter regime that overlaps with those of Ref. [30] and found results that are consistent with our analytical analysis. Furthermore, we find the stability of chiral p -wave in this parameter regime requires fine-tuning, in that a small change in parameters renders this phase unstable.

Given the difficulty of stabilizing a chiral p -wave state within the current model, we wonder what ingredients can favor a chiral p -wave state if we go beyond this model. There are at least two possibilities to consider: (1) three-dimensional effects on the normal state Fermi surface; (2) longer range off-site interactions.

In a 3D model with the same on-site Kanamori-Hubbard interaction, like the one used in Ref. [31], two additional interorbital hybridization terms appear in the normal state Hamiltonian, $t_{xz,xy}$ ($t_{yz,xy}$) between d_{xz} (d_{yz}) and d_{xy} orbitals,

in addition to the t''' that we have already considered. The two interlayer hybridizations $t_{xz,xy}$ and $t_{yz,xy}$, combined with the finite SOC, can mix an out-of-plane component $k_z(\hat{x}, \hat{y})$ in the $\mathbf{d}(\mathbf{k})$ vector of the chiral p -wave pairing state within the E_u representation [14,39,40], which shifts the T_c of the chiral p -wave state. However, this mixing is small because of its dependence on small parameters η/t and t_z/t , where $t_z \equiv \max\{|t_{yz,xy}|, |t_{xz,xy}|\}$. The mixing vanishes if either $\eta = 0$ or $t_z = 0$ so that, to leading order in η/t and t_z/t , it is $\propto \eta t_z/t^2$. The resulted critical temperature shift from the mixing can be estimated by a second order nondegenerate perturbation theory and the result is $\delta T_c/T_c \propto (\eta t_z/t^2)^2$. Detailed discussions can be found in Appendix C. This shift is negligible compared to the effects of other SOC induced terms on T_c that we discussed in Sec. III. Therefore we ignore the possible mixing in the following.

Then we can easily generalize our 2D analyses to the 3D model. If we set all interorbital hybridizations and J to zero, the same derivations as in Sec. III B lead to the same conclusion that all p -wave pairing states remain degenerate even with $\eta \neq 0$. Note that in this case there is no mixing between the in-plane and out-of-plane pairings because the full pseudospin $SU(2)$ symmetry is still preserved. SOC induced terms by each interorbital hybridization can be analyzed similarly following Sec. III C. The two additional hybridizations, $t_{xz,xy}$ and $t_{yz,xy}$, add two additional terms to the $\delta \tilde{H}_K(\mathbf{k})$ in Eq. (14) that are $\propto t_{xz,xy} \sin k_z/2 \cos k_x/2 \sin k_y/2 \dots$ and $\propto t_{yz,xy} \sin k_z/2 \cos k_y/2 \sin k_x/2 \dots$, respectively [31]. However, the leading order GL free energy from these two terms vanish in $\delta \mathcal{F} = \langle \delta \tilde{H}_K(\mathbf{k}) \rangle$ after the \mathbf{k} average, since we have ignored a possible mixing of the out-of-plane p_z pairing component, and the odd k_z dependence of those two terms can not be compensated by any other term in the mean field Hamiltonian of a p_x or p_y pairing state. Therefore, to linear order in $t_{xz,xy}/t$ or $t_{yz,xy}/t$, which are expected to be even smaller than t'''/t , we can drop those additional hybridizations in the normal state Hamiltonian. Then the analyses of the t''' and J induced terms are identical to those in Sec. III C and III D. Therefore the conclusions obtained in the 2D analysis can be directly applied to the 3D model. In other words, the three-dimensional effect of the FS does not help stabilize a chiral p -wave pairing state, consistent with the 3D weak-coupling RG numerical results obtained in Ref. [31], where helical states have been found to dominate over chiral p -wave pairing at J/U all the way up to $J/U = 0.2$.

Another possibility is to consider longer-range off-site interaction models [23,41]. Reference [23] considered such a model with attractive nearest neighbor interactions, and, indeed, chiral p -wave pairing states were found to be stabilized in some regime of the pairing interaction parameter space. However, the solutions were obtained under the assumption that the p -wave pseudospin triplet channel is favored over singlet channels. In Ref. [41], the authors studied a nearest neighbor version of the Kanamori-Hubbard interaction model, and found that p -wave pseudospin triplet states are more stable than singlet channels for certain choice of interaction parameters; on the other hand, the relative stability among different p -wave pairing states has been completely ignored by simply assuming that chiral p -wave pairing states are favored over helical states. In both cases, further investigations beyond

the assumptions made here would be needed to establish the stability of chiral p -wave states.

V. CONCLUSIONS

We have conducted a thorough study of the effect of SOC on the relative stability of different p -wave pairing states for a widely used microscopic model for Sr_2RuO_4 . Our analysis combines a general GL free energy expansion with an analytical study of the symmetry of the microscopic model Hamiltonian. We give the most general form of the SOC induced quadratic GL terms that break the pseudospin $\text{SU}(2)$ rotation symmetry, identify the relevant GL terms for the microscopic model, and examine their effects on lifting the degeneracy among different p -wave pairing states. The analytical results are further supported by our weak-coupling RG and RPA numerical calculations.

A theme that emerges from this study is that the breaking of $\text{SU}(2)$ rotation symmetry in pseudospin space can be quite different from that in the actual spin space; this was also pointed out in Ref. [24]. The former depends on not only the presence of SOC but also other ingredients of the microscopic Hamiltonian, which in the current model are the interorbital hybridization t'' , Hund's coupling J , and/or pair hopping. The additional dependence on t'' and J significantly reduces the splitting among different p -wave states for Sr_2RuO_4 since both t''/t and J/U are small. In the parameter space regime relevant to Sr_2RuO_4 , with finite but small t''/t and small J/U , we find that the finite t'' effect tends to dominate and always stabilizes helical states over the chiral ones. We have also generalized our analysis to a 3D model and shown that the existence of interorbital hybridizations, in addition to the t'' that already exists in 2D models, does not help stabilize the chiral p -wave pairing states, in agreement with the recent numerical study [31]. On the other hand, including longer-range interactions may or may not make the chiral states more favorable and requires further investigation.

Our analysis has resolved some conflicts among different results on the relative stability between helical and chiral p -wave pairing states in the literature. Since the analysis is largely based on the symmetries of the model and independent of how the model is treated, it also serves as a guide for future studies, both analytical and numerical. Furthermore, the analysis presented here can be adapted to study the effect of SOC on other multiorbital pseudospin triplet superconductors.

An outstanding issue in Sr_2RuO_4 is to reconcile theory with the observations of broken time-reversal symmetry [1,3] and a jump in the shear modulus c_{66} [42]. Although a chiral p -wave state can explain both, here we discuss possible alternative explanations with helical states.

Given the small splitting among different helical states found here and in previous works [18,29,31,43], a possibility to consider is a pair of accidentally or nearly degenerate helical states. If the two states are close enough to degeneracy, such a pair can lead to either coexistence of different helical state domains [14,44] or a homogeneous time reversal breaking state [44–46], depending on microscopic interactions. A previous analysis of quartic GL terms [47] suggests that a homogeneous time reversal symmetry breaking state is almost impossible unless the system is very near or right at the degeneracy point.

Moreover, except right at the degeneracy point, this scenario requires two phase transitions with different T_c , which is not observed experimentally. Nevertheless, if two almost degenerate helical orders do form a homogeneous state, this can lead to a jump in c_{66} if the two mixed representations are $\{A_{1u}, B_{2u}\}$ or $\{A_{2u}, B_{1u}\}$ [43]. However, within the models studied in this paper, our analysis in Sec. III suggests that residual symmetries in pseudospin space do not naturally lead to a degeneracy between A_{1u} (A_{2u}) and B_{2u} (B_{1u}).

In the case of coexistence of domains, time reversal breaking is possible at domain walls where two different helical order parameters coexist. However, since the order parameter mixing is local, the resulted coupling to external probes, such as light in a Polar Kerr measurement [3] and the shear strain ϵ_{xy} in an ultrasound measurement [42], is also local, which makes it unlikely to be able to account for the experiments. So a theoretical explanation of both broken time-reversal symmetry and a jump in c_{66} is highly constrained. Further investigations, both experimentally and theoretically, are needed to better assess the possibility of reconciling the experiments with helical ordered states.

Note added. Recently, Ref. [30] was updated with additional calculations on the effects of the interorbital hybridization t'' . Their new results are consistent with our analysis.

ACKNOWLEDGMENTS

We would like to thank Sung-Sik Lee, Wen Huang, and Thomas Scaffidi for useful discussions. This research is supported by the National Science and Engineering Research Council of Canada (NSERC) and the Canadian Institute for Advanced Research (CIFAR). This work was made possible by the facilities of the Shared Hierarchical Academic Research Computing Network (SHARCNET: www.sharcnet.ca) and Compute/Calcul Canada.

APPENDIX A: SOC INDUCED GL FREE ENERGY TERMS AT QUADRATIC ORDER FOR 2D MODELS

As mentioned in the main text, the remaining symmetry group in the presence of SOC is $D_{4h}^{L+S} \otimes U(1)^C$ for a 2D model. To derive all possible GL free energy terms at quadratic order for the pseudospin triplet pairing states, we contract the rank-4 tensor, $(d_i^\mu)^* d_j^\nu$, to a scalar such that it is invariant under all symmetry operations of the above group. For 2D models, the xy -plane mirror reflection symmetry of D_{4h}^{L+S} , denoted as \mathcal{M}_{xy}^S , is operative only on the pseudospin since there is no k_z . \mathcal{M}_{xy}^S requires that, in $(d_i^\mu)^* d_j^\nu$, either $\{\mu, \nu\} = \{x, y\}$ or $\mu = \nu = z$.

For the case of $\{\mu, \nu\} = \{x, y\}$, there are only four possible independent contractions, given in Table III. With $\mu = \nu = z$ the only possible contraction is

$$\sum_{ij=\{x,y\}} \delta_{ij} (d_i^z)^* d_j^z = |d_x^z|^2 + |d_y^z|^2. \quad (\text{A1})$$

Linear combinations of the four terms from Table III and the one in Eq. (A1) gives the five terms in Table I of the main text. The above SOC induced free energy terms can be also rewritten in terms of the order parameter matrix $\hat{\Delta}$. Rewriting

TABLE III. All possible contractions of $(d_i^\mu)^* d_j^\nu$ that are invariant under the $D_{4h}^{L+S} \otimes U(1)^C$ group for $\{\mu, \nu\} = \{x, y\}$. For 2D models, $\{i, j\} = \{x, y\}$.

Different contractions	Results
$\sum_{\mu\nu ij=\{x,y\}} \delta_{\mu i} \delta_{\nu j} (d_i^\mu)^* d_j^\nu$	$\sum_{ij=\{x,y\}} (d_i^i)^* d_j^j$
$\sum_{\mu\nu ij=\{x,y\}} \delta_{\mu j} \delta_{\nu i} (d_i^\mu)^* d_j^\nu$	$\sum_{ij=\{x,y\}} (d_i^j)^* d_j^i$
$\sum_{\mu\nu ij=\{x,y\}} \delta_{\mu\nu} \delta_{ij} (d_i^\mu)^* d_j^\nu$	$\sum_{ij=\{x,y\}} (d_i^j)^* d_j^i$
$\sum_{\mu\nu ij=\{x,y\}} \delta_{\mu i} \delta_{i j} \delta_{j \nu} (d_i^\mu)^* d_j^\nu$	$ d_x^x ^2 + d_y^y ^2$

the five terms in Table I using Eq. (1) and linearly recombining them gives the five independent terms in Table IV, from which we see that order parameter products other than $\hat{\Delta}^\dagger \hat{\Delta}$, such as $\hat{\Delta}_i \hat{\Delta}$ and $\hat{\Delta}_i \hat{\Delta}_j$, also appear in the free energy expansion, due to the broken pseudospin SU(2) symmetry [34].

APPENDIX B: SOC DEPENDENCE OF THE SPLITTING BETWEEN HELICAL AND CHIRAL STATES WHEN $J = J' = 0$

The η dependence of $\delta\mathcal{F}$ for the 2D model at $J = J' = 0$ is calculated in weak-coupling RG and shown in Fig. 7. As mentioned in the main text, we find that the splitting between helical states has a quadratic dependence on η for small η at $J/U = 0$. This result can be understood as follows. When both $\eta = 0$ and $J' = J = 0$, the two-particle effective interaction has no coupling between $\alpha + \beta$ bands, which consist of the d_{xz} and d_{yz} orbitals, and the γ band, if only intraband pairing is considered as in the weak-coupling RG [18]. Then the pairing lives purely on the γ band since that band has a larger density of states. Therefore, at zero order in η , all the off-diagonal density matrices in Eq. (17) are identically zero. As a consequence, $\delta\mathcal{F} \sim \mathcal{O}(\eta^2)$. However, in general, we expect the three bands to be coupled even when $\eta = 0$ if the pair hopping $J' \neq 0$. In that case, $\delta\mathcal{F}$ picks up a linear in η term, as seen in Fig. 5. The η linear term is likely to dominate over the η^2 term since its estimated J/U for Sr₂RuO₄ is about 0.1 (see Ref. [18] and the references therein). Note that even a small J/U can strongly couple the three bands together such that order parameter magnitudes on the three bands are comparable [18]. This is largely because the normal state

TABLE IV. All possible SOC induced GL free energy terms at quadratic order in $\hat{\Delta}$ for the pseudospin triplet pairing states in a 2D model. $\hat{\Delta}_x$ is the part of the order parameter matrix $\hat{\Delta}$ that transforms like k_x under the spatial D_{4h} group. The trace Tr is performed in the pseudospin space. Note that, in this table, $f_2^{\text{SOC},E}$ is allowed because the pseudospin Pauli matrix σ_z is even under the xy -plane mirror reflection \mathcal{M}_{xy}^S .

GL terms	Expressions in terms of $\hat{\Delta}$
$f_2^{\text{SOC},A}$	$\text{Tr}[\hat{\Delta}_x^\dagger \sigma_z \hat{\Delta}_x \sigma_z] + \text{Tr}[\hat{\Delta}_y^\dagger \sigma_z \hat{\Delta}_y \sigma_z]$
$f_2^{\text{SOC},B}$	$\text{Tr}[\hat{\Delta}_x^\dagger \sigma_x \hat{\Delta}_y \sigma_x] - \text{Tr}[\hat{\Delta}_x^\dagger \sigma_y \hat{\Delta}_x \sigma_y]$
$f_2^{\text{SOC},C}$	$\text{Tr}[\hat{\Delta}_x^\dagger \sigma_x \hat{\Delta}_x \sigma_x] - \text{Tr}[\hat{\Delta}_y^\dagger \sigma_y \hat{\Delta}_y \sigma_y]$
$f_2^{\text{SOC},D}$	$\text{Tr}[\hat{\Delta}_x^\dagger \sigma_x \hat{\Delta}_y \sigma_y] - \text{Tr}[\hat{\Delta}_y^\dagger \sigma_y \hat{\Delta}_x \sigma_x]$
$f_2^{\text{SOC},E}$	$i \{ \text{Tr}[\hat{\Delta}_x^\dagger \sigma_z \hat{\Delta}_y] - \text{Tr}[\hat{\Delta}_y^\dagger \sigma_z \hat{\Delta}_x] \}$

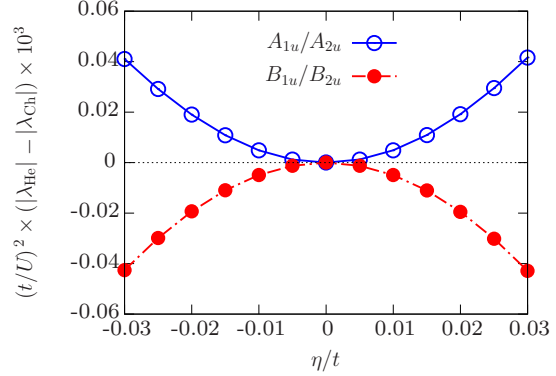


FIG. 7. η/t dependence of the splitting between helical and chiral p -wave pairing states in weak-coupling RG. $t'' = 0.1t$ and $J = 0$. The splittings are $\propto (\eta/t)^2$ to leading order in η .

density of states of the $\alpha + \beta$ bands is comparable to that of the γ band.

APPENDIX C: SOC INDUCED GL FREE ENERGY TERMS AT QUADRATIC ORDER FOR 3D MODELS

For a 3D model that depends on k_z , in addition to the basis functions given in Table II, an out-of-plane pairing component, with the basis function $\mathbf{d}(\mathbf{k}) = \hat{z}k_z$ for the A_{1u} and $\mathbf{d}(\mathbf{k}) = k_z(\hat{x}, \hat{y})$ for the E_u representation, is also allowed by symmetry [14,39,40]. In the presence of SOC and interlayer coupling, in general, the vector $\mathbf{d}(\mathbf{k})$ of the E_u (but not the A_{1u} ; see below) representation is a mixture of the in-plane and out-of-plane pairing components, which leads to more GL free energy terms at quadratic order in $\hat{\Delta}$.

To obtain these GL free energy terms, we follow the 2D derivations outlined in Appendix A. The only difference is that, for 3D models, the xy -plane mirror reflection, \mathcal{M}_{xy}^{L+S} , now operates on both the \mathbf{k} and pseudospin. Besides the terms in Table I, we also get

$$f_2^{\text{SOC},6} = |d_z^z|^2, \quad (\text{C1a})$$

$$f_2^{\text{SOC},7} = |d_z^x|^2 + |d_z^y|^2, \quad (\text{C1b})$$

$$f_2^{\text{SOC},8} = \sum_{j=\{x,y\}} [(d_j^j)^* d_j^j + \text{c.c.}], \quad (\text{C1c})$$

$$f_2^{\text{SOC},9} = \sum_{j=\{x,y\}} i [(d_j^j)^* d_j^j - \text{c.c.}]. \quad (\text{C1d})$$

$f_2^{\text{SOC},6}$ and $f_2^{\text{SOC},7}$ describe the free energy contributions from the $\mathbf{d}(\mathbf{k}) = \hat{z}k_z$ and $\mathbf{d}(\mathbf{k}) = k_z(\hat{x}, \hat{y})$ pairings, respectively. They exist even without SOC. However, $f_2^{\text{SOC},6}$ and $f_2^{\text{SOC},7}$ are irrelevant to our current discussions since the T_c of the out-of-plane pairings are expected to be much smaller than that of the in-plane components for Sr₂RuO₄, which is highly quasi-2D. The other two GL terms, $f_2^{\text{SOC},8}$ and $f_2^{\text{SOC},9}$, describe the coupling between the in-plane $\mathbf{d}(\mathbf{k}) = \hat{z}(k_x, k_y)$ and out-of-plane $\mathbf{d}(\mathbf{k}) = k_z(\hat{x}, \hat{y})$ components within the same

E_u representation. Their appearance requires finite SOC to break the full pseudospin rotational symmetry. Note that such a coupling does not exist for the A_{1u} representation.

The mixing of the out-of-plane component to the in-plane chiral p -wave pairing state in E_u leads to a shift of the T_c away from its zero SOC value, T_c^0 . On the other hand, the helical p -wave states are unaffected by the mixing; therefore, the degeneracy among different p -wave states is in general lifted due to the shift. Hence it is important to understand the magnitude of this shift, and compare it to the effect of other SOC induced GL terms on T_c that we have discussed in Sec. III of the main text.

To that end, we first analyze the dependence of the GL coefficients associated with $f_2^{\text{SOC},8}$ and $f_2^{\text{SOC},9}$, a_8 and a_9 , on small parameters of the model that we consider [31]. Spin rotation symmetry breaking requires that, to leading order in η , $\{a_8, a_9\} \propto \eta/t$. Since the terms in $f_2^{\text{SOC},8}$ and $f_2^{\text{SOC},9}$ transform like $k_x k_z$ or $k_y k_z$ under spatial rotations, the two GL coefficients necessarily come from a \mathbf{k} space

average $\langle \dots k_x k_z \rangle$ or $\langle \dots k_y k_z \rangle$, which is nonzero only if the $k_x k_z$ or $k_y k_z$ dependence is compensated by interlayer hopping terms such as $t_{yz,xy} \sin k_x/2 \sin k_z/2 \cos k_y/2$ or $t_{xz,xy} \sin k_y/2 \sin k_z/2 \cos k_x/2$. As a consequence, to leading order in $t_{yz,xy}/t$ and $t_{xz,xy}/t$, $\{a_8, a_9\} \propto t_z/t$, where $t_z = \max\{|t_{yz,xy}|, |t_{xz,xy}|\}$. Combining the η/t and t_z/t dependence, we have $\{a_8, a_9\} \propto T_c^0(\eta t_z)/t^2$, where T_c^0 is a characteristic pairing temperature scale for zero SOC.

Now consider the T_c shift of the chiral p -wave pairing state due to the mixing. As mentioned above, we expect that, for Sr_2RuO_4 , the T_c of the in-plane and out-of-plane pairing components in the E_u representation, $T_{c,\text{in}}$ and $T_{c,\text{out}}$, satisfy $T_{c,\text{in}} \gg T_{c,\text{out}}$. So the T_c shift of the in-plane chiral p -wave pairing state due to the mixing can be well estimated from a second order non-degenerate perturbation theory, i.e., $\delta T_c \approx \max\{|a_8|^2, |a_9|^2\}/(T_{c,\text{in}} - T_{c,\text{out}})$, which leads to $\delta T_c/T_c \propto (\eta t_z)^2/t^4$. This shift is negligible compared with the contributions from other SOC induced terms that we have discussed in the main text, since $\eta/t \sim 0.1$ and $|t_z/t| \lesssim 0.1$ for Sr_2RuO_4 .

-
- [1] G. Luke, Y. Fudamoto, K. Kojima, M. Larkin, J. Merrin, B. Nachumi, Y. Uemura, Y. Maeno, Z. Mao, Y. Mori *et al.*, *Nature (London)* **394**, 558 (1998).
- [2] K. Ishida, H. Mukuda, Y. Kitaoka, K. Asayama, Z. Mao, Y. Mori, and Y. Maeno, *Nature (London)* **396**, 658 (1998).
- [3] J. Xia, Y. Maeno, P. T. Beyersdorf, M. M. Fejer, and A. Kapitulnik, *Phys. Rev. Lett.* **97**, 167002 (2006).
- [4] A. P. Mackenzie and Y. Maeno, *Rev. Mod. Phys.* **75**, 657 (2003).
- [5] C. Kallin and J. Berlinsky, *Rep. Prog. Phys.* **79**, 054502 (2016).
- [6] A. J. Leggett, *Rev. Mod. Phys.* **47**, 331 (1975).
- [7] N. Read and D. Green, *Phys. Rev. B* **61**, 10267 (2000).
- [8] C. Nayak, S. H. Simon, A. Stern, M. Freedman, and S. Das Sarma, *Rev. Mod. Phys.* **80**, 1083 (2008).
- [9] A. P. Mackenzie, T. Scaffidi, C. W. Hicks, and Y. Maeno, *Quantum Materials* **2**, 40 (2017).
- [10] M. Matsumoto and M. Sgrist, *J. Phys. Soc. Jpn.* **68**, 994 (1999).
- [11] J. R. Kirtley, C. Kallin, C. W. Hicks, E.-A. Kim, Y. Liu, K. A. Moler, Y. Maeno, and K. D. Nelson, *Phys. Rev. B* **76**, 014526 (2007).
- [12] C. W. Hicks, D. O. Brodsky, E. A. Yelland, A. S. Gibbs, J. A. N. Bruin, M. E. Barber, S. D. Edkins, K. Nishimura, S. Yonezawa, Y. Maeno, and A. P. Mackenzie, *Science* **344**, 283 (2014).
- [13] A. Steppke, L. Zhao, M. E. Barber, T. Scaffidi, F. Jerzembeck, H. Rosner, A. S. Gibbs, Y. Maeno, S. H. Simon, A. P. Mackenzie, and C. W. Hicks, *Science* **355**, eaaf9398 (2017).
- [14] A. Pustogow, Y. Luo, A. Chronister, Y.-S. Su, D. Sokolov, F. Jerzembeck, A. Mackenzie, C. Hicks, N. Kikugawa, S. Raghu *et al.*, *Nature (London)* **574**, 72 (2019).
- [15] K. Ishida, M. Manago, and Y. Maeno, arXiv:1907.12236.
- [16] M. W. Haverkort, I. S. Elfimov, L. H. Tjeng, G. A. Sawatzky, and A. Damascelli, *Phys. Rev. Lett.* **101**, 026406 (2008).
- [17] A. Tamai, M. Zingl, E. Rozbicki, E. Cappelli, S. Riccò, A. de la Torre, S. McKeown Walker, F. Y. Bruno, P. D. C. King, W. Meevasana, M. Shi, M. Radović, N. C. Plumb, A. S. Gibbs, A. P. Mackenzie, C. Berthod, H. U. R. Strand, M. Kim, A. Georges, and F. Baumberg, *Phys. Rev. X* **9**, 021048 (2019).
- [18] T. Scaffidi, J. C. Romers, and S. H. Simon, *Phys. Rev. B* **89**, 220510(R) (2014).
- [19] H. S. Røising, F. Flicker, T. Scaffidi, and S. H. Simon, *Phys. Rev. B* **98**, 224515 (2018).
- [20] D. F. Agterberg, T. M. Rice, and M. Sgrist, *Phys. Rev. Lett.* **78**, 3374 (1997).
- [21] M. Sgrist, D. Agterberg, A. Furusaki, C. Honerkamp, K. Ng, T. Rice, and M. Zhitomirsky, *Physica C (Amsterdam)* **317-318**, 134 (1999).
- [22] K.-K. Ng and M. Sgrist, *Physica B (Amsterdam)* **281-282**, 969 (2000).
- [23] K. K. Ng and M. Sgrist, *Europhys. Lett.* **49**, 473 (2000).
- [24] Y. Yanase and M. Ogata, *J. Phys. Soc. Jpn.* **72**, 673 (2003).
- [25] J. F. Annett, G. Litak, B. L. Györfy, and K. I. Wysokiński, *Phys. Rev. B* **73**, 134501 (2006).
- [26] S. Raghu, A. Kapitulnik, and S. A. Kivelson, *Phys. Rev. Lett.* **105**, 136401 (2010).
- [27] C. M. Puetter and H.-Y. Kee, *Europhys. Lett.* **98**, 27010 (2012).
- [28] Y. Yanase, S. Takamatsu, and M. Udagawa, *J. Phys. Soc. Jpn.* **83**, 061019 (2014).
- [29] L.-D. Zhang, W. Huang, F. Yang, and H. Yao, *Phys. Rev. B* **97**, 060510(R) (2018).
- [30] A. T. Römer, D. D. Scherer, I. M. Eremin, P. J. Hirschfeld, and B. M. Andersen, *Phys. Rev. Lett.* **123**, 247001 (2019).
- [31] H. S. Røising, T. Scaffidi, F. Flicker, G. F. Lange, and S. H. Simon, *Phys. Rev. Res.* **1**, 033108 (2019).
- [32] Q. H. Wang, C. Platt, Y. Yang, C. Honerkamp, F. C. Zhang, W. Hanke, T. M. Rice, and R. Thomale, *Europhys. Lett.* **104**, 17013 (2013).
- [33] W.-S. Wang, C.-C. Zhang, F.-C. Zhang, and Q.-H. Wang, *Phys. Rev. Lett.* **122**, 027002 (2019).
- [34] D. Vollhardt and P. Wolfle, *The Superfluid Phases of Helium 3* (Taylor & Francis, 1990).
- [35] A. Georges, L. d. Medici, and J. Mravlje, *Annu. Rev. Condens. Matter Phys.* **4**, 137 (2013).

- [36] W. Kohn and J. M. Luttinger, *Phys. Rev. Lett.* **15**, 524 (1965).
- [37] Y. Imai, K. Wakabayashi, and M. Sigrist, *Phys. Rev. B* **85**, 174532 (2012).
- [38] A. T. Rømer, T. A. Maier, A. Kreisel, I. Eremin, P. J. Hirschfeld, and B. M. Andersen, [arXiv:1909.00627](https://arxiv.org/abs/1909.00627).
- [39] M. Sigrist and K. Ueda, *Rev. Mod. Phys.* **63**, 239 (1991).
- [40] W. Huang and H. Yao, *Phys. Rev. Lett.* **121**, 157002 (2018).
- [41] S. Koikegami, Y. Yoshida, and T. Yanagisawa, *Phys. Rev. B* **67**, 134517 (2003).
- [42] C. Lupien, Ultrasound attenuation in the unconventional superconductor Sr_2RuO_4 , Ph.D. thesis, University of Toronto, 2002; S. Ghosh, A. Shekhter, F. Jerzembeck, N. Kikugawa, D. A. Sokolov, A. P. Mackenzie, C. W. Hicks, and B. J. Ramshaw (unpublished).
- [43] A. Ramires and M. Sigrist, *Phys. Rev. B* **100**, 104501 (2019).
- [44] M. Khodas and A. V. Chubukov, *Phys. Rev. Lett.* **108**, 247003 (2012).
- [45] D. F. Agterberg, V. Barzykin, and L. P. Gor'kov, *Phys. Rev. B* **60**, 14868 (1999).
- [46] V. Stanev and Z. Tešanović, *Phys. Rev. B* **81**, 134522 (2010).
- [47] W. Huang, T. Scaffidi, M. Sigrist, and C. Kallin, *Phys. Rev. B* **94**, 064508 (2016).

Chapter 5

Higher angular momentum pairing states in Sr_2RuO_4 in the presence of longer-range interactions

5.1 Preface

Recently, TRSB $d_{x^2-y^2} \pm ig_{xy(x^2-y^2)}$ pairing with symmetry-protected vertical line nodes along the (1,1,0) direction was proposed as an order parameter candidate from a phenomenological analysis. [27] This OP can be compatible with a wide variety of key experiments. [27] However, the stability of this state, especially of the g -wave component, in SRO is unclear. As far as we know, no g -wave pairing has been found in previous studies of SRO [120, 51, 106, 139, 107, 108, 121, 52, 118, 119], except in studies of orbital pairings that include sizable interband pairing.




Previous studies on the single-band Hubbard model found that both $d_{x^2-y^2}$ - and g -wave are dominant and nearly degenerate in the weak coupling limit when nearest-neighbor (NN) Coulomb interactions, V^{NN} , are included. [122] A recent study [97] extends this analysis to a multi-band SRO model and finds that neither $d_{x^2-y^2}$ nor g -wave pairing is favored within RPA. Instead, they suggest a TRSB $s' + id_{xy}$ solution with gap minima near (1,1,0) which, like $d_{x^2-y^2} + ig$ order, can explain the NMR Knight shift and ultrasound data. (s' labels nodal s -wave states.)

However, the model employed in Ref.[97] does not capture the orbital dependence of the longer-range interactions, which is not negligible in SRO.

Another effect that may help stabilize the g -wave state is the B_{2g} channel SOC, $\eta_{B_{2g}}$. [140, 98] $\eta_{B_{2g}}$ involves in-plane next-nearest neighbor (NNN) Ru sites and is allowed by symmetry in the presence of the atomic SOC and the inter-orbital hybridizations between d_{xz} and d_{yz} orbitals. [140] It is expected to be the leading SOC term beyond the atomic SOC in SRO as it can utilize the intermediate p -orbitals through several hopping channels. The effect of $\eta_{B_{2g}}$ is explored in Ref.[98] within the so-called Hund’s coupling mean-field approach where superconducting pairings are generated by attractive on-site interactions due to strong Hund’s coupling. Both $d_{x^2-y^2}$ - and g -, including a $d_{x^2-y^2} + ig$, are stabilized in the presence of a strong $\eta_{B_{2g}}$, $\eta_{B_{2g}}/\eta \gtrsim 0.4$. It has been pointed out that Hund’s pairings are, in general, less favored than spin-fluctuation pairings in SRO due to its nesting features in Refs. [119, 137]. Thus, it is important to study the effects of $\eta_{B_{2g}}$ more generally.

In this chapter, we study the stability of the $d_{x^2-y^2}$ - and $g_{xy(x^2-y^2)}$ -wave states, as well as $d_{x^2-y^2} \pm ig_{xy(x^2-y^2)}$, in SRO models in the presence of longer-range interactions within RPA. (See Appendix C for details.) We find that the inclusion of in-plane NNN Coulomb repulsions, together with $\eta_{B_{2g}}$ and/or orbital-anisotropy of the non-local interactions, can have a significant impact on the stability of both $d_{x^2-y^2}$ - and g -wave pairing channels. As a result, accidentally degenerate or near degenerate $d_{x^2-y^2} + ig$ can be stable for a specific range of parameters. We further study the properties, such as nodal structures, in-plane field spin-susceptibility, and spontaneous edge current, of the realized $d_{x^2-y^2} + ig$ pairing. We find that, compared with the realized $s' + id_{xy}$ [97] and mixed helical pairings [96], the $d_{x^2-y^2} + ig$ pairing is more compatible with existing experiments. [112, 113, 92, 93, 37, 38, 39] Our study identifies the critical effects that stabilize the $d_{x^2-y^2} + ig$ state, which has been somewhat discounted relative to other states like $s' + id_{xy}$ in previous studies.

5.2 Publication

Higher angular momentum pairing states in Sr₂RuO₄ in the presence of longer-range interactionsXin Wang ¹, Zhiqiang Wang ² and Catherine Kallin¹¹*Department of Physics and Astronomy, McMaster University, Hamilton, Ontario, Canada L8S 4M1*²*James Franck Institute, University of Chicago, Chicago, Illinois 60637, USA* (Received 27 July 2022; revised 26 September 2022; accepted 7 October 2022; published 25 October 2022)

The superconducting symmetry of Sr₂RuO₄ remains a puzzle. Time-reversal symmetry breaking $d_{x^2-y^2} + ig_{xy(x^2-y^2)}$ pairing has been proposed for reconciling multiple key experiments. However, its stability remains unclear. In this work, we theoretically study the superconducting instabilities in Sr₂RuO₄, including the effects of spin-orbit coupling (SOC), in the presence of both local and longer-range interactions within a random-phase approximation. We show that the inclusion of second-nearest-neighbor repulsions, together with nonlocal SOC in the B_{2g} channel or orbital-anisotropy of the nonlocal interactions, can have a significant impact on the stability of both $d_{x^2-y^2}$ - and g -wave pairing channels. We analyze the properties, such as Knight shift and spontaneous edge current, of the realized $d_{x^2-y^2} + ig$, $s' + id_{xy}$, and mixed helical pairings in different parameter spaces, and we find that the $d_{x^2-y^2} + ig$ solution is in better agreement with the experimental data.

DOI: [10.1103/PhysRevB.106.134512](https://doi.org/10.1103/PhysRevB.106.134512)**I. INTRODUCTION**

The nature of the unconventional superconductivity in Sr₂RuO₄ (SRO) remains an outstanding open question after more than 27 years of study, despite this material being simpler than the high-temperature cuprates in many respects. The samples are clean, and superconductivity condenses from a well-defined Fermi liquid normal state so that it is natural to take an itinerant-electron perspective, where superconductivity is an instability of the Fermi surface (FS). However, despite intense efforts, an order parameter (OP) that is consistent with all the key experimental observations is lacking.

A multicomponent OP is inferred from a variety of experiments, including muon spin rotation (μ SR) [1,2], polar Kerr [3], Josephson relation [4], and ultrasound measurements [5–7]. The multicomponents can be degenerate by symmetry, belonging to the two-dimensional irreducible representations (irrep.) of the crystal point symmetry group, or be degenerate accidentally, belonging to two distinct one-dimensional irreps.

Possible symmetry-related OPs for a crystal with D_{4h} symmetry are spin-triplet $p_x \pm ip_y$ with E_u symmetry and spin-singlet $d_{xz} \pm id_{yz}$ (E_g). Both are difficult to reconcile with experiments. The $p_x \pm ip_y$ pairing is inconsistent with the significant drop of the in-plane Knight shift below T_c observed in recent NMR experiments [8,9]. The $d_{xz} \pm id_{yz}$ has symmetry-protected horizontal line nodes at $k_z = 0$ that conflict with thermal conductivity and scanning tunneling microscopy (STM) studies, where vertical line nodes are indicated [10,11]. In addition, it would produce a jump in the elastic modulus associated with shear B_{1g} strain, which is not observed in experiments [5]. Indeed, no $d_{xz} \pm id_{yz}$ pairing has been found in microscopic calculations for SRO [12,13] except in studies of orbital pairings that include sizable interband pairing [14,15]. We briefly discuss interband pairing in the conclusions.

The above difficulties associated with the symmetry-related OPs focused attention on the accidental degeneracy scenario, even though it usually requires fine-tuning. The need for fine-tuning can be somewhat relaxed by considering inhomogeneous states, where, for example, the second OP is induced by inhomogeneous strains near dislocations [16,17]. This scenario is consistent with recent μ SR [2] and ultrasound attenuation measurements [7].

Recently, a time-reversal symmetry breaking (TRSB) $d_{x^2-y^2} \pm ig_{xy(x^2-y^2)}$ pairing with symmetry-protected vertical line nodes has been proposed to explain multiple key experiments [18,19]. Although $d_{x^2-y^2}$ -wave is stable in SRO models in the presence of on-site interactions [20–27], g -wave is not favored. It has been suggested that the g -wave state may be stabilized by longer-range interactions based on studies of single-band Hubbard models [28,29]. A recent study [27] found that neither $d_{x^2-y^2}$ - nor g -wave pairing is favored in SRO in the presence of orbital-isotropic longer-range Coulomb repulsions. Instead, an $s' + id_{xy}$ solution was suggested with gap minima near (1,1,0), which, like $d_{x^2-y^2} + ig$ order, is also consistent with NMR and ultrasound measurements (s' labels nodal s -wave states). The calculations in Ref. [27] are performed in an intermediate Hubbard- U regime, $U \approx 1.1t$, where t is the primary hopping amplitude.

It was recently reported in Ref. [15] that the g -wave pairing could be stabilized in SRO by strong nonlocal SOC in the B_{2g} channel ($\eta_{B_{2g}}$) within the so-called Hund's coupling mean-field approach. In this framework, superconducting pairings are generated by attractive on-site interactions due to strong Hund's coupling. However, Refs. [13,30] suggested that, in general, Hund's pairing is less favored than spin-fluctuation pairing in SRO due to its nesting features. Therefore, it is of interest to study the effects of $\eta_{B_{2g}}$ in SRO more generally.

In this work, we study the superconducting instabilities in the presence of both local and longer-range Coulomb

repulsions in SRO in a realistic multiorbital model, with local and nonlocal SOC, over a range of U and other interaction parameters, including the effects of orbital anisotropies. One focus is identifying the effects that stabilize g -wave. In this paper, the effective interactions are treated within the random-phase approximation (RPA). Our studies include both the weak-coupling limit and finite- U RPA. While RPA includes some higher-order scatterings associated with finite interactions and has been shown to agree with other methods for a one-band model [31], it is unclear whether RPA provides a more accurate description for SRO beyond weak coupling.

We find that nearest-neighbor (NN) Coulomb repulsion, V^{NN} , combined with next-nearest-neighbor (NNN) repulsion, V^{NNN} , promotes g -wave pairing. Depending on the strength of U , g -wave pairing becomes the leading or the first subleading pairing for a substantial range of V^{NN} and V^{NNN} . $\eta_{B_{2g}}$ and orbital anisotropies of V^{NN} and V^{NNN} can further stabilize the g -wave phase. Although $d_{x^2-y^2}$ pairing is not favored in the presence of orbital-independent V^{NN} and V^{NNN} , it can be stabilized by the effects of $\eta_{B_{2g}}$ and longer-range interaction anisotropies. As a result, accidentally/near-degenerate $d_{x^2-y^2}$ and g pairing can be obtained at the phase boundaries in certain parameter spaces. We also study the physical properties of the realized $d_{x^2-y^2} \pm ig$ pairing and compare it with another two recently proposed pairing candidates: the $s' \pm id_{xy}$ [27] and a mixed helical pairing [32]. We find that the $d_{x^2-y^2} + ig$ is somewhat in better agreement with the experiments.

The paper is organized as follows. The microscopic model and method employed are discussed in Sec. II and the results of our RPA calculations are presented in Sec. III. The physical properties of the possible two-component OPs are discussed in Sec. IV. Section V contains our conclusions and further discussion, including a brief discussion of interband pairing that is found in some studies of SRO [15,33]. Finally, some details are left to Appendixes, including the derivation of the effective interactions in Appendix A, the effects of V^{NN} in Appendix B, the more detailed analysis of the stability of $d_{x^2-y^2}$ - and g -wave pairing in Appendix C, and the general effects of longer-range interaction anisotropies in Appendix D.

II. MODEL AND METHOD

We consider the microscopic model Hamiltonian for the three conduction bands of SRO,

$$H = H_K + H_{\text{int}}, \quad (1)$$

where H_K is the kinetic energy part that gives rise to the normal state FSs, and H_{int} is the interaction.

H_K can be written in the basis $\Psi(\mathbf{k}) = [c_{\mathbf{k},1,\uparrow}; c_{\mathbf{k},2,\uparrow}; c_{\mathbf{k},3,\downarrow}; c_{\mathbf{k},1,\downarrow}; c_{\mathbf{k},2,\downarrow}; c_{\mathbf{k},3,\uparrow}]^T$, so that it is block-diagonal,

$$\hat{H}_K(\mathbf{k}) = \begin{pmatrix} H_{\uparrow\uparrow}(\mathbf{k}) & 0 \\ 0 & H_{\downarrow\downarrow}(\mathbf{k}) \end{pmatrix}, \quad (2)$$

where $\{1, 2, 3\} = \{d_{yz}, d_{xz}, d_{xy}\}$ orbitals, and $c^\dagger(c)$ is the electron creation (annihilation) operator,

$$H_{ss}(\mathbf{k}) = \begin{pmatrix} \epsilon_{yz,\mathbf{k}} & g_{\mathbf{k}} + is\eta & -s\eta - i\eta_{\mathbf{k}}^{B_{2g}} \\ g_{\mathbf{k}} - is\eta & \epsilon_{xz,\mathbf{k}} & i\eta + s\eta_{\mathbf{k}}^{B_{2g}} \\ -s\eta + i\eta_{\mathbf{k}}^{B_{2g}} & -i\eta + s\eta_{\mathbf{k}}^{B_{2g}} & \epsilon_{xy,\mathbf{k}} \end{pmatrix}, \quad (3)$$

with $s = 1(-1)$ for spin $\uparrow(\downarrow)$. $\epsilon_{yz(xz),\mathbf{k}} = -2t \cos k_{y(x)} - 2t^\perp \cos k_{x(y)} - \mu$ and $\epsilon_{xy,\mathbf{k}} = -2t'(\cos k_x + \cos k_y) - 4t'' \cos k_x \cos k_y - \mu_c$ describe intraorbital hoppings; $g_{\mathbf{k}} = -4t''' \sin k_x \sin k_y$ is the hopping between d_{xz} and d_{yz} orbitals. η is the atomic SOC, and $\eta_{\mathbf{k}}^{B_{2g}} = 4\eta_{B_{2g}} \sin k_x \sin k_y$ is the nonlocal SOC in the B_{2g} channel. Diagonalizing \hat{H}_K gives three doubly degenerate energy bands labeled by band index, $\{\alpha, \beta, \gamma\}$, and pseudospin, $\sigma = \uparrow(\downarrow)$. The band parameters are $(t, t^\perp, t''', t', t'', \mu, \mu_c) = (1, 0.11, 0.05, 0.8, 0.32, 1.05, 1.1)t$, which capture the overall band structure and FS sheets of SRO. For now, the magnitudes of η and $\eta_{B_{2g}}$ are left undetermined and will be suitably varied to analyze the effects of SOC. The resulting FSs for two different values of the SOC parameters are shown in Fig. 9 in Appendix C.

The interaction Hamiltonian (with on-site and longer-range interactions) is

$$H_{\text{int}} = \frac{U}{2} \sum_{i,a} n_{ia\uparrow} n_{ia\downarrow} + \frac{U'}{2} \sum_{i,a \neq b,s,s'} n_{ias} n_{ibs'} + \frac{J}{2} \sum_{i,a \neq b,s,s'} c_{ias}^\dagger c_{ibs'}^\dagger c_{ias} c_{ibs} + \frac{J'}{2} \sum_{i,a \neq b,s \neq s'} c_{ias}^\dagger c_{ias'}^\dagger c_{ibs} c_{ibs'} \quad (4a)$$

$$+ \sum_{i,\delta = \{\pm\hat{x}, \pm\hat{y}\}, a,b,s,s'} \frac{V_{ab,\delta}^{\text{NN}}}{2} n_{i,a,s} n_{i+\delta,b,s'} + \sum_{i,\delta = \{\pm\hat{x}\pm\hat{y}\}, a,b,s,s'} \frac{V_{ab,\delta}^{\text{NNN}}}{2} n_{i,a,s} n_{i+\delta,b,s'}, \quad (4b)$$

where $n_{i,a,s} \equiv c_{i,a,s}^\dagger c_{i,a,s}$ is the spin- and orbital-resolved electron density operator at site i . Equation (4a) describes the on-site interaction, where U (U') is the intra- (inter)orbital repulsive Hubbard interaction, J is the Hund's coupling, and J' is the pair hopping. Equation (4b) describes the longer-range interactions, where $V_{ab,\delta}^{\text{NN}}$ ($V_{ab,\delta}^{\text{NNN}}$) is the NN (NNN) Coulomb repulsion.

For simplicity, we take $J' = J$ and $U' = U - 2J$ [SO(3) symmetry] [34] and ignore the $d_{xy/z}$ anisotropy due to hybridization with oxygen orbitals [35,36], but we will briefly comment on the effect of this anisotropy in Sec. V. $V_{ab,\delta}^{\text{NN}}$ and $V_{ab,\delta}^{\text{NNN}}$ are t_{2g} orbital-dependent, and their orbital-anisotropies are defined as

$$\alpha_{ab,\delta} \equiv \frac{V_{ab,\delta}^{\text{NN}}}{V_{11,\hat{x}}^{\text{NN}}} - 1 \equiv \frac{V_{ab,\delta}^{\text{NN}}}{V^{\text{NN}}} - 1, \quad (5)$$

$$\beta_{ab,\delta} \equiv \frac{V_{ab,\delta}^{\text{NNN}}}{V_{11,\hat{x}\pm\hat{y}}^{\text{NNN}}} - 1 \equiv \frac{V_{ab,\delta}^{\text{NNN}}}{V^{\text{NNN}}} - 1, \quad (6)$$

where $V_{11,\hat{x}}^{\text{NN}}$ ($V_{11,\hat{x}+\hat{y}}^{\text{NNN}}$) is the intraorbital interaction between two NN (NNN) d_{yz} orbitals with $\delta = \hat{x}$ ($\delta = \hat{x} + \hat{y}$). $\{\alpha_{ab,\delta}\} = 0$ ($\{\beta_{ab,\delta}\} = 0$) describes the orbital-isotropic V^{NN} (V^{NNN}) case. From rotation symmetry in the t_{2g} orbital space, there are six free orbital-anisotropy parameters: α_{33} , $\alpha_{23,\pm\hat{x}}$, α_{12} , β_{33} , β_{13} , and β_{12} . Here, and in the following, we drop the subscript δ in $\alpha_{33,\delta}$, $\alpha_{12,\delta}$, and $\beta_{ab,\delta}$ as these parameters are δ -independent. Following from symmetry,

$$\alpha_{22,\pm\hat{y}} = \alpha_{11,\pm\hat{x}} = 0, \quad (7a)$$

$$\alpha_{33} = \alpha_{22,\pm\hat{x}} = \alpha_{11,\pm\hat{y}}, \quad (7b)$$

$$\alpha_{12} = \alpha_{23,\pm\hat{y}} = \alpha_{13,\pm\hat{x}}, \quad (7c)$$

$$\alpha_{23,\pm\hat{x}} = \alpha_{13,\pm\hat{y}}, \quad (7d)$$

and

$$\beta_{11} = \beta_{22} = 0, \quad (8a)$$

$$\beta_{13} = \beta_{23}. \quad (8b)$$

To study the superconducting instabilities, we obtain effective pairing vertices within the RPA. Taking the static limit, the effective interaction in the orbital basis reads

$$V_{\text{eff}} = \frac{1}{4} \sum_{\mathbf{k}, \mathbf{k}'} [\Gamma(\mathbf{k}, \mathbf{k}')]_{\bar{a}_3 \bar{a}_4}^{\bar{a}_1 \bar{a}_2} c_{\mathbf{k}, \bar{a}_1}^\dagger c_{-\mathbf{k}, \bar{a}_3}^\dagger c_{-\mathbf{k}, \bar{a}_4} c_{\mathbf{k}', \bar{a}_2}, \quad (9)$$

where $\bar{a}_1 = \{a_1, s_1\}$ is a composite index that labels both orbital and spin, and

$$[\Gamma(\mathbf{k}, \mathbf{k}')]_{\bar{a}_3 \bar{a}_4}^{\bar{a}_1 \bar{a}_2} = \sum_{\delta, \delta'} \sum_{i, j=\{1,2\}} \left[\begin{pmatrix} e^{i\mathbf{k}\cdot\delta} & 0 \\ 0 & e^{i\mathbf{k}\cdot\delta} \end{pmatrix} [\tilde{W}(\delta)]_{\bar{a}_3 \bar{a}_4}^{\bar{a}_1 \bar{a}_2} \begin{pmatrix} e^{-i\mathbf{k}'\cdot\delta} & 0 \\ 0 & e^{i\mathbf{k}'\cdot\delta} \end{pmatrix} \right. \quad (10a)$$

$$\left. - \begin{pmatrix} e^{i\mathbf{k}\cdot\delta} & 0 \\ 0 & e^{i\mathbf{k}\cdot\delta} \end{pmatrix} [\tilde{W}(\delta)] \chi^{\text{RPA}}(\mathbf{k}, \mathbf{k}'; \delta, \delta') [\tilde{W}(\delta')]_{\bar{a}_3 \bar{a}_4}^{\bar{a}_1 \bar{a}_2} \begin{pmatrix} e^{-i\mathbf{k}'\cdot\delta'} & 0 \\ 0 & e^{i\mathbf{k}'\cdot\delta'} \end{pmatrix} \right. \quad (10b)$$

$$\left. + \begin{pmatrix} e^{i\mathbf{k}\cdot\delta} & 0 \\ 0 & e^{i\mathbf{k}\cdot\delta} \end{pmatrix} [\tilde{W}(\delta)] \chi^{\text{RPA}}(\mathbf{k}, -\mathbf{k}'; \delta, \delta') [\tilde{W}(\delta')]_{\bar{a}_3 \bar{a}_2}^{\bar{a}_1 \bar{a}_4} \begin{pmatrix} e^{i\mathbf{k}'\cdot\delta'} & 0 \\ 0 & e^{-i\mathbf{k}'\cdot\delta'} \end{pmatrix} \right]_{ij}. \quad (10c)$$

Here,

$$\chi^{\text{RPA}}(\mathbf{k}, \mathbf{k}'; \delta, \delta') = \frac{1}{1 + \chi(\mathbf{k}, \mathbf{k}'; \delta, \delta') \tilde{W}(\delta')} \chi(\mathbf{k}, \mathbf{k}'; \delta, \delta') \quad (11)$$

is a generalized δ -dependent RPA particle-hole susceptibility matrix, with $\chi(\mathbf{k}, \mathbf{k}'; \delta, \delta')$ the corresponding bare susceptibility, whose matrix element is

$$\chi_{\bar{b}_3 \bar{b}_4}^{\bar{b}_1 \bar{b}_2}(\mathbf{k}, \mathbf{k}'; \delta, \delta') = \sum_{\mathbf{p}} \sum_{\alpha, \beta} \frac{n_F(\xi_{\mathbf{p}}^\alpha) - n_F(\xi_{\mathbf{p}-(\mathbf{k}-\mathbf{k}')}^\beta)}{\xi_{\mathbf{p}-(\mathbf{k}-\mathbf{k}')}^\beta - \xi_{\mathbf{p}}^\alpha} \mathcal{F}_{\bar{b}_3 \bar{b}_4}^{\bar{b}_1 \bar{b}_2}(\alpha, \beta; \mathbf{p}, \mathbf{k} - \mathbf{k}') \begin{pmatrix} e^{-i\mathbf{k}'\cdot\delta + i\mathbf{k}\cdot\delta'} & e^{-i\mathbf{k}'\cdot\delta + i\mathbf{p}\cdot\delta'} \\ e^{-i\mathbf{p}\cdot\delta + i\mathbf{k}\cdot\delta'} & e^{-i\mathbf{p}\cdot\delta - \delta'} \end{pmatrix}. \quad (12)$$

$\mathcal{F}_{\bar{b}_3 \bar{b}_4}^{\bar{b}_1 \bar{b}_2}(\alpha, \beta; \mathbf{p}, \mathbf{q})$ is the form factor associated with the band-to-orbital transformations,

$$\mathcal{F}_{\bar{b}_3 \bar{b}_4}^{\bar{b}_1 \bar{b}_2}(\alpha, \beta; \mathbf{p}, \mathbf{q}) = \psi_{\bar{b}_2}^\alpha(\mathbf{p}) [\psi_{\bar{b}_3}^\alpha(\mathbf{p})]^* [\psi_{\bar{b}_1}^\beta(\mathbf{p} - \mathbf{q})]^* \psi_{\bar{b}_4}^\beta(\mathbf{p} - \mathbf{q}). \quad (13)$$

In these equations, α and β are energy band labels (including the pseudospin). $\xi_{\mathbf{k}}^\alpha$ is the α th band dispersion, $\psi_{\bar{b}}^\alpha(\mathbf{k})$ is the corresponding matrix element of the orbital-to-band transformation, and n_F is the Fermi-Dirac distribution function. $\tilde{W}(\delta)$ is the bare interaction, H_{int} , written in \mathbf{k} -space but with its \mathbf{k} -dependence peeled off and absorbed into the definition of the susceptibility χ , which reduces the computational complexity. (Similar methods have been introduced in Ref. [27].) This is achieved by introducing a redundant 2×2 subspace, indexed by $\{i, j\}$ in Eq. (10). More details can be found in Appendix A. \tilde{W} , χ , and χ^{RPA} are $N \times N$ matrices for given momenta with $N = 6 \times 6 \times 9 \times 2$, where 6×6 comes from the two sets of composite indices $\{\bar{a}_1, \bar{a}_2\}$, each of which consists of three orbitals \otimes two spin species, nine from the label of neighboring sites $\delta = \{0, \hat{x}, \hat{y}, -\hat{x}, -\hat{y}, \hat{x} + \hat{y}, -\hat{x} - \hat{y}, -\hat{x} - \hat{y}, \hat{x} - \hat{y}\}$, and two from the additional subspace label $i = \{1, 2\}$. Equation (12) will be evaluated at low temperatures where χ is temperature-independent and using a sufficiently large \mathbf{k} -mesh in the first Brillouin zone [29]. Throughout this work,

we choose $k_B T = 0.001t$ and a 512×512 grid mesh for the integration.

Transforming V_{eff} in Eq. (9) to the band basis leads to

$$V_{\text{eff}} = \sum_{\mathbf{k}, \mathbf{k}'} \sum_{\alpha, \beta} \Gamma^{\alpha\beta}(\mathbf{k}, \mathbf{k}') c_{\alpha}^\dagger(\mathbf{k}) c_{\alpha}^\dagger(-\mathbf{k}) c_{\beta}(-\mathbf{k}') c_{\beta}(\mathbf{k}'), \quad (14)$$

where

$$\Gamma^{\alpha\beta}(\mathbf{k}, \mathbf{k}') = \frac{1}{4} \sum_{\bar{a}_i} \Gamma_{\bar{a}_3 \bar{a}_4}^{\bar{a}_1 \bar{a}_2}(\mathbf{k}, \mathbf{k}') [\psi_{\bar{a}_1}^\alpha(\mathbf{k})]^* [\psi_{\bar{a}_3}^\alpha(-\mathbf{k})]^* \times \psi_{\bar{a}_4}^\beta(-\mathbf{k}') \psi_{\bar{a}_2}^\beta(\mathbf{k}'). \quad (15)$$

Note that we have used Γ for both the orbital- and band-basis effective interaction, which are distinguished by their indices. Projecting $\Gamma^{\alpha\beta}$ onto the FS, one can determine the superconducting instabilities by solving the following BCS linearized

gap equation [21]:

$$\sum_{\beta} \int_{S_{\beta}} \frac{dk'_{\parallel}}{|S_{\beta}|} g(\mathbf{k}_{\alpha}, \mathbf{k}'_{\beta}) \psi(\mathbf{k}'_{\beta}) = \lambda \psi(\mathbf{k}_{\alpha}), \quad (16)$$

where

$$g(\mathbf{k}_{\alpha}, \mathbf{k}'_{\beta}) = \sqrt{\frac{\rho_{\alpha} \bar{v}_{F,\alpha}}{v_F(\mathbf{k}_{\alpha})}} \Gamma^{\alpha\beta}(\mathbf{k}_{\alpha}, \mathbf{k}'_{\beta}) \sqrt{\frac{\rho_{\beta} \bar{v}_{F,\beta}}{v_F(\mathbf{k}'_{\beta})}}, \quad (17)$$

and $\lambda = \rho V_{\text{eff}}$, where ρ is the density of states at the Fermi level [37]. In Eq. (16), all momenta are defined on the FS. S_{β} is the FS of the β th band, which is a one-dimensional contour for our two-dimensional calculations; $|S_{\beta}|$ is its corresponding area (or contour length). ρ_{α} is the density of states of the α th band, and the average of the norm of the Fermi velocity is given by $\bar{v}_{F,\alpha}^{-1} = \int_{S_{\alpha}} \frac{dk_{\parallel}}{|S_{\alpha}|} v_F^{-1}(\mathbf{k}_{\alpha})$. After discretizing Eq. (16), it becomes a matrix equation to be solved numerically. To get good convergence, we discretize the FS contours with ~ 1000 equally spaced points. Alternatively, one can take an easier method by discretizing the whole first Brillouin zone, but only keeping states that lie within a thin energy window from the Fermi level. However, as pointed out in Ref. [38], a much larger number of points is then required for the same level of accuracy.

The critical temperature, T_c , is determined by the most negative eigenvalue, λ , through $T_c \sim \mathcal{W} e^{-1/|\lambda|}$, where \mathcal{W} is of the order of the bandwidth. The superconducting gap is

$$\Delta(\mathbf{k}_{\alpha}) \propto \sqrt{\frac{v_F(\mathbf{k}_{\alpha})}{\rho_{\alpha} \bar{v}_{F,\alpha}}} \psi(\mathbf{k}_{\alpha}), \quad (18)$$

where $\Delta(\mathbf{k}_{\alpha})$ can be written in the *pseudospin* basis as

$$\Delta(\mathbf{k}_{\alpha}) = \begin{pmatrix} \Delta_{\uparrow\uparrow} & \Delta_{\uparrow\downarrow} \\ \Delta_{\downarrow\uparrow} & \Delta_{\downarrow\downarrow} \end{pmatrix} \quad (19)$$

for a given \mathbf{k}_{α} point on one of the three FS sheets.

III. PAIRING RESULTS IN THE PRESENCE OF LONGER-RANGE INTERACTIONS

We first ignore the effects of nonlocal SOC, $\eta_{B_{2g}} = 0$, but we include a sizable atomic SOC of $\eta/t = 0.2$. Similar calculations have been conducted in several theoretical works with only local interactions, where s' -, $d_{x^2-y^2}$ -, helical, or chiral pairing is obtained depending on microscopic details [22,24,26]. As in Ref. [27], we investigate the ef-

fects of orbital-independent NN Coulomb repulsions, V^{NN} , in Appendix B. We include a wide range of Hubbard- U from weak to intermediate coupling, i.e., $U/t \in (10^{-4}, 1.1)$, as U can strongly influence the leading pairing within the RPA [22,26,31]. Hund's coupling is set as $J/U = 0.2$ as obtained via the constrained local-density approximation [39] and the constrained RPA [36]. The size of V^{NN} for SRO is not clear. For cuprates with identical crystal structures, V^{NN}/U is about [40] 0.2, and this value was used in Ref. [27]. As Ru $4d$ orbitals are more extended than Cu $3d$ orbitals, V^{NN}/U for SRO may be larger. One finds $V^{\text{NN}}/U \approx 0.38$ from integrals over Slater-type Ru d orbitals where screening effects and hybridizations between the Ru d and oxygen p orbitals are neglected [41]. By comparison, the same calculation for Cu $d_{x^2-y^2}$ orbitals gives $V^{\text{NN}}/U \approx 0.22$, suggesting the effects of hybridization and screening in the cuprates essentially cancel each other. Guided by this analysis, we perform calculations for SRO in the range of $V^{\text{NN}}/U \in (0, 0.4)$. We find that V^{NN} has little effect in stabilizing g -wave pairing and tends to destabilize the $d_{x^2-y^2}$ -wave phase. However, it favors helical pairing in the weak- U regime, and d_{xy} -wave at intermediate values of U . As a result, $s' + id_{xy}$, $d_{x^2-y^2} + id_{xy}$, or a mixed helical state can be obtained (at phase boundaries) in different regimes of the interaction parameter space (see Fig. 7 in Appendix B).

Our results for intermediate- U are in rough agreement with Ref. [27], except for the absence of the d_{xy} phase there. We find the d_{xy} state may be overtaken by s' if we increase T or decrease N_{FS} , the number of patching points used to solve the linearized gap equation. The sensitivity to temperature, even at relatively low temperatures, has been noted previously in the context of similar RPA calculations [42]. In all our calculations, we choose a sufficiently low temperature for the susceptibility calculations so that the results no longer change with decreasing temperature.

In this section, we focus on the superconducting instabilities in the presence of both V^{NN} and V^{NNN} . We first ignore the effects of orbital anisotropies of V^{NN} and V^{NNN} . The ratio of $V^{\text{NNN}}/V^{\text{NN}}$ can be roughly estimated through integrals over Ru $4d$ orbitals, as discussed above for V^{NN}/U , which gives $V^{\text{NNN}}/V^{\text{NN}} \sim 0.7$. This neglects hybridization and screening, the combined effect of which likely reduces $V^{\text{NNN}}/V^{\text{NN}}$. Our calculations will focus on the range of $V^{\text{NNN}}/V^{\text{NN}} \in (0, 0.7)$.

Nonzero V^{NN} and V^{NNN} produce a correction, $\delta\Gamma(\mathbf{k}, \mathbf{k}')$, to the effective pairing interaction. For weak V^{NN} and V^{NNN} , $\delta\Gamma(\mathbf{k}, \mathbf{k}')$ is dominated by the bare- V^{NN} and V^{NNN} contributions, which can be schematically written as

$$\delta\Gamma^{(1)}(\mathbf{k}, \mathbf{k}') \sim V^{\text{NN}} [\cos(k_x - k'_x) + \cos(k_y - k'_y)] \mathcal{F}_{o \rightarrow b}(\mathbf{k}, \mathbf{k}') + 2V^{\text{NNN}} \cos(k_x - k'_x) \cos(k_y - k'_y) \mathcal{F}_{o \rightarrow b}(\mathbf{k}, \mathbf{k}') \quad (20a)$$

$$= \sum_{\Lambda, i} (g_{\Lambda, i}^{\text{NN}} + g_{\Lambda, i}^{\text{NNN}}) [\phi^{\Lambda, i}(\mathbf{k})]^* \phi^{\Lambda, i}(\mathbf{k}'), \quad (20b)$$

where $\phi^{\Lambda, i}$ denotes the i th lattice harmonic of irrep. Λ in the D_{4h} group and $g_{\Lambda, i}^{\text{NN(NNN)}}$ is the corresponding pairing interaction strength. In the presence of SOC, $\mathcal{F}_{o \rightarrow b}$, the form factor associated with orbital-to-band transformation, carries nontrivial pseudospin structures [see Eq. (15)], which are omitted here for a qualitative discussion.

In the single-band case, $\mathcal{F}_{o \rightarrow b}(\mathbf{k}, \mathbf{k}') = 1$ and $\delta\Gamma^{(1)}(\mathbf{k}, \mathbf{k}')$ can be greatly simplified. $g_{\Lambda, j}^{\text{NNN}}$ is nonzero and repul-

sive only for NNN harmonics in the $\Lambda = \{A_{1g}, B_{2g}, E_u\} = \{s', d_{xy}, p\}$ irrep. with eigenfunctions $\phi^{s', 2} = \cos k_x \cos k_y$,

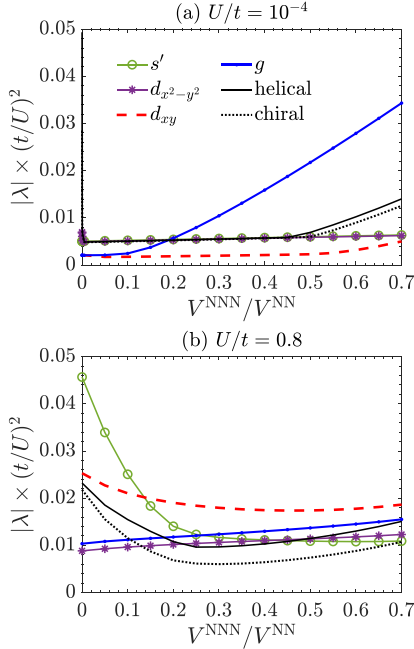


FIG. 1. Superconducting instabilities as a function of $V^{\text{NNN}}/V^{\text{NN}}$ for (a) $U/t = 10^{-4}$ and (b) $U/t = 0.8$, where helical and s' -wave is favored at $V^{\text{NNN}} = 0$, respectively. Only the largest eigenvalue (in magnitude) of each irrep. is shown. $\eta/t = 0.2$, $\eta_{B_{2g}} = 0$, $J/U = 0.2$, and $V^{\text{NN}}/U = 0.25$.

$\phi^{d_{xy},2} = \sin k_x \sin k_y$, and $\phi^{p_{x(y)},2} = \cos k_{y(x)} \sin k_{x(y)}$ [28]. Similarly, as discussed in Appendix B and in Ref. [28], $g_{\Lambda,i}^{\text{NN}}$ is repulsive for $\phi^{s',1} = \cos k_x + \cos k_y$, $\phi^{d_{x^2-y^2},1} = \cos k_x - \cos k_y$, and $\phi^{p_{x/y},1} = \sin k_{x/y}$. In summary, $\delta\Gamma^{(1)}$ has repulsive components in all the pairing channels except for g -wave. In the multiband model with SOC, our numerical results show that $\delta\Gamma^{(1)}$ remains repulsive as long as $J/U \leq 1/3$ and also has small components in the g -wave channel.

For sizable V^{NN} and V^{NNN} , the second-order correction, $\delta\Gamma^{(2)}$, becomes important. $\delta\Gamma^{(2)}$ usually involves higher angular harmonics and can be attractive due to fluctuations. For example, $V^{\text{NN}}(\mathbf{k}, \mathbf{k}')\tilde{\chi}(\mathbf{k} - \mathbf{k}')V^{\text{NNN}}(\mathbf{k}, \mathbf{k}')$ is one of the second-order correction terms from the bubble diagram in Fig. 6(b), where $\tilde{\chi}$ represents the bubble; the expansion of this term into angular harmonics contains the g -wave component with basis functions such as $\phi^{g,4}(\mathbf{k}) = \phi^{d_{xy},2}(\mathbf{k})\phi^{d_{x^2-y^2},1}(\mathbf{k}) = \sin k_x \sin k_y (\cos k_x - \cos k_y)$ for the single band case. This argument applies even in the presence of multiorbitals and SOC. Thus, g -wave can be promoted by the combined effects of V^{NN} and V^{NNN} .

Figure 1 shows the effects of V^{NNN} on the leading superconducting instability in each irrep. in the case of $V^{\text{NN}}/U = 0.25$ for (a) $U/t = 10^{-4}$ and (b) $U/t = 0.8$, where helical and s' -wave is favored without $V^{\text{NNN}}/V^{\text{NN}}$, respectively. One sees that g -wave pairing is enhanced by V^{NNN} . In the weak- U case,

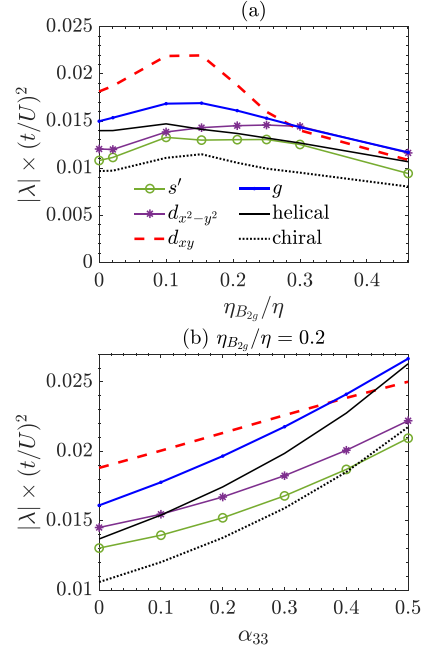


FIG. 2. (a) Effects of $\eta_{B_{2g}}/\eta$ on the superconducting instabilities in different channels for $U/t = 0.8$, $V^{\text{NN}}/U = 0.25$, $V^{\text{NNN}}/V^{\text{NN}} = 0.65$. (b) Evolutions of the leading superconducting instabilities as a function of anisotropy parameter α_{33} for $\eta_{B_{2g}}/\eta = 0.2$, where $\alpha_{33} = 0$ represents the isotropic longer-range interaction case in (a). Other anisotropy parameters are chosen as $(\alpha_{23,\pm\hat{x}}, \alpha_{12}, \beta_{33}, \beta_{13}, \beta_{12}) = (1, 0.4, 0.33, 0.17, 0)\alpha_{33}$.

the g -wave state becomes the leading order at $V^{\text{NNN}}/V^{\text{NN}} \gtrsim 0.2$, as other pairing channels are largely suppressed by the bare and repulsive V^{NN} and V^{NNN} . An $s' + ig$ pairing can be obtained close to the multicritical point (i.e., $V^{\text{NNN}}/V^{\text{NN}} \approx 0.2$), where the s' - and g -wave channels are near-degenerate. For intermediate U , g -wave order becomes the first subleading pairing for a substantial range of $V^{\text{NNN}}/V^{\text{NN}}$, $V^{\text{NNN}}/V^{\text{NN}} \gtrsim 0.3$, whereas d_{xy} -wave pairing is dominant. We also find that s' -wave pairing is significantly suppressed by V^{NNN} -induced corrections at the RPA level, in contrast to the case studied in Ref. [13], where the suppression effect is moderate. In summary, g -wave is the leading or the first subleading pairing for a broad range of U , V^{NN} , and V^{NNN} (not shown), while $d_{x^2-y^2}$ -wave is not favored.

$\eta_{B_{2g}}$ can strongly impact the higher angular momentum pairings as it involves NNN Ru sites. Figure 2(a) shows the superconducting instabilities as a function of $\eta_{B_{2g}}/\eta$ in the intermediate U case ($V^{\text{NN}}/U = 0.25$ and $V^{\text{NNN}}/V^{\text{NN}} = 0.65$), where g -wave is the first subleading order at $\eta_{B_{2g}} = 0$. $\eta_{B_{2g}}/\eta$ is increased by decreasing η linearly while increasing $\eta_{B_{2g}}$, so that the sum of η and $\eta_{B_{2g}}$ is constant [15]. The chemical potential for the d_{xy} orbitals is adjusted, $\tilde{\mu}_c = \mu_c + \delta\mu_c$, to fit the ARPES data [43]. In Fig. 2(a), we find that both $d_{x^2-y^2}$ - and g -wave pairings are dominant and near/accidentally degenerate at $\eta_{B_{2g}}/\eta \gtrsim 0.3$. The very close overlap of these

two states for $\eta_{B_{2g}}/\eta \gtrsim 0.3$ is accidental. In general, we find $d_{x^2-y^2}$ - and g -wave states are the first two leading pairings in the range of $V^{\text{NN}}/U \in (0.2, 0.3)$ and $V^{\text{NNN}}/V^{\text{NN}} > 0.5$ (in Fig. 11 of Appendix C). Also, for the weak- U case, $d_{x^2-y^2}$ and g -wave are found to be the first two leading channels at a much smaller $\eta_{B_{2g}}/\eta$, $\eta_{B_{2g}}/\eta > 0.15$ (see Fig. 13 in Appendix C).

We note that the required $\eta_{B_{2g}}/\eta$ for the presence of both $d_{x^2-y^2}$ and g -wave phase is much larger than the density functional theory (DFT) estimate ~ 0.02 [15]. However, it has been pointed out that SOC is underestimated in the DFT calculations and can be further enhanced by correlation effects [35,43–46]. In addition, in the following, we will show that this value can be reduced by including longer-range interaction anisotropies.

The $d_{x^2-y^2} + ig$ pairing stabilized by $\eta_{B_{2g}}$ is also observed in a recent study using a mean-field approach, although a much larger $\eta_{B_{2g}}/\eta \gtrsim 0.45$ is required there [15]. In addition, our RPA calculations find that nonzero V^{NN} and V^{NNN} are necessary to obtain the $d_{x^2-y^2} + ig$ -wave phase, unlike in Ref. [15].

We further consider the effects of the longer-range interaction anisotropies. The magnitudes of the orbital-anisotropies, defined in Eqs. (5) and (6), largely depend on the spread of the d -orbitals. We can roughly estimate the anisotropy parameters through integrals over Ru $4d$ Slater-type orbitals, where we find that the largest orbital anisotropy parameter, α_{33} , is about 0.12. As discussed above, such estimations do not include the hybridization and screening effects. These effects substantially enhance the interaction anisotropies in HgBa₂CuO₄. For example, the NN interaction for Cu $d_{x^2-y^2}$ -orbitals is about 25% larger than that for $d_{3z^2-r^2}$ -orbitals according to Ref. [47], while a direct Slater integral gives only 3%. Similarly, the hybridization and screening effects may also enhance the estimates in SRO. In comparison to HgBa₂CuO₄, the orbitals are larger (which should increase the hybridization) but the Ru-O bonds are substantially less anisotropic in different crystal directions (which decreases the enhancement). Consequently, in the absence of a detailed calculation, we treat the anisotropy as a variable parameter. Figure 2(b) shows the superconducting instabilities as a function of α_{33} in the case of $\eta_{B_{2g}}/\eta = 0.2$. The relative magnitudes of other parameters are chosen as $(\alpha_{23,\pm\hat{x}}, \alpha_{12}, \beta_{33}, \beta_{13}, \beta_{12}) = (1, 0.4, 0.33, 0.17, 0)\alpha_{33}$, based on rough estimates through Ru t_{2g} Slater-type orbitals integrals. (Details can be found in Appendix D.) The t_{2g} orbital-anisotropy increases the stability of the g -wave so that it becomes the leading order for $\alpha_{33} \gtrsim 0.36$. We note that the required α_{33} to stabilize the g -wave is much larger than its Slater orbital estimate, 0.12. However, this does not need to be an obstruction since we also found that the required α_{33} can be much smaller in some parts of the parameter space, for example, with larger V^{NN} and V^{NNN} and/or in the weak- U regime (not shown). Furthermore, as discussed above, the actual α_{33} is expected to be larger than our simple estimate. Although $d_{x^2-y^2}$ -wave pairing is not favored, it is promoted relative to the d_{xy} -channel, suggesting that the $d_{x^2-y^2}$ phase can be enlarged by orbital anisotropies. More discussion on the anisotropy effects are shown in Appendix D, where, in particular, we find that α_{33} helps to stabilize g -wave pairing, and β_{33} favors $d_{x^2-y^2}$ -wave for finite- U .

IV. PROPERTIES OF THE STABLE PAIRING STATES

In Sec. III, we show that $d_{x^2-y^2}$ - and g -wave pairing can be favored in SRO by the effects of longer-range interactions and $\eta_{B_{2g}}$. Consequently, at certain parameters, $d_{x^2-y^2} + ig$ pairing can be realized. In this section, we explore the gap structure, spin susceptibility, and spontaneous edge current of $d_{x^2-y^2} + ig$ pairing using the stable OP configurations found at the phase boundary: $(\eta_{B_{2g}}/\eta, U/t, V^{\text{NN}}/U, V^{\text{NNN}}/V^{\text{NN}}) = (0.3, 0.8, 0.25, 0.65)$, to see if it can be compatible with experiments on SRO. In addition, we also compare these properties of $d_{x^2-y^2} + ig$ pairing to those of two other recently proposed pairings, $s' + id_{xy}$ and mixed helical pairing, which are obtained at $(\eta_{B_{2g}}/\eta, U/t, V^{\text{NN}}/U, V^{\text{NNN}}/V^{\text{NN}}) = (0, 0.8, 0.05, 0)$ and $(0, 0.0001, 0.15, 0)$, respectively. The stability of the latter two TRSB pairing candidates is discussed in Appendix B with nonzero V^{NN} . The $s' + id_{xy}$ can be obtained for a finite- U , as in Ref. [27], while the mixed helical pairings are realized in the weak- U limit. We also find that the splitting between helical pairings in B_{1u} and B_{2u} (or A_{1u} and A_{2u}) is rather small throughout $V^{\text{NN}} \in (0, 0.3)$ in the weak- U limit as shown in Fig. 8 (in Appendix B). The result at $V^{\text{NN}} = 0$, i.e., with only on-site interactions, is consistent with previous studies both in 2D [26] and in 3D [12].

A. Gap structure

The gaps are of similar size on all bands and exhibit strong gap anisotropy with multiple nodes or near-nodes on the FS for all three pairings (shown in Fig. 3). We find $|\Delta|_{\text{min}}/|\Delta|_{\text{max}} \sim 10\%$ [48] in the realized $s' + id_{xy}$ and mixed helical states. Since the experiment estimate of $|\Delta|_{\text{min}}/|\Delta|_{\text{max}}$ is $\lesssim 3\%$ [10,49], further fine-tuning of the interaction parameters is needed to make the $s' + id_{xy}$ and the mixed helical states compatible with the experiments. In agreement with the previous studies [21,22,24,27], the locations of the minima are slightly off the $k_x = \pm k_y$ diagonal lines and are robust against the change of interaction parameters. Thus, future experiments on the precise location of the nodes or near-nodes can help in identifying the pairing symmetry.

B. Spin susceptibility and Knight shift

Recent NMR measurements reveal a substantial in-plane Knight shift drop below T_c [8,9], which is most straightforwardly explained by spin-singlet pairings. It has been argued that spin-triplet helical pairings could also be consistent with the susceptibility drop [32].

Figure 4 shows the calculated spin susceptibility as a function of temperature for the three pairings. The residual $\chi(T=0)$ is roughly similar for all three pairings due to SOC, which mixes spin-singlet and -triplet states. $\chi(T=0)/\chi_n$ is about 28%, 23%, and 50% for the $d_{x^2-y^2} + ig$, $s' + id_{xy}$, and mixed helical pairing, respectively. Taking into account experimental precision along with vortex and disorder effects, the $s' + id_{xy}$ and $d_{x^2-y^2} + ig$ pairings are in better agreement with the experiments. It might be difficult to clearly distinguish these two pairings in Knight shift measurements, especially if the $s' + id_{xy}$ had extremely deep gap minima, i.e., $|\Delta|_{\text{min}}/|\Delta|_{\text{max}} < 3\%$, which is expected to increase the residual spin susceptibility. Nevertheless, the calculated $\chi(T=$

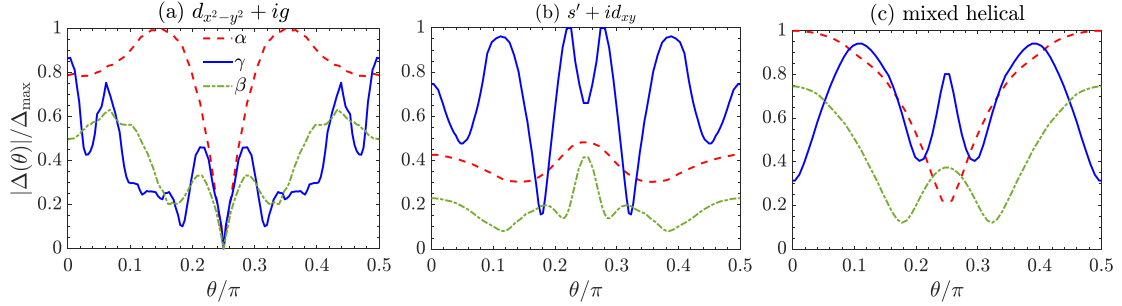


FIG. 3. Gap function profiles of three TRSB solutions (a) $d_{x^2-y^2} + ig$, (b) $s' + id_{xy}$, and (c) mixed-helical, along the three FS contours in one quadrant of the first BZ. The FS contour of each band is parametrized by the angle of the vector $\mathbf{k}_F = k_F(\theta)(\cos \theta, \sin \theta)$. Angle θ is measured from (π, π) for the α band, and from $(0, 0)$ for β and γ bands. The three states are obtained at phase boundaries where their two respective components are degenerate. The band/interaction parameters for the phase boundaries are $(\eta_{B_{2g}}/\eta, U/t, V^{\text{NN}}/U, V^{\text{NNN}}/V^{\text{NN}}) =$ (a) $(0.3, 0.8, 0.25, 0.65)$, (b) $(0, 0.8, 0.05, 0)$, and (c) $(0, 0.0001, 0.15, 0)$. Note, for the nonunitary mixed-helical pairing, because $|\Delta_{\downarrow\downarrow}| \ll |\Delta_{\uparrow\uparrow}|$, only the latter is shown.

$0)/\chi_n$ is much higher than the upper bound of 10% suggested by the experiments [51]. We note that the experimental interpretations are complicated by the difficulties in disentangling the orbital and spin contributions. Our results for the $s' + id_{xy}$ pairing are consistent with Ref. [27].

C. Spontaneous edge current

A TRSB superconducting state may support finite spontaneous edge currents, which are expected to be detected by high sensitivity magnetic scanning microscopy. Experiments on SRO show no evidence for such edge currents, suggesting that the current is either absent or too tiny to be resolved [53–55]. It has been pointed out that the spontaneous edge current can be dramatically reduced by gap anisotropies [52,56], indicating that the three pairings may be reconciled with the null results in experiments, although often fine-tuning is required.

The spontaneous edge current for the $d_{x^2-y^2} + ig$ and $s' + id_{xy}$ pairings is sensitive to the edge orientation: the current

is generally finite at $(1, 0, 0)$ surfaces and vanishes at $(1, 1, 0)$ surfaces. For the mixed helical pairing, the current is independent of the edge orientation. As shown in Fig. 5, the predicted edge currents at the $(1, 0, 0)$ surfaces, $J_y(x)$, for the three pairings are much smaller than the simple chiral p -wave case. In addition, there is a sign change in $J_y(x)$ for the $d_{x^2-y^2} + ig$ pairing, which significantly reduces the total integrated edge current, $I_y = \int dx J_y(x)$. In particular, this current is compatible with the experiments [53], since $I_y^{d_{x^2-y^2}+ig}/I_y^{\text{chiral-}p} \approx 0.6\%$, where $I_y^{\text{chiral-}p}$ is the simple chiral p -wave result [57]. This current ratio is 19% and 36% for the $s' + id_{xy}$ and mixed helical pairings, respectively. The larger current reduction in the $d_{x^2-y^2} + ig$ state is a result of the higher angular harmonics in the gap functions and should be robust since it comes from an intrinsic property of the bulk superconducting state. We note that the $s' + id_{xy}$ and mixed helical pairings may also support edge currents smaller than the measurable limit, however this would need fine-tuning.

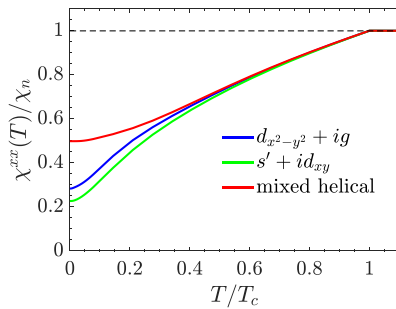


FIG. 4. The temperature dependence of the spin susceptibility (normalized by the normal state value χ_n) for the three OP pairings, calculated in the presence of a small Zeeman field in the x -direction and with Fermi-liquid corrections [9,50] included. We set $k_B T_c = 0.005t$, and the maximum magnitude of the gap is $|\Delta|_{\text{max}} = 0.015t$. These calculations follow those in Ref. [12].

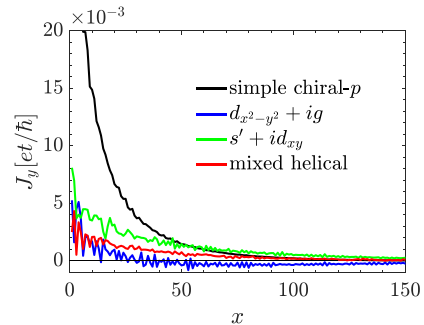


FIG. 5. Distribution of zero-temperature spontaneous edge current for the three pairings compared with simple chiral p -wave. A superconducting region of width $L_S = 800$ sites was taken with surface along $(1,0,0)$. We set $k_B T_c = 0.005t$, and the maximum magnitude of the gap is $|\Delta|_{\text{max}} = 0.015t$. These calculations follow those in Ref. [52], and lattice constant is defined to be unity.

Our results for the mixed helical pairing are in rough agreement with Ref. [32].

V. CONCLUSIONS

Within the RPA, we find that both $d_{x^2-y^2}$ - and g -wave can be stabilized by the effects of longer-range interactions and $\eta_{B_{2g}}$, and that accidentally/near-degenerate $d_{x^2-y^2} + ig$ can be stable for a specific range of parameters. We also calculate the physical properties of the realized $d_{x^2-y^2} + ig$ state and compare it with the realized $s' + id_{xy}$ [27] and mixed helical pairings [32]. We find that, although the $s' + id_{xy}$ pairing is as competitive as the $d_{x^2-y^2} + ig$, and is better than the mixed helical pairing, in explaining the spin susceptibility data [8,9], the $d_{x^2-y^2} + ig$ state is more compatible with experimental evidence of the existence of nodes/near-nodes [10,11] and the absence of spontaneous edge current [53–55] than the other two proposals.

Since $T_c \sim e^{-1/|\lambda|}$, the TRSB phase would occur only when the interaction parameters are tuned essentially right at the phase boundaries, where $T_c^{d_{x^2-y^2}} \approx T_c^g$. As pointed out in Refs. [16,17], the relative stability of the $d_{x^2-y^2}$ - and g -wave states can be sensitive to local strains, so that in the presence of such strains, one may have coexisting domains of g -wave and $d_{x^2-y^2}$ -wave order. In this case, time-reversal symmetry can be broken at domain walls between different strain regions [16]. Reference [17] shows that strain-inhomogeneities can couple a single-component primary OP, e.g., $d_{x^2-y^2}$ (g)-wave, to a subleading pairing state, e.g., g ($d_{x^2-y^2}$)-wave, and break time-reversal symmetry. As perfect degeneracy of the $d_{x^2-y^2}$ and g -wave is not required, the $d_{x^2-y^2} + ig$ state is expected to be stabilized in a broader parameter regime compared to a homogeneous $d_{x^2-y^2} + ig$ state. Recent studies show that the inhomogeneous TRSB domain walls may provide a route to explaining the observation of half-quantum vortices [16], heat capacity [58], and ultrasound attenuation measurements [7] on SRO. Our calculations suggest that even modest strains may be sufficient for such a scenario since we find $d_{x^2-y^2}$ and g -wave to be the first two leading orders over a range of parameters.

The RPA formalism we employed here is limited to small values of the Coulomb interaction, $U \lesssim O(t)$, it neglects correlation effects away from the FS, and it neglects many diagrams in calculating the effective interaction. Thus, the RPA approach may not adequately capture the physics of SRO with typical estimates of $U \sim O(eV) \sim 10t$ [35,36,59,60]. A recent study [31] compares the weak-coupling RG, RPA, and dynamical cluster approximation (DCA) approaches within the single-band Hubbard model, and it finds good agreement among these approaches, in the region where they can be compared, suggesting a smooth crossover in pairing states within the Hubbard model from weak to strong coupling. While such an analysis has not been done for the multiband case, it suggests that the RPA approach can provide valuable insight into superconducting pairings in SRO. We believe that some of the observations about the effects of interaction-anisotropy and $\eta_{B_{2g}}$ in our RPA calculations will survive at strong coupling since they are independent of the strength of U . Also, beyond the weak- U limit, correlation effects away from the FS can be important to the superconducting instabilities. For example,

the RPA approach may underestimate the stability of $d_{x^2-y^2}$ pairing by not adequately accounting for the effect of the van Hove singularity away from, but near, the FS of the γ band. Thus, the functional RG approach [20,61] with longer-range interactions would be of interest since it can be employed in the sizable U -regime and it treats states away from the FS more accurately.

The superconducting pairings discussed above are classified according to the irrep. of the point group of the lattice in the band basis. Recently, it was argued that the above analysis of the pairing function is insufficient [62–64]. Instead, some recent studies of SRO focus on the orbital basis approach and propose specific interorbital pairings [15,33]. Reference [33] finds an odd frequency interorbital singlet pairing is favored by solving the linearized Eliashberg equation. Using a mean-field approach, Ref. [15] finds stable interorbital $d_{x^2-y^2} + ig$ pairing at $J/U > 1/3$. Transforming these interorbital pairings into the band basis, one finds that they both support substantial interband pairing away from the FS. By contrast, the approach we take ignores interband pairing.

The relative size of intraband and interband pairing in SRO is an open question. However, since the minimum energy difference between electron states on different bands and with opposite momentum is much larger than the superconducting pairing energy in SRO, one might expect interband pairing to be small. For example, interband pairing might be reduced by finite frequency effects that are usually ignored in weak-coupling formalisms. In any case, one does not expect interband pairing to significantly impact the relative stability of different pairing states close to T_c , since interband pairing does not open up a gap anywhere on the FS. In particular, interband pairing only contributes in order Δ^2/E_F to the pairing gap at the FSs. Nevertheless, interband pairing can be important for some properties, including the polar Kerr effect [3], which has been measured at high frequencies where all superconducting contributions are of order $(\Delta/E_F)^2$ or smaller. While the approach of Ref. [33] could, in principle, address the size of interband pairing, the calculations are restricted to temperatures $\gtrsim 300$ K, not only well above T_c , but also above the temperature where a well-defined FS emerges. One would likely need to go to much lower temperatures to reliably capture the relative size of intraband and interband pairing. Since the presence of substantial interband pairing could impact the interpretation of some experiments, this is an interesting avenue for future studies.

Lastly, we comment on the effects of $d_{xy/z}$ anisotropy we have neglected throughout this paper. In the crystal field with D_{4h} symmetry, the Ru t_{2g} states split into an e_g doublet (d_{xz} , d_{yz}) and a b_{2g} singlet (d_{xy}). As the RuO bond in the c -direction is elongated, d_{xy} orbitals are more spread out than (d_{xz} , d_{yz}) orbitals, suggesting stronger interactions for d_{xy} orbitals. This anisotropy would slightly suppress g -wave pairing. However, it will not significantly affect our key results, as it is very small in SRO, i.e., the spread of the d_{xy} orbital is larger than (d_{xz} , d_{yz}) by about 7% [35,36].

ACKNOWLEDGMENTS

We would like to thank Sung-Sik Lee, Erik S. Sørensen, and Wen Huang for useful discussions. This research is

supported by the Natural Sciences and Engineering Research Council. This work was made possible by the facilities of the Shared Hierarchical Academic Research Comput-

ing Network [65] and Compute/Calcul Canada. Z.W. is supported by James Franck Institute at the University of Chicago.

APPENDIX A: SUSCEPTIBILITY AND EFFECTIVE INTERACTION

In this Appendix, we show the derivation of the effective interaction in the Cooper pair channel that takes into account on-site, NN, and NNN interactions. The bare interaction Hamiltonian is defined in Eq. (4), and it can be rewritten in a more compact form as

$$H_{\text{int}} = \frac{1}{4} \sum_{i,\delta,\tilde{a}_i} ([W_1(\delta)]_{\tilde{a}_3\tilde{a}_4}^{\tilde{a}_1\tilde{a}_2} c_{i,\tilde{a}_1}^\dagger c_{i+\delta,\tilde{a}_3}^\dagger c_{i,\tilde{a}_2} c_{i+\delta,\tilde{a}_4} + [W_2(\delta)]_{\tilde{a}_3\tilde{a}_4}^{\tilde{a}_1\tilde{a}_2} c_{i,\tilde{a}_1}^\dagger c_{i+\delta,\tilde{a}_3}^\dagger c_{i,\tilde{a}_2} c_{i+\delta,\tilde{a}_4}). \quad (\text{A1})$$

$\tilde{a}_j = \{a_j, s_j\}$ is a composite index that labels both orbital (a_j) and spin (s_j). $[W_1(\delta)]_{\tilde{a}_3\tilde{a}_4}^{\tilde{a}_1\tilde{a}_2}$ has the following nonzero elements:

$$[W_1(0)]_{\tilde{a}\tilde{s},\tilde{a}\tilde{s}}^{as,as} = U, \quad [W_1(0)]_{\tilde{b}\tilde{s},\tilde{b}\tilde{s}}^{as,as} = U', \quad [W_1(0)]_{\tilde{a}\tilde{s},\tilde{b}\tilde{s}}^{as,bs} = J', \quad [W_1(0)]_{\tilde{b}\tilde{s},\tilde{a}\tilde{s}}^{as,bs} = J, \quad [W_1(0)]_{\tilde{b}\tilde{s},\tilde{b}\tilde{s}}^{as,as} = U' - J, \quad (\text{A2a})$$

$$[W_1(\delta \neq 0)]_{\tilde{a}\tilde{s},\tilde{a}\tilde{s}}^{as,as} = [W_1(\delta \neq 0)]_{\tilde{a}\tilde{s},\tilde{a}\tilde{s}}^{as,as} = V_{aa,\delta}, \quad [W_1(\delta \neq 0)]_{\tilde{b}\tilde{s},\tilde{b}\tilde{s}}^{as,as} = [W_1(\delta \neq 0)]_{\tilde{b}\tilde{s},\tilde{b}\tilde{s}}^{as,as} = V_{ab,\delta}, \quad (\text{A2b})$$

where $a \neq b$ and $\tilde{s} = -s$. $W_2(\delta)$ is related to $W_1(\delta)$ such that the whole interaction matrix coefficient is antisymmetric with respect to exchanges of indices of two creation or annihilation operators in H_{int} :

$$[W_2(\delta)]_{\tilde{a}_3\tilde{a}_4}^{\tilde{a}_1\tilde{a}_2} = [W_2(\delta)]_{\tilde{a}_1\tilde{a}_2}^{\tilde{a}_3\tilde{a}_4} = -[W_1(\delta)]_{\tilde{a}_3\tilde{a}_4}^{\tilde{a}_1\tilde{a}_2} = -[W_1(\delta)]_{\tilde{a}_1\tilde{a}_2}^{\tilde{a}_3\tilde{a}_4}. \quad (\text{A3})$$

$[W_1(\delta)]_{\tilde{a}_3\tilde{a}_4}^{\tilde{a}_1\tilde{a}_2}$ (and, similarly, $[W_2(\delta)]_{\tilde{a}_3\tilde{a}_4}^{\tilde{a}_1\tilde{a}_2}$) is a 36×36 matrix, for each value of δ , with $(\tilde{a}_1, \tilde{a}_2)$ its row index and $(\tilde{a}_3, \tilde{a}_4)$ the column index.

By Fourier transformation of the interaction, we obtain

$$H_{\text{int}}(\mathbf{k}) = \frac{1}{4} \sum_{\mathbf{k}_i, \tilde{a}_i} \sum_{\delta} [W(\mathbf{k}_1, \mathbf{k}_2; \mathbf{k}_3, \mathbf{k}_4, \delta)]_{\tilde{a}_3\tilde{a}_4}^{\tilde{a}_1\tilde{a}_2} c_{\mathbf{k}_1, \tilde{a}_1}^\dagger c_{\mathbf{k}_3, \tilde{a}_3}^\dagger c_{\mathbf{k}_4, \tilde{a}_4} c_{\mathbf{k}_2, \tilde{a}_2}, \quad (\text{A4})$$

where

$$[W(\mathbf{k}_1, \mathbf{k}_2; \mathbf{k}_3, \mathbf{k}_4, \delta)]_{\tilde{a}_3\tilde{a}_4}^{\tilde{a}_1\tilde{a}_2} = \sum_{i,j=\{1,2\}} \left[\begin{array}{cc} e^{i\mathbf{k}_1 \cdot \delta} & 0 \\ 0 & e^{i\mathbf{k}_1 \cdot \delta} \end{array} \underbrace{\begin{pmatrix} [W_1(\delta)]_{\tilde{a}_3\tilde{a}_4}^{\tilde{a}_1\tilde{a}_2} & 0 \\ 0 & [W_2(\delta)]_{\tilde{a}_3\tilde{a}_4}^{\tilde{a}_1\tilde{a}_2} \end{pmatrix}}_{[\tilde{W}(\delta)]_{\tilde{a}_3\tilde{a}_4}^{\tilde{a}_1\tilde{a}_2}} \begin{pmatrix} e^{-i\mathbf{k}_2 \cdot \delta} & 0 \\ 0 & e^{-i\mathbf{k}_2 \cdot \delta} \end{pmatrix} \right]_{ij}. \quad (\text{A5})$$

Here, we introduce an additional but redundant 2×2 subspace, and the sum is taken over all the matrix elements in this subspace. In the form of Eq. (A5), the momenta dependence of the bare interaction is factored out, which can facilitate our derivation of the RPA effective interactions, as will become clear in the following.

In the presence of longer-range interactions, the bare interaction depends on the momentum transfer, $\mathbf{k}_1 - \mathbf{k}_2$ and $\mathbf{k}_1 - \mathbf{k}_4$. As a result, in deriving the effective interaction, the interaction vertex in the higher-order diagrams involves the internal loop momentum \mathbf{p} , unlike the on-site interaction case where the bare interaction is momentum-independent [21,22,24]. The additional \mathbf{p} -dependence poses a challenge for writing diagrammatic contributions to the RPA effective interaction as a simple geometric and algebraic sum. This computational complexity can be reduced by factoring out the \mathbf{p} -dependence in the interaction vertex and absorbing it into the definition of particle-hole susceptibility as in Ref. [27]. We follow a similar approach to that in Ref. [27] except that we start with the antisymmetrized bare interaction. This parametrization of the interaction will prove convenient in the following derivation of the RPA effective interaction.

The exchange of the spin and orbital fluctuations can induce attractions responsible for superconductivity, even if the bare interaction is repulsive. To take into account this effect, one calculates the effective electron-electron interaction, $[\Gamma(\mathbf{k}, \mathbf{k}')]_{\tilde{a}_3\tilde{a}_4}^{\tilde{a}_1\tilde{a}_2}$ in Eq. (9), by summing up one-particle irreducible diagrams of different orders in the bare interaction, Eq. (A4). The first-order contribution [shown in Fig. 6(a)] is

$$[\Gamma(\mathbf{k}, \mathbf{k}')^{(1)}]_{\tilde{a}_3\tilde{a}_4}^{\tilde{a}_1\tilde{a}_2} = \sum_{\delta} \sum_{i,j=\{1,2\}} \left[\begin{pmatrix} e^{i\mathbf{k} \cdot \delta} & 0 \\ 0 & e^{i\mathbf{k} \cdot \delta} \end{pmatrix} [\tilde{W}(\delta)]_{\tilde{a}_3\tilde{a}_4}^{\tilde{a}_1\tilde{a}_2} \begin{pmatrix} e^{-i\mathbf{k}' \cdot \delta} & 0 \\ 0 & e^{-i\mathbf{k}' \cdot \delta} \end{pmatrix} \right]_{ij}. \quad (\text{A6})$$

The two second-order diagrams are shown in Figs. 6(b) and 6(c). The contribution of the bubble diagram is expressed as

$$\begin{aligned} [\Gamma(\mathbf{k}, \mathbf{k}')^{(2, \text{bubble})}]_{\tilde{a}_3\tilde{a}_4}^{\tilde{a}_1\tilde{a}_2} &= - \sum_{\delta, \delta'} \sum_{\tilde{b}_i} \sum_{\mathbf{p}} [W(\mathbf{k}, \mathbf{k}'; \mathbf{p} - (\mathbf{k} - \mathbf{k}'), \mathbf{p}, \delta)]_{\tilde{b}_1\tilde{b}_2}^{\tilde{a}_1\tilde{a}_2} \sum_{\alpha, \beta} \frac{n_F(\xi_{\mathbf{p}}^\alpha) - n_F(\xi_{\mathbf{p} - (\mathbf{k} - \mathbf{k}')}^\beta)}{\xi_{\mathbf{p} - (\mathbf{k} - \mathbf{k}')}^\beta - \xi_{\mathbf{p}}^\alpha} \\ &\times \mathcal{F}_{\tilde{b}_3\tilde{b}_4}^{\tilde{b}_1\tilde{b}_2}(\alpha, \beta; \mathbf{p}, \mathbf{k} - \mathbf{k}') [W(\mathbf{p}, \mathbf{p} - (\mathbf{k} - \mathbf{k}'); -\mathbf{k}, -\mathbf{k}', \delta')]_{\tilde{a}_3\tilde{a}_4}^{\tilde{b}_3\tilde{b}_4} \end{aligned} \quad (\text{A7})$$

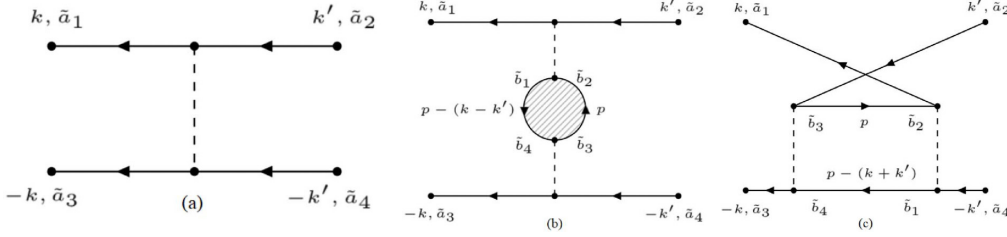


FIG. 6. The first- and second-order diagrams which contribute to the effective interaction in the Cooper pair channel. Note that each interaction line carries four joint composite indices $\tilde{a}_i = (a_i, s_i)$. The internal momentum label, p , is a short-hand notation for frequency and momentum, both of which need to be summed over; on the other hand, for the external momenta, k and k' , we only consider zero frequency, i.e., the retardation effect in the effective pairing interaction is neglected.

$$= - \sum_{\delta, \delta'} \sum_{i, j=\{1,2\}} \left[\begin{pmatrix} e^{ik \cdot \delta} & 0 \\ 0 & e^{ik \cdot \delta} \end{pmatrix} [\tilde{W}(\delta) \chi(\mathbf{k}, \mathbf{k}'; \delta, \delta') \tilde{W}(\delta')]_{\tilde{a}_3 \tilde{a}_4}^{\tilde{a}_1 \tilde{a}_2} \begin{pmatrix} e^{-ik' \cdot \delta'} & 0 \\ 0 & e^{ik' \cdot \delta'} \end{pmatrix} \right]_{ij}. \quad (\text{A8})$$

$[\chi(\mathbf{k}, \mathbf{k}'; \delta, \delta')]_{\tilde{b}_3 \tilde{b}_4}^{\tilde{b}_1 \tilde{b}_2}$ is the bare susceptibility defined in Eq. (12). $\xi_{\mathbf{k}}^{\alpha(\beta)}$ is the $\alpha(\beta)$ -band dispersion, n_F is the Fermi-Dirac distribution function, and $\mathcal{F}_{\tilde{b}_3 \tilde{b}_4}^{\tilde{b}_1 \tilde{b}_2}(\alpha, \beta; \mathbf{p}, \mathbf{q})$ is the form factor associated with the band-to-orbital transformations given in Eq. (13). From Eqs. (A7) and (A8), the \mathbf{p} dependence in the interaction vertices, $[W(\mathbf{k}, \mathbf{k}'; \mathbf{p} - (\mathbf{k} - \mathbf{k}'), \mathbf{p}, \delta)]$ and $[W(\mathbf{p}, \mathbf{p} - (\mathbf{k} - \mathbf{k}'); -\mathbf{k}, -\mathbf{k}', \delta')]$, is factorized and absorbed into the integrand of $[\chi(\mathbf{k}, \mathbf{k}'; \delta, \delta')]$.

Similarly, the ladder diagram contribution is

$$[\Gamma(\mathbf{k}, \mathbf{k}')^{(2, \text{ladder})}]_{\tilde{a}_3 \tilde{a}_4}^{\tilde{a}_1 \tilde{a}_2} = \sum_{\delta, \delta'} \sum_{i, j=\{1,2\}} \left[\begin{pmatrix} e^{ik \cdot \delta} & 0 \\ 0 & e^{ik \cdot \delta} \end{pmatrix} [\tilde{W}(\delta) \chi(\mathbf{k}, -\mathbf{k}'; \delta, \delta') \tilde{W}(\delta')]_{\tilde{a}_3 \tilde{a}_2}^{\tilde{a}_1 \tilde{a}_4} \begin{pmatrix} e^{ik' \cdot \delta'} & 0 \\ 0 & e^{-ik' \cdot \delta'} \end{pmatrix} \right]_{ij}. \quad (\text{A9})$$

Notice that $[\Gamma(\mathbf{k}, \mathbf{k}')^{(2, \text{ladder})}]_{\tilde{a}_3 \tilde{a}_4}^{\tilde{a}_1 \tilde{a}_2} = -[\Gamma(\mathbf{k}, -\mathbf{k}')^{(2, \text{bubble})}]_{\tilde{a}_2 \tilde{a}_4}^{\tilde{a}_1 \tilde{a}_4}$. As a result, the effective interaction at the order of $(U/t)^2$ satisfies the same antisymmetric property as the bare interaction in Eq. (A4). The effective interaction vertex at the RPA level [in Eq. (10)] is obtained by summing up the bare interaction in Eq. (A6), and a geometric series of the bubble and ladder diagrams. The latter contribution takes a form similar to Eqs. (A8) and (A9), except that the susceptibility χ is replaced by χ^{RPA} , given in Eq. (11). Note that, not only the usual particle-hole bubble and ladder contributions but the vertex corrections consisting of admixtures of the bubble and ladder vertices [66], all of which are summed to infinite order, are included, since the bare interaction is antisymmetrized.

APPENDIX B: SUPERCONDUCTING INSTABILITIES IN THE PRESENCE OF NN COULOMB REPULSION

In this Appendix, we explore the superconducting instabilities in the presence of the on-site Kanamori-Hubbard interaction, U , and NN Coulomb repulsion, V^{NN} . To deduce the general behavior, we perform calculations from weak to intermediate strength of U . The effects of $\eta_{B_{2g}}$ and longer-range anisotropies are neglected here.

For comparison, we first briefly summarize the results with U only [22,24,26,67]. It has been pointed out that the interplay of the bare- U interaction and fluctuations mediated interactions is nontrivial in determining the leading superconducting pairing within the RPA [22,67]. In a multiorbital model with SOC, the bare- U interaction is repulsive in the even-parity s' -, $d_{x^2-y^2}$ -, and d_{xy} -wave channels, but it does not affect g -wave or odd-parity pairings. On the other hand, fluctuation-induced interactions favor s' - and $d_{x^2-y^2}$ -wave pairings [22]. Thus, as U crosses from the weak- to the intermediate-coupling regime and the bare U becomes relatively less important, the dominant pairing changes from a helical to an s' - or $d_{x^2-y^2}$ -wave [22,26].

When V^{NN} is taken into account, it produces a correction, $\delta\Gamma(\mathbf{k}, \mathbf{k}')$, to the effective pairing interaction. At the bare- V^{NN} level, $\delta\Gamma^{(1)}(\mathbf{k}, \mathbf{k}')$ has the following schematic form:

$$\begin{aligned} \delta\Gamma^{(1)} &\sim V^{\text{NN}} [\cos(k_x - k'_x) + \cos(k_y - k'_y)] \mathcal{F}_{o \rightarrow b}(\mathbf{k}, \mathbf{k}') \\ &= \sum_{\Lambda} \sum_i g_{\Lambda, i}^{\text{NN}} [\phi^{\Lambda, i}(\mathbf{k})]^* \phi^{\Lambda, i}(\mathbf{k}'), \end{aligned} \quad (\text{B1})$$

where $\phi^{\Lambda, i}$ is the i th lattice harmonic of irrep. Λ in the D_{4h} group, with $g_{\Lambda, i}^{\text{NN}}$ the corresponding pairing interaction strength. Note that, in the presence of SOC, $\mathcal{F}_{o \rightarrow b}(\mathbf{k}, \mathbf{k}')$, the form factor associated with the orbital-to-band transformation, is in general a complex matrix in the pseudospin subspace (whose dependence is omitted here for a qualitative discussion). In the single-band Hubbard model, as discussed in Refs. [28,29], $\mathcal{F}_{o \rightarrow b}(\mathbf{k}, \mathbf{k}') = 1$; $g_{\Lambda, i}^{\text{NN}}$ is repulsive in the s -, $d_{x^2-y^2}$ -, and p -wave channels, while it is zero for both the d_{xy} - and g -wave channels. In the multiorbital case with a finite SOC, our numerical results show that $\delta\Gamma^{(1)}$ also contains small repulsive components in the d_{xy} - and g -wave channels, induced by the nontrivial form factor $\mathcal{F}_{o \rightarrow b}(\mathbf{k}, \mathbf{k}')$.

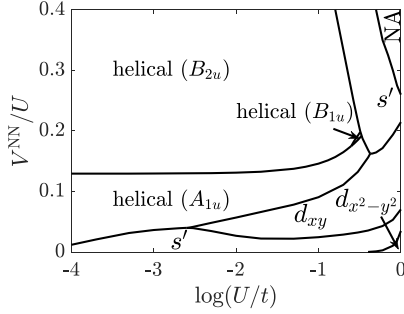


FIG. 7. Leading superconducting instability phase diagram as a function of $\log_{10}(U/t)$ and orbital-isotropic V^{NN} . “NA” corresponds to the regime where the RPA susceptibility diverges and where RPA breaks down. $\eta/t = 0.2$, $\eta_{B_{2g}}/\eta = 0$, and $J/U = 0.2$.

Higher-order contributions to $\delta\Gamma(\mathbf{k}, \mathbf{k}')$ due to V^{NN} are again induced by particle-hole fluctuations in spin, charge, and orbitals, and they can be either attractive or repulsive. They can make significant contributions to certain otherwise suppressed channels. For example, expanding the second-order correction term in the form of $V^{\text{NN}}(\mathbf{k}, \mathbf{k}')\tilde{\chi}(\mathbf{k}, \mathbf{k}')V^{\text{NN}}(\mathbf{k}, \mathbf{k}')$, where $\tilde{\chi}$ represents the bubble in Fig. 6(b), into different harmonic channels shows that this term has a substantial weight in the d_{xy} -wave channel.

Figure 7 shows the phase diagram for the leading superconducting instability as a function of the dimensionless interaction parameters U/t and V^{NN}/U . V^{NN} stabilizes the helical state in the weak- U regime and d_{xy} -wave pairing at intermediate U . As a result, TRSB $s' + id_{x^2-y^2}$, $s' + id_{xy}$, $d_{x^2-y^2} + id_{xy}$, mixed helical, or mixed parity $s' + ip$ pairing can be obtained at the phase boundaries. However, g -wave pairing is not favored. The phase diagram is roughly robust against the change of η and J/U . In the following, we discuss two limiting U cases in detail.

We first consider the weak- U limit and take $U/t = 10^{-4}$, where s' -wave is leading for $V^{\text{NN}} = 0$. The evolutions of the superconducting instabilities as a function of V^{NN} are shown in Fig. 8. The leading eigenvalue in all the pairing channels

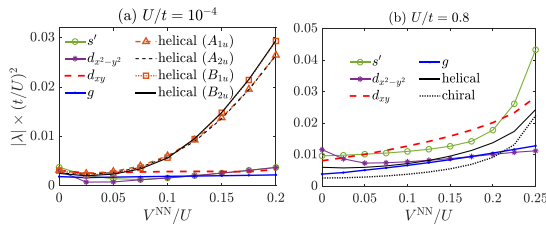


FIG. 8. Evolution of the largest eigenvalue (in magnitude) of the linearized gap equation, Eq. (16), in selected leading irrep. as a function of V^{NN}/U for (a) $U/t = 10^{-4}$ and (b) $U/t = 0.8$. (Some subleading irreps. are not shown.)

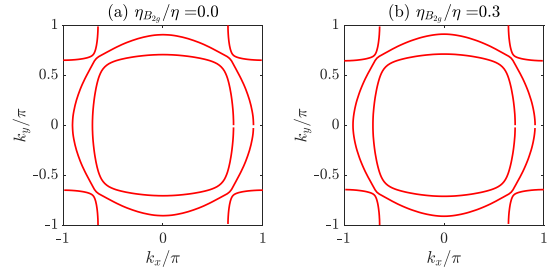


FIG. 9. Fermi surfaces for the tight-binding model given in Eq. (3) with SOC parameters: $(\eta, \eta_{B_{2g}}) =$ (a) $(0.2, 0)t$ and (b) $(0.154, 0.046)t$. $\tilde{\mu}_c$ is adjusted to 1.14*t* for (b).

shown is slightly suppressed at small V^{NN} ; helical pairings are promoted when $V^{\text{NN}}/U \gtrsim 0.05$. In the latter case, the corresponding helical gap functions we obtained are similar to those obtained in the absence of V^{NN} in the previous studies [21,22,61].

A noticeable feature in Fig. 8(a) is that, independent of V^{NN}/U , the splitting between helical pairings in the B_{1u} and B_{2u} (or A_{1u} and A_{2u}) irrep. is rather small, making it reasonable to consider accidentally degenerate helical pairings $B_{1u} + iB_{2u}$ (or $A_{1u} + iA_{2u}$). These pairings are proposed in Ref. [32] to explain some observations in SRO, including the intrinsic Hall and Kerr effects, the absence of observable spontaneous edge current, and the substantial Knight shift drop using simple gap functions without any microscopic details. We revisit the $B_{1u} + iB_{2u}$ state obtained at $V^{\text{NN}}/U = 0.15$ in Sec. IV to see if it can reconcile with the experiments.

Figure 8(b) shows an intermediate U case, $U/t = 0.8$, where $d_{x^2-y^2}$ is slightly leading without V^{NN} . The leading superconducting instabilities in most of the pairing channels, including g -wave, are enhanced, due to the enhancement of χ^{RPA} . Either the s' - or d_{xy} -solution dominates over other channels depending on the value of V^{NN} . Similar results were recently reported in Ref. [27], where $s' + id_{xy}$ pairing is proposed. We discuss the properties of the $s' + id_{xy}$ pairing at $V^{\text{NN}}/U = 0.05$ in Sec. IV.

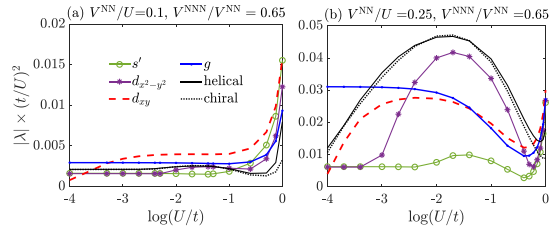


FIG. 10. Leading superconducting instabilities as a function of $\log(U/t)$ for (a) $V^{\text{NN}}/U = 0.1$, $V^{\text{NNN}}/V^{\text{NN}} = 0.65$ and (b) $V^{\text{NN}}/U = 0.25$, $V^{\text{NNN}}/V^{\text{NN}} = 0.65$.

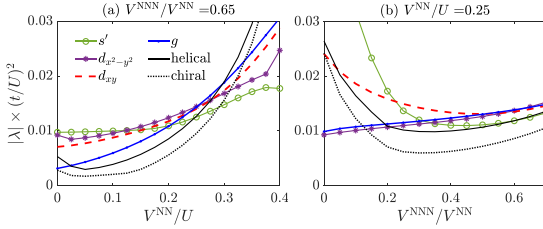


FIG. 11. Leading superconducting instabilities as (a) V^{NNN}/U and (b) $V^{\text{NNN}}/V^{\text{NN}}$ is varied. $\eta_{B_{2g}}/\eta = 0.3$. The case at $V^{\text{NN}}/U = 0.25$, $V^{\text{NNN}}/V^{\text{NN}} = 0.65$ is shown in Fig. 2(a).

APPENDIX C: STABILITY OF $d_{x^2-y^2}$ AND g -WAVE PAIRING IN THE PRESENCE OF LONGER-RANGE INTERACTIONS AND $\eta_{B_{2g}}$

In Sec. III, we show that both $d_{x^2-y^2}$ - and g -wave pairing can be stabilized at $\eta_{B_{2g}}/\eta \gtrsim 0.3$ in the intermediate U case ($U = 0.8$, $V^{\text{NN}}/U = 0.25$, $V^{\text{NNN}}/V^{\text{NN}} = 0.65$). [See Fig. 2(a).] In this Appendix, we show that this is a robust result relevant for a large region of parameter space. The resulting FSs for two distinct SOC parameter values are shown in Fig. 9. The orbital anisotropies, which can further promote the $d_{x^2-y^2}$ - and g -wave phase, are neglected here.

Before we focus on a detailed case, we first give a general picture of the evolutions of the g -wave superconducting instability for a wide range of U in the presence of sizable V^{NNN} (in Fig. 10). We find that g -wave pairing becomes dominant in the weak- U limit when longer-range interactions are included and is less favored for finite U , as observed in Fig. 1. However, the dependence of the leading pairing and of the g -wave state on U is nonmonotonic. Another important piece of information we can get from Fig. 10 is that, for a given U , the g -wave can always become the leading or the first subleading pairing in the parameter space of V^{NN} and V^{NNN} . For the latter case, it can be further promoted by the effects of $\eta_{B_{2g}}$ and interaction-anisotropies, as discussed in the main text.

We then consider the case at $\eta_{B_{2g}}/\eta = 0.3$ where the $d_{x^2-y^2}$ state is slightly dominant and the g -wave is the first subleading channel. As shown in Figs. 11 and 12, $d_{x^2-y^2}$ - and g -wave

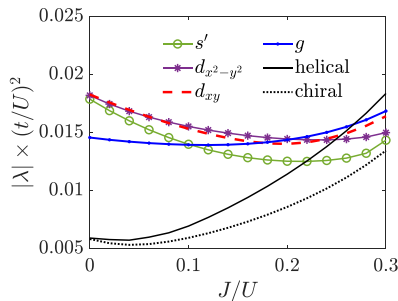


FIG. 12. Superconducting instabilities vs J/U in the $\eta_{B_{2g}}/\eta = 0.3$ case ($U/t = 0.8$, $V^{\text{NN}}/U = 0.25$, $V^{\text{NNN}}/V^{\text{NN}} = 0.65$).

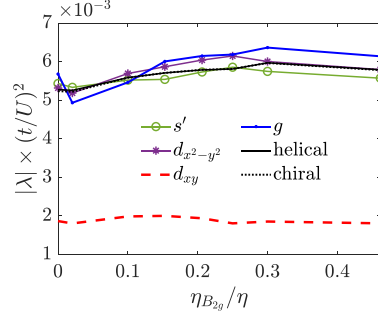


FIG. 13. Effects of $\eta_{B_{2g}}/\eta$ on the superconducting instabilities in different channels for $U/t = 0.0001$, $V^{\text{NN}}/U = 0.25$, $V^{\text{NNN}}/V^{\text{NN}} = 0.2$.

are the first two leading pairings in the range of $V^{\text{NN}}/U \in (0.2, 0.3)$, $V^{\text{NNN}}/V^{\text{NN}} > 0.5$, and $J/U \in (0.16, 0.24)$. The $d_{x^2-y^2}$ and g -wave phase can be larger by increasing $\eta_{B_{2g}}$ or including longer-range interaction anisotropies.

Figure 13 shows the effects of $\eta_{B_{2g}}/\eta$ in the weak- U case ($U/t = 10^{-4}$, $V^{\text{NN}}/U = 0.25$, $V^{\text{NNN}}/V^{\text{NN}} = 0.2$), where the g -wave is slightly dominant at $\eta_{B_{2g}}/\eta = 0$. We find that $d_{x^2-y^2}$ - and g -wave become the first two leading pairings at $\eta_{B_{2g}}/\eta \gtrsim 0.15$.

APPENDIX D: EFFECTS OF ORBITAL ANISOTROPIES OF THE LONGER-RANGE INTERACTIONS

Orbital anisotropies of the longer-range interactions can significantly impact the leading superconducting instabilities. In particular, they help to stabilize the g - and $d_{x^2-y^2}$ -wave state [in Fig. 2(b)]. In this Appendix, we show that anisotropy parameters α_{33} and β_{33} [defined in Eqs. (5) and (6)] are crucial to stabilizing the g - and $d_{x^2-y^2}$ -wave state, respectively. The effects of $\eta_{B_{2g}}$ are not included.

Rough estimates of the orbital-anisotropy parameters through integrals over Ru $4d-t_{2g}$ Slater-type orbitals are shown in Table I. The largest anisotropy parameter α_{33} ,

TABLE I. Effects of orbital-anisotropy parameters on different pairing channels (last six columns) for finite- U . \uparrow (\downarrow or $-$) means that the eigenvalue (magnitude) of that pairing channel is enhanced (suppressed or barely changed). $\uparrow\uparrow$ indicates that the eigenvalue of that channel is more enhanced than those with \uparrow . The second column gives the estimates of the parameters through integrals over Ru $4d-t_{2g}$ Slater-type orbitals.

Parameter	Estimate	Effects					
		s'	$d_{x^2-y^2}$	d_{xy}	g	helical	chiral
α_{33}	0.12	$\uparrow\uparrow$	$\uparrow\uparrow$	\uparrow	$\uparrow\uparrow$	$\uparrow\uparrow$	$\uparrow\uparrow$
$\alpha_{23,x}$	0.11	\uparrow	\uparrow	\uparrow	\uparrow	\uparrow	\uparrow
α_{12}	0.05	$-$	$-$	\downarrow	$-$	\uparrow	\uparrow
β_{33}	0.04	$\uparrow\uparrow$	$\uparrow\uparrow$	$-$	$-$	\uparrow	\uparrow
β_{13}	0.02	$-$	$-$	\uparrow	\uparrow	$\uparrow\uparrow$	$\uparrow\uparrow$
β_{12}	0.002	$-$	$-$	\uparrow	\uparrow	\uparrow	\uparrow

which quantifies the NN interactions for d_{xy} -orbitals (or d_{xz} -orbitals along the x -direction) relative to that for d_{yz} -orbitals along the y -direction, is about 0.12. As discussed in Sec. III, this value is underestimated because the hybridization effects are neglected. However, Table I can still indicate how those parameters compare with each other. For example, $(\alpha_{23,x}, \alpha_{12}, \beta_{33}, \beta_{13}, \beta_{12}) \approx (1, 0.4, 0.33, 0.17, 0)\alpha_{33}$, and this is the ratio used in the main text.

Table I shows the effects of the anisotropy parameters on different pairing channels for finite- U . See the caption for explanations of notation (arrows and dash). For example, α_{33} tends to significantly enhance all the pairing channels except d_{xy} . As a consequence, d_{xy} is surpassed by g -wave or helical at large α_{33} [shown in Fig. 14(a)]. In addition, β_{33} is critical to stabilizing $d_{x^2-y^2}$ -pairing. As shown in Fig. 14(b), $d_{x^2-y^2}$ -wave pairing is favored at $\beta_{33} > 0.7$. In the weak- U limit, the anisotropies tend to favor the g -wave state (not shown), because the enhancement effects on other pairing channels,

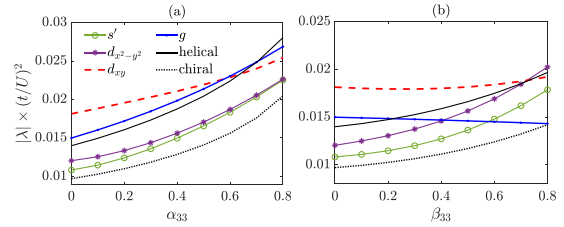


FIG. 14. Evolutions of the superconducting instability as a function of (a) α_{33} and (b) β_{33} . $U/t = 0.8$, $V^{\text{NN}}/U = 0.25$, $V^{\text{NNN}}/V^{\text{NN}} = 0.65$. Other anisotropy parameters are set to zero. $\alpha_{33}(\beta_{33}) = 0$ describes the orbital-isotropic case in Fig. 1.

as discussed above, are generally canceled out by the bare interactions.

- [1] G. M. Luke, Y. Fudamoto, K. M. Kojima, M. I. Larkin, J. Merrin, B. Nachumi, Y. J. Uemura, Y. Maeno, Z. Q. Mao, Y. Mori, H. Nakamura, and M. Sigrist, *Nature (London)* **394**, 558 (1998).
- [2] V. Grinenko, S. Ghosh, R. Sarkar, J.-C. Orain, A. Nikitin, M. Elender, D. Das, Z. Guguchia, F. Brückner, M. E. Barber *et al.*, *Nat. Phys.* **17**, 748 (2021).
- [3] J. Xia, Y. Maeno, P. T. Beyersdorf, M. M. Fejer, and A. Kapitulnik, *Phys. Rev. Lett.* **97**, 167002 (2006).
- [4] F. Kidwingira, J. D. Strand, D. J. Van Harlingen, and Y. Maeno, *Science* **314**, 1267 (2006).
- [5] S. Ghosh, A. Shekhter, F. Jerzembeck, N. Kikugawa, D. A. Sokolov, M. Brando, A. P. Mackenzie, C. W. Hicks, and B. J. Ramshaw, *Nat. Phys.* **17**, 199 (2021).
- [6] S. Benhabib, C. Lupien, I. Paul, L. Berges, M. Dion, M. Nardone, A. Zitouni, Z. Q. Mao, Y. Maeno, A. Georges, L. Taillefer, and C. Proust, *Nat. Phys.* **17**, 194 (2021).
- [7] S. Ghosh, T. G. Kiely, A. Shekhter, F. Jerzembeck, N. Kikugawa, D. A. Sokolov, A. P. Mackenzie, and B. J. Ramshaw, *Phys. Rev. B* **106**, 024520 (2022).
- [8] A. Pustogow, Y. Luo, A. Chronister, Y.-S. Su, D. A. Sokolov, F. Jerzembeck, A. P. Mackenzie, C. W. Hicks, N. Kikugawa, S. Raghu, E. D. Bauer, and S. E. Brown, *Nature (London)* **574**, 72 (2019).
- [9] K. Ishida, M. Manago, K. Kinjo, and Y. Maeno, *J. Phys. Soc. Jpn.* **89**, 034712 (2020).
- [10] E. Hassinger, P. Bourgeois-Hope, H. Taniguchi, S. René de Cotret, G. Grissonnanche, M. S. Anwar, Y. Maeno, N. Doiron-Leyraud, and L. Taillefer, *Phys. Rev. X* **7**, 011032 (2017).
- [11] R. Sharma, S. D. Edkins, Z. Wang, A. Kostin, C. Sow, Y. Maeno, A. P. Mackenzie, J. C. S. Davis, and V. Madhavan, *Proc. Natl. Acad. Sci. (USA)* **117**, 5222 (2020).
- [12] H. S. Røising, T. Scaffidi, F. Flicker, G. F. Lange, and S. H. Simon, *Phys. Rev. Res.* **1**, 033108 (2019).
- [13] A. T. Rømer, T. A. Maier, A. Kreisel, P. J. Hirschfeld, and B. M. Andersen, *Phys. Rev. Res.* **4**, 033011 (2022).
- [14] H. G. Suh, H. Menke, P. M. R. Brydon, C. Timm, A. Ramires, and D. F. Agterberg, *Phys. Rev. Res.* **2**, 032023(R) (2020).
- [15] J. Clepkens, A. W. Lindquist, X. Liu, and H.-Y. Kee, *Phys. Rev. B* **104**, 104512 (2021).
- [16] A. C. Yuan, E. Berg, and S. A. Kivelson, *Phys. Rev. B* **104**, 054518 (2021).
- [17] R. Willa, M. Hecker, R. M. Fernandes, and J. Schmalian, *Phys. Rev. B* **104**, 024511 (2021).
- [18] S. A. Kivelson, A. C. Yuan, B. Ramshaw, and R. Thomale, *npj Quantum Mater.* **5**, 43 (2020).
- [19] R. Willa, *Phys. Rev. B* **102**, 180503(R) (2020).
- [20] Q. H. Wang, C. Platt, Y. Yang, C. Honerkamp, F. C. Zhang, W. Hanke, T. M. Rice, and R. Thomale, *Europhys. Lett.* **104**, 17013 (2013).
- [21] T. Scaffidi, J. C. Romers, and S. H. Simon, *Phys. Rev. B* **89**, 220510(R) (2014).
- [22] L.-D. Zhang, W. Huang, F. Yang, and H. Yao, *Phys. Rev. B* **97**, 060510(R) (2018).
- [23] O. Gingras, R. Nourafkan, A. M. S. Tremblay, and M. Côté, *Phys. Rev. Lett.* **123**, 217005 (2019).
- [24] A. T. Rømer, D. D. Scherer, I. M. Eremin, P. J. Hirschfeld, and B. M. Andersen, *Phys. Rev. Lett.* **123**, 247001 (2019).
- [25] W.-S. Wang, C.-C. Zhang, F.-C. Zhang, and Q.-H. Wang, *Phys. Rev. Lett.* **122**, 027002 (2019).
- [26] Z. Wang, X. Wang, and C. Kallin, *Phys. Rev. B* **101**, 064507 (2020).
- [27] A. T. Rømer, P. J. Hirschfeld, and B. M. Andersen, *Phys. Rev. B* **104**, 064507 (2021).
- [28] S. Raghu, E. Berg, A. V. Chubukov, and S. A. Kivelson, *Phys. Rev. B* **85**, 024516 (2012).
- [29] S. Wolf, T. L. Schmidt, and S. Rachel, *Phys. Rev. B* **98**, 174515 (2018).
- [30] M. Roig, A. T. Rømer, A. Kreisel, P. J. Hirschfeld, and B. M. Andersen, *Phys. Rev. B* **106**, L100501 (2022).
- [31] A. T. Rømer, T. A. Maier, A. Kreisel, I. Eremin, P. J. Hirschfeld, and B. M. Andersen, *Phys. Rev. Res.* **2**, 013108 (2020).
- [32] W. Huang and Z. Wang, *Phys. Rev. Res.* **3**, L042002 (2021).

- [33] S. Käser, H. U. R. Strand, N. Wentzell, A. Georges, O. Parcollet, and P. Hansmann, *Phys. Rev. B* **105**, 155101 (2022).
- [34] A. Georges, L. d. Medici, and J. Mravlje, *Annu. Rev. Condens. Matter Phys.* **4**, 137 (2013).
- [35] G. Zhang, E. Gorelov, E. Sarvestani, and E. Pavarini, *Phys. Rev. Lett.* **116**, 106402 (2016).
- [36] J. Mravlje, M. Aichhorn, T. Miyake, K. Haule, G. Kotliar, and A. Georges, *Phys. Rev. Lett.* **106**, 096401 (2011).
- [37] S. Raghu, S. A. Kivelson, and D. J. Scalapino, *Phys. Rev. B* **81**, 224505 (2010).
- [38] W. Cho, R. Thomale, S. Raghu, and S. A. Kivelson, *Phys. Rev. B* **88**, 064505 (2013).
- [39] Z. V. Pchelkina, I. A. Nekrasov, T. Pruschke, A. Sekiyama, S. Suga, V. I. Anisimov, and D. Vollhardt, *Phys. Rev. B* **75**, 035122 (2007).
- [40] M. Hirayama, Y. Yamaji, T. Misawa, and M. Imada, *Phys. Rev. B* **98**, 134501 (2018).
- [41] P. E. Hoggan, M. B. Ruiz, and T. Özdoğan, *Quantum Frontiers of Atoms and Molecules* (Nova Science Publishers, 2011), pp. 64–90.
- [42] A. T. Rømer, A. Kreisel, I. Eremin, M. A. Malakhov, T. A. Maier, P. J. Hirschfeld, and B. M. Andersen, *Phys. Rev. B* **92**, 104505 (2015).
- [43] A. Tamai, M. Zingl, E. Rozbicki, E. Cappelli, S. Riccò, A. de la Torre, S. McKeown Walker, F. Y. Bruno, P. D. C. King, W. Meevasana, M. Shi, M. Radović, N. C. Plumb, A. S. Gibbs, A. P. Mackenzie, C. Berthod, H. U. R. Strand, M. Kim, A. Georges, and F. Baumberger, *Phys. Rev. X* **9**, 021048 (2019).
- [44] G.-Q. Liu, V. N. Antonov, O. Jepsen, and O. K. Andersen, *Phys. Rev. Lett.* **101**, 026408 (2008).
- [45] H. Isobe and N. Nagaosa, *Phys. Rev. B* **90**, 115122 (2014).
- [46] M. Kim, J. Mravlje, M. Ferrero, O. Parcollet, and A. Georges, *Phys. Rev. Lett.* **120**, 126401 (2018).
- [47] M. Hirayama, T. Misawa, T. Ohgoe, Y. Yamaji, and M. Imada, *Phys. Rev. B* **99**, 245155 (2019).
- [48] $|\Delta|_{\max(\min)}$ is the maximum (minimum) gap magnitude over all three bands.
- [49] C. Lupien, W. A. MacFarlane, C. Proust, L. Taillefer, Z. Q. Mao, and Y. Maeno, *Phys. Rev. Lett.* **86**, 5986 (2001).
- [50] A. J. Leggett, *Phys. Rev. Lett.* **14**, 536 (1965).
- [51] A. Chronister, A. Pustogow, N. Kikugawa, D. A. Sokolov, F. Jerzembeck, C. W. Hicks, A. P. Mackenzie, E. D. Bauer, and S. E. Brown, *Proc. Natl. Acad. Sci. USA* **118**, e2025313118 (2021).
- [52] T. Scaffidi and S. H. Simon, *Phys. Rev. Lett.* **115**, 087003 (2015).
- [53] J. R. Kirtley, C. Kallin, C. W. Hicks, E.-A. Kim, Y. Liu, K. A. Moler, Y. Maeno, and K. D. Nelson, *Phys. Rev. B* **76**, 014526 (2007).
- [54] C. W. Hicks, J. R. Kirtley, T. M. Lippman, N. C. Koshnick, M. E. Huber, Y. Maeno, W. M. Yuhasz, M. B. Maple, and K. A. Moler, *Phys. Rev. B* **81**, 214501 (2010).
- [55] P. J. Curran, S. J. Bending, W. M. Desoky, A. S. Gibbs, S. L. Lee, and A. P. Mackenzie, *Phys. Rev. B* **89**, 144504 (2014).
- [56] W. Huang, S. Lederer, E. Taylor, and C. Kallin, *Phys. Rev. B* **91**, 094507 (2015).
- [57] M. Stone and R. Roy, *Phys. Rev. B* **69**, 184511 (2004).
- [58] Y.-S. Li, N. Kikugawa, D. A. Sokolov, F. Jerzembeck, A. S. Gibbs, Y. Maeno, C. W. Hicks, J. Schmalian, M. Nicklas, and A. P. Mackenzie, *Proc. Natl. Acad. Sci. (USA)* **118**, e2020492118 (2021).
- [59] L. Vaugier, H. Jiang, and S. Biermann, *Phys. Rev. B* **86**, 165105 (2012).
- [60] M. Behrmann, C. Piefke, and F. Lechermann, *Phys. Rev. B* **86**, 045130 (2012).
- [61] M. Tsuchiizu, Y. Yamakawa, S. Onari, Y. Ohno, and H. Kontani, *Phys. Rev. B* **91**, 155103 (2015).
- [62] S.-O. Kaba and D. Sénéchal, *Phys. Rev. B* **100**, 214507 (2019).
- [63] A. Ramires and M. Sigrist, *Phys. Rev. B* **100**, 104501 (2019).
- [64] W. Huang, Y. Zhou, and H. Yao, *Phys. Rev. B* **100**, 134506 (2019).
- [65] SHARCNET: www.sharcnet.ca.
- [66] M. Altmeyer, D. Guterding, P. J. Hirschfeld, T. A. Maier, R. Valentí, and D. J. Scalapino, *Phys. Rev. B* **94**, 214515 (2016).
- [67] A. T. Rømer and B. M. Andersen, *Mod. Phys. Lett. B* **34**, 2040052 (2020).

Chapter 6

Conclusions

In this thesis, we have focused on the problems associated with unconventional superconductivity in SRO and related materials.

In Chap.3, we focused on an extraordinary class of unconventional superconductors: chiral superconductors. [25] In particular, we studied the spontaneous edge current in chiral d - and f -wave superconductors. While it had previously been shown that in the absence of Meissner screening, these currents vanish in the continuum limit at zero temperature, [68, 69] we showed that in general (at finite temperature and/or beyond the continuum limit) the edge currents are non-vanishing but tiny in comparison to that in the analogous chiral p -wave case. We also found that, as in the chiral p -wave case, [78, 79] the magnitude of the edge currents in chiral f -wave superconductors is suppressed by surface roughness. In this regard, the chiral d -wave superconductor is special. In chiral d -wave, surface roughness can either reverse the direction of the current flow or, like the p - (f -) wave case, reduce the magnitude of the current density, depending on the microscopic details, such as the edge orientation, the band structure, and the strength of the surface roughness. These results are important for experimental studies on materials that support higher chirality superconductivity, such as SrAsPt, doped Graphene, and UPt₃. [63, 64, 25]

In Chap.4 and Chap.5, we delved into the pairing mechanism and pairing symmetry in SRO. The effect of atomic SOC on different triplet p -wave channels is discussed in Chap.4. In this study, we first presented a complete Ginzburg Landau free energy analysis of the SOC effect for a general multi-band model (both 2D

and 3D). Then we studied the case of SRO, combining a symmetry analysis with numerical weak-coupling RG and RPA calculations. We found that the splitting among the p -wave pairings depends on not only the presence of SOC, but also other ingredients of the microscopic Hamiltonian. In general, chiral p -wave pairing is difficult to stabilize in SRO. Moreover, helical pairing, nodal s' - or $d_{x^2-y^2}$ pairing can be obtained depending on the details of the interactions.

Lastly, we studied the superconducting instabilities in SRO in the presence of non-local interactions and non-local SOC in Chap.5. One focus of this work is identifying the effects that stabilize $d_{x^2-y^2} + ig_{xy(x^2-y^2)}$ pairing in SRO models. We found that both $d_{x^2-y^2}$ - and g -wave pairing are obtained in the presence of sizable NNN interaction with orbital anisotropy of the longer-range interactions or with B_{2g} channel SOC or both. As a result, an accidentally degenerate or near degenerate $d_{x^2-y^2} + ig$ state can be stable in specific parameter spaces. We also showed that the $d_{x^2-y^2} + ig$ pairing is better in explaining the existence of nodes/near-nodes and the absence of spontaneous edge current than the $s' + id_{xy}$ and mixed helical pairing proposals.

The RPA formalism we employed in this thesis is limited to small values of the Coulomb interaction, $U \lesssim \mathcal{O}(t)$. In most real materials structurally similar to SRO, typical estimates of U fall in the $\mathcal{O}(eV)$ range, i.e. $U \sim 10t$. In addition, the RPA formalism neglects correlations away from the FS and many diagrams in calculating the effective interaction. These effects can have a significant impact beyond the weak coupling limit. For example, the $d_{x^2-y^2}$ pairing may be discounted, if the effect of the van Hove singularity close to the FS of the γ band is not adequately taken into account. A recent study [141] compares the weak coupling RG, RPA, and dynamical cluster approximation (DCA) approaches within the single band Hubbard model and finds good agreement among these approaches, in the region where they can be compared, suggesting a smooth crossover in pairing states within the Hubbard model from weak to strong coupling. Thus, it is reasonable to expect the RPA approach to provide valuable insight into superconducting pairings in SRO. Nevertheless, in light of the multi-band nature of SRO, it would be of interest to study the stability of the $d_{x^2-y^2} + ig_{xy(x^2-y^2)}$ pairing state using functional RG [120, 142], since it can be employed in the sizable U -regime and it

treats states away from the FS more accurately.

The superconducting pairings discussed in this thesis are considered as an instability of the FS and are classified according to the irreps. of the point group of the lattice in the band basis. In the presence of SOC or other orbital mixing hybridizations, the orbital and spin characteristics of a pairing are complicated. Therefore, it was suggested that the above analysis of the pairing function labelled by band indices is insufficient. An extended classification of the allowed order parameters in the orbital basis has been introduced in recent studies. [143, 144, 145, 28] Multiple inter-orbital pairings have been proposed based on orbital basis approaches. [146, 140, 98] When transformed into the band basis, all these pairings support sizable interband pairing, which has been ignored in our studies.

Since the interorbital coupling terms that give rise to the band structure near the Fermi energy is much larger than the superconducting pairing energy in SRO, one might expect interband pairing to be small compared to intraband pairing. Also, interband pairing is not expected to significantly impact the relative stability of different pairing states close to T_c , as it does not open up a gap on the FS. However, the interband pairing can be important for some properties, including the polar Kerr effect [35], which has been measured at high frequencies where all superconducting contributions are of order $(\Delta/E_F)^2$ or smaller. Thus, it is interesting to address the relative size of intraband and interband pairing in SRO.

This issue can be addressed in the current RPA formalism by including effective interaction terms, such as $V_{abab}^{\text{eff}} c_{a,\mathbf{k}}^\dagger c_{b,-\mathbf{k}}^\dagger c_{b,-\mathbf{q}} c_{a,\mathbf{q}}$, where $a \neq b$ are band indices and \mathbf{k} and \mathbf{q} are electron wavevectors in the BZ, instead of being constrained on the FSs. These effective interaction terms can give rise to interband pairings. Thus, one can calculate intra- and inter-band pairings by solving the linearized gap equation. This would be a significantly larger numerical calculation because of the removal of the restriction to momenta on the FS, but it would be an exciting avenue for future work.

Appendix A

Quasiclassical Eilenberger theory

In Chapter 3, we studied the spontaneous edge currents in higher chirality superconductors using the quasiclassical Eilenberger formalism. This approach, developed by Schopohl, *et al* [133], has been applied to the vortex [133, 134, 135, 136] and the boundary problems. [75, 74] Here we give a brief description of this framework. For more details, one can refer to Refs. [147, 148, 149].

The chiral superconducting OP is described by,

$$\hat{\Delta}(\mathbf{r}, \mathbf{r}') = \begin{cases} \Delta(\mathbf{r}, \mathbf{r}') i\hat{\sigma}_y & \text{for a spin-singlet chiral pairing,} \\ (\Delta(\mathbf{r}, \mathbf{r}')\hat{\sigma}_z) i\hat{\sigma}_y & \text{for a spin-triplet chiral pairing,} \end{cases} \quad (\text{A.1})$$

where $\hat{\sigma}$ is the Pauli spin matrix. $\Delta(\mathbf{r}, \mathbf{r}')$ describes the orbital part of the superconducting gap function, which for a translationally invariant system would be a function of $\mathbf{r} - \mathbf{r}'$ only.

The Bogoliubov-de Gennes equations that describe the inhomogeneous states can be expressed in a 2×2 matrix form as,

$$\int d\mathbf{r}' \begin{pmatrix} \delta(\mathbf{r} - \mathbf{r}') H(\mathbf{r}') & \Delta(\mathbf{r}, \mathbf{r}') \\ (-1)^S \Delta^*(\mathbf{r}, \mathbf{r}') & -\delta(\mathbf{r} - \mathbf{r}') H^*(\mathbf{r}') \end{pmatrix} \begin{pmatrix} u_\alpha(\mathbf{r}') \\ v_\alpha(\mathbf{r}') \end{pmatrix} = E_\alpha \begin{pmatrix} u_\alpha(\mathbf{r}) \\ v_\alpha(\mathbf{r}) \end{pmatrix}. \quad (\text{A.2})$$

Here, $u_\alpha(\mathbf{r})$ and $v_\alpha(\mathbf{r})$ are the quasiparticle and quasihole wave functions. $H(\mathbf{r}) = [-i\nabla + e\mathbf{A}(\mathbf{r})]^2/2m - \mu$ is the kinetic energy of an electron. e is the electron charge and \mathbf{A} is the vector potential. S is the spin angular momentum. For convenience,

the Planck constant, \hbar , the Boltzmann constant, k_B , and the speed of light, c , are all taken to be unity.

Eq. A.2 is associated with two characteristic length scales: the Fermi wavelength, \mathbf{k}_F^{-1} , and the coherence length of the Cooper pairs, $\xi \sim \hbar \mathbf{v}_F / \Delta$. Δ is the bulk superconducting gap, and \mathbf{v}_F is the Fermi velocity. Since the self-consistent pair potential varies only on the scale of ξ , where $\xi \gg \mathbf{k}_F^{-1}$, one can apply the Andreev approximation, i.e. factoring the fast and slow spatial variations, as [150, 151]

$$\begin{pmatrix} u_\alpha(\mathbf{r}) \\ v_\alpha(\mathbf{r}) \end{pmatrix} = \begin{pmatrix} \bar{u}_\alpha(\mathbf{k}_F, \mathbf{r}) \\ \bar{v}_\alpha(\mathbf{k}_F, \mathbf{r}) \end{pmatrix} e^{i\mathbf{k}_F \cdot \mathbf{r}}, \quad (\text{A.3})$$

Retaining leading-order terms in $k_F \xi_0$, we obtain,

$$\begin{pmatrix} -i\mathbf{v}_F \cdot \nabla + e\mathbf{v}_F \cdot \mathbf{A}(\mathbf{r}) & \Delta(\mathbf{k}_F, \mathbf{r}) \\ -\Delta^*(\mathbf{k}_F, \mathbf{r}) & i\mathbf{v}_F \cdot \nabla + e\mathbf{v}_F \cdot \mathbf{A}(\mathbf{r}) \end{pmatrix} \psi_\alpha(\mathbf{k}_F, \mathbf{r}) = E_\alpha \psi_\alpha(\mathbf{k}_F, \mathbf{r}), \quad (\text{A.4})$$

where, $\psi_\alpha(\mathbf{k}_F, \mathbf{r}) = \begin{pmatrix} \bar{u}_\alpha(\mathbf{k}_F, \mathbf{r}) \\ \bar{v}_\alpha(\mathbf{k}_F, \mathbf{r}) \end{pmatrix}$. Eq.(A.4) is the same for both singlet and triplet pairings, since $\Delta(-\mathbf{k}_F, \mathbf{r}) = -\Delta(\mathbf{k}_F, \mathbf{r})$ for triplet pairings, while $\Delta(-\mathbf{k}_F, \mathbf{r}) = \Delta(\mathbf{k}_F, \mathbf{r})$ for singlet pairings.

The corresponding Eilenberger transport equation is,

$$i\mathbf{v}_F \cdot \nabla \hat{g}(\mathbf{k}_F, \omega_n, \mathbf{r}) + \left[\begin{pmatrix} i\omega_n - e\mathbf{v}_F \cdot \mathbf{A}(\mathbf{r}) & -\Delta(\mathbf{k}_F, \mathbf{r}) \\ \Delta^*(\mathbf{k}_F, \mathbf{r}) & -i\omega_n + e\mathbf{v}_F \cdot \mathbf{A}(\mathbf{r}) \end{pmatrix}, \hat{g}(\mathbf{k}_F, \omega_n, \mathbf{r}) \right] = 0, \quad (\text{A.5})$$

where the quasi-classical Green function is defined as,

$$\hat{g}(\mathbf{k}_F, \omega_n, \mathbf{r}) = \begin{pmatrix} g(\mathbf{k}_F, \omega_n, \mathbf{r}) & if(\mathbf{k}_F, \omega_n, \mathbf{r}) \\ -i\bar{f}(\mathbf{k}_F, \omega_n, \mathbf{r}) & -g(\mathbf{k}_F, \omega_n, \mathbf{r}) \end{pmatrix}. \quad (\text{A.6})$$

$\omega_n = (2n + 1)\pi T$ is the Matsubara frequency with n being an integer. g and f are the normal and anomalous parts of the quasi-classical Green function, respectively,

satisfying the normalization relation: $g^2(\mathbf{k}_F, \omega_n, \mathbf{r}) + f(\mathbf{k}_F, \omega_n, \mathbf{r}) \bar{f}(\mathbf{k}_F, \omega_n, \mathbf{r}) = 1$.

The Eilenberger equation, Eq.(A.5), is difficult to solve directly, as g , f , and f^\dagger are coupled with each other. However, the equation can be decoupled into two scalar Riccati-type differential equations using the Riccati parametrization. (For more details, refer to Ref. [152].) The Riccati equations can be calculated self-consistently using initial conditions, boundary conditions, superconducting gap equations, and Maxwell equations. For more details, one can refer to [75, 153].

Appendix B

Ginzburg-Landau analysis of the SOC effect on triplet p -wave pairings

In Chap.4, we show that SOC can induce five Ginzburg-Landau (GL) terms at quadratic order in the order parameter for triplet p -wave states of a 2D model. Here we provide details of the derivations.

A1 GL free energy in the absence of SOC

In general, the triplet superconducting OP can be written in the following form,

$$\hat{\Delta}(\mathbf{k}) \equiv \sum_{\mu=\{x,y,z\}} \sum_{j=\{x,y\}} d_j^\mu \sigma_\mu i \sigma_2 \psi_j(\mathbf{k}) \quad (\text{B.1})$$

$$= \sum_{j=\{x,y\}} \hat{\Delta}_j \psi_j(\mathbf{k}), \quad (\text{B.2})$$

where σ is Pauli matrix; $\psi_j(\mathbf{k})$ are two basis functions in \mathbf{k} -space that transform like k_x and k_y under the D_{4h} point group. $\hat{\Delta}_j$ is defined as [7]

$$\hat{\Delta}_j = \begin{pmatrix} \Delta_{\uparrow\uparrow,j} & \Delta_{\uparrow\downarrow,j} \\ \Delta_{\downarrow\uparrow,j} & \Delta_{\downarrow\downarrow,j} \end{pmatrix}. \quad (\text{B.3})$$

In the absence of SOC, the GL free energy is invariant under the D_{4h} point group and $SU(2)$ spin rotation. Rotational invariance in spin space implies that only products terms of the type $(\hat{\Delta}\hat{\Delta}^\dagger)^n$ can appear in the GL free energy expansion [7]:

$$f_2^0 = \alpha(T - T_c^0) \frac{1}{2} \text{Tr}[\hat{\Delta}^\dagger \hat{\Delta}] \quad (\text{B.4})$$

$$= \alpha(T - T_c^0) \frac{1}{2} \text{Tr}[\hat{\Delta}_x^\dagger \hat{\Delta}_x + \hat{\Delta}_y^\dagger \hat{\Delta}_y] \quad (\text{B.5})$$

$$= \alpha(T - T_c^0) \frac{1}{2} \sum_{j=\{x,y\}} \left(|\Delta_{\uparrow\uparrow,j}|^2 + |\Delta_{\downarrow\downarrow,j}|^2 + |\Delta_{\uparrow\downarrow,j}|^2 + |\Delta_{\downarrow\uparrow,j}|^2 \right) \quad (\text{B.6})$$

$$= \alpha(T - T_c^0) \sum_{\mu=\{x,y,z\}} \sum_{j=\{x,y\}} |d_j^\mu|^2. \quad (\text{B.7})$$

Where the superscript “0” indicates quantities defined for zero SOC, and the subscript “2” denotes the order of terms in $\hat{\Delta}$. The trace, $\text{Tr}[\dots]$, is taken over the spin space.

Following Ref. [13, 154], the GL free energy at fourth-order in $\hat{\Delta}$ is,

$$f_4^0 = \frac{\beta_1}{4} \left\{ \text{Tr}[\hat{\Delta}_x^\dagger \hat{\Delta}_x + \hat{\Delta}_y^\dagger \hat{\Delta}_y] \right\}^2 + \frac{\beta_2}{4} \left\{ \text{Tr}[\hat{\Delta}_x \hat{\Delta}_y^\dagger - \hat{\Delta}_x^\dagger \hat{\Delta}_y] \right\}^2 + \frac{\beta_3}{2} \text{Tr}[\hat{\Delta}_x \hat{\Delta}_x^\dagger] \text{Tr}[\hat{\Delta}_y^\dagger \hat{\Delta}_y]. \quad (\text{B.8})$$

Note that the fourth-order terms are different from those for ^3He . [7] This is because the model we consider for SRO is 2D with D_{4h} symmetry; while ^3He is 3D with $SO(2)$ symmetry. [155]

A2 SOC induced GL free energy terms

The presence of SOC generally breaks both the full pseudospin $SU(2)$ rotation and spatial D_{4h} symmetries, so that the GL free energy is only invariant under a simultaneous rotation in both spin and spatial spaces. This leads to additional terms in the GL free energy. To write down all possible SOC-induced GL free energy terms at second order in $\hat{\Delta}$, we start with the following quadratic term,

$$f_{ij}^{\mu\nu} = (d_i^\mu)^* d_j^\nu, \quad (\text{B.9})$$

which is a rank-4 tensor. $\{i, j\} = \{1, 2\}$ for spatial indices and $\{\mu, \nu\} = \{1, 2, 3\}$ for spin.

The remaining symmetry of $f_{ij}^{\mu\nu}$ in the presence of SOC is $D_{4h}^{\hat{L}+\hat{S}} \otimes U(1)^C \otimes \mathcal{M}_{xy}^{\hat{S}}$. $D_{4h}^{\hat{L}+\hat{S}}$ is the D_{4h} point group whose symmetry operations act simultaneously on the spatial \mathbf{k} and pseudospin spaces, $U(1)^C$ is the charge $U(1)$ gauge symmetry, and $\mathcal{M}_{xy}^{\hat{S}}$ is the xy -plane mirror reflection in the pseudospin space. In order for $f_{ij}^{\mu\nu}$ to be invariant under symmetry operations of the above group, we need to contract $f_{ij}^{\mu\nu}$ to a scalar.

The mirror reflection symmetry $\mathcal{M}_{xy}^{\hat{S}}$ requires that $\{\mu, \nu\} = \{x, y\}$ or $\mu = \nu = z$. For $\{\mu, \nu\} = \{x, y\}$, the possible contractions are,

$$\sum_{\mu\nu} \sum_{ij} \delta_{\mu i} \delta_{\nu j} f_{ij}^{\mu\nu} = \sum_{i,j=\{x,y\}} (d_i^i)^* d_j^j = |d_x^x|^2 + |d_y^y|^2 + (d_x^x)^* d_y^y + (d_y^y)^* d_x^x, \quad (\text{B.10a})$$

$$\sum_{\mu\nu} \sum_{ij} \delta_{\mu j} \delta_{\nu i} f_{ij}^{\mu\nu} = \sum_{i,j=\{x,y\}} (d_i^j)^* d_j^i = |d_x^x|^2 + |d_y^y|^2 + (d_x^y)^* d_y^x + (d_y^x)^* d_x^y, \quad (\text{B.10b})$$

$$\sum_{\mu\nu} \sum_{ij} \delta_{\mu\nu} \delta_{ij} f_{ij}^{\mu\nu} = \sum_{i,j=\{x,y\}} (d_i^j)^* d_i^j = |d_x^x|^2 + |d_y^y|^2 + |d_x^y|^2 + |d_y^x|^2, \quad (\text{B.10c})$$

$$\sum_{\mu\nu} \sum_{ij} \delta_{\mu i} \delta_{ij} \delta_{j\nu} f_{ij}^{\mu\nu} = |d_x^x|^2 + |d_y^y|^2. \quad (\text{B.10d})$$

For $\mu = \nu = z$, there is only one possible contraction,

$$\sum_{i,j=\{1,2\}} \delta_{ij} f_{ij}^{zz} = |d_x^z|^2 + |d_y^z|^2. \quad (\text{B.11})$$

We can get the five SOC-induced GL free energy terms shown in Table 1 of Chap. 4, by combining Eq. (B.10) and Eq. (B.11)

We can also write these terms in terms of $\hat{\Delta}$. In the absence of SOC, only $(\hat{\Delta}^\dagger \hat{\Delta})^n$ terms can appear in the GL free energy expansion; $\text{Tr}\{\hat{\Delta}_i^\dagger \sigma_j \hat{\Delta}_k\}$ and $\text{Tr}\{\hat{\Delta}_i^\dagger \sigma_j \hat{\Delta}_k \sigma_\ell\}$ terms, with $\{j, \ell\} \neq 0$ can appear with SOC. The five free energy

terms can be rewritten as,

$$f_2^{SOC,1} = \frac{1}{4} \sum_{i=1,2} \left\{ \text{Tr}\{\hat{\Delta}_i^\dagger \sigma_1 \hat{\Delta}_i \sigma_1\} - \text{Tr}\{\hat{\Delta}_i^\dagger \sigma_2 \hat{\Delta}_i \sigma_2\} \right\} \quad (\text{B.12})$$

$$f_2^{SOC,2} = \frac{1}{4} \left\{ \left[\text{Tr}[\hat{\Delta}_1^\dagger \sigma_1 \hat{\Delta}_2 \sigma_2] + \text{Tr}[\hat{\Delta}_2^\dagger \sigma_1 \hat{\Delta}_1 \sigma_2] \right] + i \left[\epsilon_{ij} \text{Tr}\{\hat{\Delta}_i^\dagger \sigma_3 \hat{\Delta}_j\} - c.c. \right] \right\}, \quad (\text{B.13})$$

$$f_2^{SOC,3} = \frac{1}{4} \left\{ \left[\text{Tr}[\hat{\Delta}_1^\dagger \sigma_1 \hat{\Delta}_2 \sigma_2] + \text{Tr}[\hat{\Delta}_2^\dagger \sigma_1 \hat{\Delta}_1 \sigma_2] \right] - i \left[\epsilon_{ij} \text{Tr}\{\hat{\Delta}_i^\dagger \sigma_3 \hat{\Delta}_j\} - c.c. \right] \right\}, \quad (\text{B.14})$$

$$\begin{aligned} f_2^{SOC,4} = & \frac{1}{8} \left\{ 2 \left\{ \text{Tr}\{\hat{\Delta}_1^\dagger \sigma_3 \hat{\Delta}_1 \sigma_3\} + \text{Tr}\{\hat{\Delta}_2^\dagger \sigma_3 \hat{\Delta}_2 \sigma_3\} \right\} \right. \\ & \left. + \text{Tr}\{\hat{\Delta}_2^\dagger \sigma_1 \hat{\Delta}_2 \sigma_1\} + \text{Tr}\{\hat{\Delta}_2^\dagger \sigma_2 \hat{\Delta}_2 \sigma_2\} - \text{Tr}\{\hat{\Delta}_1^\dagger \sigma_1 \hat{\Delta}_1 \sigma_1\} - \text{Tr}\{\hat{\Delta}_1^\dagger \sigma_2 \hat{\Delta}_1 \sigma_2\} \right\} \end{aligned} \quad (\text{B.15})$$

$$\begin{aligned} f_2^{SOC,5} = & \frac{1}{8} \left\{ 2 \left\{ \text{Tr}\{\hat{\Delta}_1^\dagger \sigma_3 \hat{\Delta}_1 \sigma_3\} + \text{Tr}\{\hat{\Delta}_2^\dagger \sigma_3 \hat{\Delta}_2 \sigma_3\} \right\} \right. \\ & \left. + \text{Tr}\{\hat{\Delta}_1^\dagger \sigma_1 \hat{\Delta}_1 \sigma_1\} + \text{Tr}\{\hat{\Delta}_1^\dagger \sigma_2 \hat{\Delta}_1 \sigma_2\} - \text{Tr}\{\hat{\Delta}_2^\dagger \sigma_1 \hat{\Delta}_2 \sigma_1\} - \text{Tr}\{\hat{\Delta}_2^\dagger \sigma_2 \hat{\Delta}_2 \sigma_2\} \right\}. \end{aligned} \quad (\text{B.16})$$

Appendix C

RPA effective interaction in the presence of both local and longer-range interactions

In Chap. 4 and Chap. 5, we study the superconducting instabilities in SRO models within RPA, where the effective pairing vertex is calculated by summing up infinite orders of diagrams of bubble and ladder topology. This approach has been successfully applied to different multi-orbital systems in the presence of local interactions, such as iron-based superconductors [156], and SRO [106, 107]. In this appendix, we present a detailed derivation of the RPA effective interaction in the presence of longer-range interactions, as given in Chap.5.

A1 Coulomb interactions

The bare interaction Hamiltonian is defined in Eq. 4 of Chap. 5 and can be rewritten in a more compact form as,

$$H_{\text{int}} = \frac{1}{4} \sum_{i, \delta, \tilde{a}_j} \left([W_1(\delta)]_{\tilde{a}_3 \tilde{a}_2}^{\tilde{a}_1 \tilde{a}_4} c_{i, \tilde{a}_1}^\dagger c_{i+\delta, \tilde{a}_3}^\dagger c_{i+\delta, \tilde{a}_4} c_{i, \tilde{a}_2} + [W_2(\delta)]_{\tilde{a}_3 \tilde{a}_2}^{\tilde{a}_1 \tilde{a}_4} c_{i, \tilde{a}_1}^\dagger c_{i+\delta, \tilde{a}_3}^\dagger c_{i, \tilde{a}_4} c_{i+\delta, \tilde{a}_2} \right). \quad (\text{C.1})$$

$\tilde{a}_j = \{a_j, s_j\}$ is a composite index that labels both orbital (a_j) and spin (s_j). $\delta = \{0, \hat{x}, \hat{y}, -\hat{x}, -\hat{y}, \hat{x} + \hat{y}, -\hat{x} + \hat{y}, -\hat{x} - \hat{y}, \hat{x} - \hat{y}\}$ for the lattice vector between

sites. $[W_1(\delta)]_{\tilde{a}_3\tilde{a}_4}^{\tilde{a}_1\tilde{a}_2}$ and its symmetry-related partner $[W_2(\delta)]_{\tilde{a}_3\tilde{a}_4}^{\tilde{a}_1\tilde{a}_2}$ are block diagonal matrix with 36×36 sub-matrix for each value of δ , with the following non-zero elements,

$$[W_1(\delta = 0)]_{a_3\bar{s}, a_2\bar{s}}^{a_1s, a_4\bar{s}} = \begin{cases} U, & a_1 = a_2 = a_3 = a_4; \\ U', & a_1 = a_2 \neq a_3 = a_4; \\ J', & a_1 = a_3 \neq a_2 = a_4; \\ J, & a_1 = a_4 \neq a_2 = a_3; \end{cases} \quad (\text{C.2a})$$

$$[W_1(\delta = 0)]_{a_3\bar{s}, a_2\bar{s}}^{a_1s, a_4s} = U' - J, \quad a_1 = a_2 \neq a_3 = a_4; \quad (\text{C.2b})$$

$$[W_2(\delta = 0)]_{a_3\bar{s}, a_2\bar{s}}^{a_1s, a_4s} = \begin{cases} -U, & a_1 = a_2 = a_3 = a_4; \\ -J, & a_1 = a_2 \neq a_3 = a_4; \\ -J', & a_1 = a_3 \neq a_2 = a_4; \\ -U', & a_1 = a_4 \neq a_2 = a_3; \end{cases} \quad (\text{C.2c})$$

$$[W_2(\delta = 0)]_{a_3s, a_2s}^{a_1s, a_4s} = -U' + J, \quad a_1 = a_4 \neq a_2 = a_3; \quad (\text{C.2d})$$

$$[W_1(\delta \neq 0)]_{a_3\bar{s}, a_2\bar{s}}^{a_1s, a_4\bar{s}} = \begin{cases} V_{a_1a_1, \delta}, & a_1 = a_2 = a_3 = a_4; \\ V_{a_1a_3, \delta}, & a_1 = a_2 \neq a_3 = a_4; \end{cases} \quad (\text{C.3a})$$

$$[W_1(\delta \neq 0)]_{a_3s, a_2s}^{a_1s, a_4s} = \begin{cases} V_{a_1a_1, \delta}, & a_1 = a_2 = a_3 = a_4; \\ V_{a_1a_3, \delta}, & a_1 = a_2 \neq a_3 = a_4; \end{cases} \quad (\text{C.3b})$$

$$[W_2(\delta \neq 0)]_{a_3\bar{s}, a_2\bar{s}}^{a_1s, a_4s} = \begin{cases} -V_{a_1a_1, \delta}, & a_1 = a_2 = a_3 = a_4; \\ -V_{a_1a_3, \delta}, & a_1 = a_4 \neq a_2 = a_3; \end{cases} \quad (\text{C.3c})$$

$$[W_2(\delta \neq 0)]_{a_3s, a_2s}^{a_1s, a_4s} = \begin{cases} -V_{a_1a_1, \delta}, & a_1 = a_4 = a_2 = a_3; \\ -V_{a_1a_3, \delta}, & a_1 = a_4 \neq a_2 = a_3, \end{cases} \quad (\text{C.3d})$$

where $\bar{s} = -s$.

By Fourier transformation of the interaction, we get,

$$H_{\text{int}} = \frac{1}{4} \sum_{\delta} \sum_{\mathbf{k}_i, \tilde{a}_i} [W(\mathbf{k}_1, \mathbf{k}_2; \mathbf{k}_3, \mathbf{k}_4, \delta)]_{\tilde{a}_3\tilde{a}_2}^{\tilde{a}_1\tilde{a}_4} c_{\mathbf{k}_1, \tilde{a}_1}^{\dagger} c_{\mathbf{k}_3, \tilde{a}_3}^{\dagger} c_{\mathbf{k}_4, \tilde{a}_4} c_{\mathbf{k}_2, \tilde{a}_2}. \quad (\text{C.4})$$

The interaction matrix, $[W(\mathbf{k}_1, \mathbf{k}_2; \mathbf{k}_3, \mathbf{k}_4, \delta)]_{\tilde{a}_3 \tilde{a}_2}^{\tilde{a}_1 \tilde{a}_4}$, is defined as,

$$[W(\mathbf{k}_1, \mathbf{k}_2; \mathbf{k}_3, \mathbf{k}_4, \delta)]_{\tilde{a}_3 \tilde{a}_2}^{\tilde{a}_1 \tilde{a}_4} = e^{i(\mathbf{k}_1 - \mathbf{k}_2) \cdot \delta} [W_1(\delta)]_{\tilde{a}_3 \tilde{a}_2}^{\tilde{a}_1 \tilde{a}_4} + e^{i(\mathbf{k}_1 - \mathbf{k}_4) \cdot \delta} [W_2(\delta)]_{\tilde{a}_3 \tilde{a}_2}^{\tilde{a}_1 \tilde{a}_4} \quad (\text{C.5})$$

$$= \sum_{l,m=\{1,2\}} \left[\begin{array}{c} \left(\begin{array}{cc} e^{i\mathbf{k}_1 \cdot \delta} & 0 \\ 0 & e^{i\mathbf{k}_1 \cdot \delta} \end{array} \right) \underbrace{\left(\begin{array}{cc} [W_1(\delta)]_{\tilde{a}_3 \tilde{a}_2}^{\tilde{a}_1 \tilde{a}_4} & 0 \\ 0 & [W_2(\delta)]_{\tilde{a}_3 \tilde{a}_2}^{\tilde{a}_1 \tilde{a}_4} \end{array} \right)}_{[\tilde{W}(\delta)]_{\tilde{a}_3 \tilde{a}_2}^{\tilde{a}_1 \tilde{a}_4}} \left(\begin{array}{cc} e^{-i\mathbf{k}_2 \cdot \delta} & 0 \\ 0 & e^{-i\mathbf{k}_4 \cdot \delta} \end{array} \right) \\ \left. \vphantom{\sum} \right]_{lm} \quad (\text{C.6})$$

The sum is taken over all the matrix elements in a 2×2 subspace that we have introduced to factorize out the momenta dependence of the bare interaction, associated with momentum transfer $\mathbf{q} = \mathbf{k}_1 - \mathbf{k}_4$ and $\mathbf{q} = \mathbf{k}_1 - \mathbf{k}_2$. This can facilitate our derivation of the RPA effective interactions, as will become clear in the following. The coefficient of interaction matrix $[W(\mathbf{k}_1, \mathbf{k}_2; \mathbf{k}_3, \mathbf{k}_4, \delta)]_{\tilde{a}_3 \tilde{a}_2}^{\tilde{a}_1 \tilde{a}_4}$ is antisymmetric with respect to exchanges of indices of two creation or annihilation operators in H_{int} ,

$$\begin{aligned} [W(\mathbf{k}_1, \mathbf{k}_2; \mathbf{k}_3, \mathbf{k}_4, \delta)]_{\tilde{a}_3 \tilde{a}_4}^{\tilde{a}_1 \tilde{a}_2} &= [W(\mathbf{k}_3, \mathbf{k}_4; \mathbf{k}_1, \mathbf{k}_2, \delta)]_{\tilde{a}_1 \tilde{a}_2}^{\tilde{a}_3 \tilde{a}_4} \\ &= - [W(\mathbf{k}_3, \mathbf{k}_2; \mathbf{k}_1, \mathbf{k}_4, \delta)]_{\tilde{a}_1 \tilde{a}_4}^{\tilde{a}_3 \tilde{a}_2} \\ &= - [W(\mathbf{k}_1, \mathbf{k}_4; \mathbf{k}_3, \mathbf{k}_2, \delta)]_{\tilde{a}_3 \tilde{a}_2}^{\tilde{a}_1 \tilde{a}_4}. \end{aligned} \quad (\text{C.7})$$

A2 Spin susceptibility and effective interactions within RPA

The effective electron-electron interaction can be attractive due to the exchange of spin and orbital fluctuations, even though the bare interaction is repulsive. To account for this effect, one calculates the effective interaction by summing up two-particle irreducible diagrams of different orders in the bare interaction, Eq. (C.6). More specifically, a tree diagram and a geometric series of the ladder and bubble diagrams are included in the RPA formalism.

A2.1 Tree diagram contribution

The tree diagram (shown in Fig. A3.1) contribution to the effective interaction is,

$$[\Gamma^{(1)}(\mathbf{k}, \mathbf{k}')]_{\tilde{a}_3 \tilde{a}_2}^{\tilde{a}_1 \tilde{a}_4} = \sum_{l,m=\{1,2\}} \left[\begin{pmatrix} e^{i\mathbf{k}\cdot\delta} & 0 \\ 0 & e^{i\mathbf{k}\cdot\delta} \end{pmatrix} [\tilde{W}(\delta)]_{\tilde{a}_3 \tilde{a}_2}^{\tilde{a}_1 \tilde{a}_4} \begin{pmatrix} e^{-i\mathbf{k}'\cdot\delta} & 0 \\ 0 & e^{i\mathbf{k}'\cdot\delta} \end{pmatrix} \right]_{lm} . \quad (\text{C.8})$$

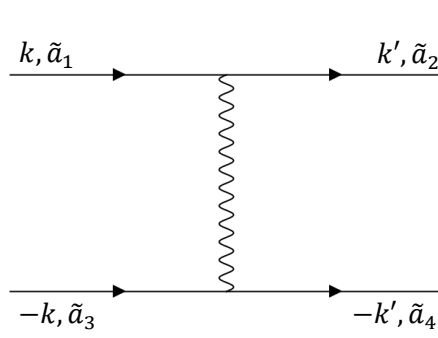


FIGURE A3.1: The first-order diagram that contributes to the effective interaction in the Cooper pair channel. Note that each interaction line carries four joint composite indices $\tilde{a}_i = \{a_i; s_i\}$.

A2.2 Ladder diagrams

Following standard Feynman rules, we can write down the second-order ladder diagram (shown in Fig. A3.2 (A)) contribution as,

$$\begin{aligned}
& [\Gamma_{lad}^{(2)}(\mathbf{k}, \mathbf{k}')]_{\tilde{a}_3 \tilde{a}_4}^{\tilde{a}_1 \tilde{a}_2} \\
&= \sum_{\delta_1, \delta_2} \sum_{\mathbf{p}} \sum_{\tilde{b}_i} [W(\mathbf{k}, -\mathbf{k}'; \mathbf{p} - (\mathbf{k} + \mathbf{k}'), \mathbf{p}, \delta_1)]_{\tilde{b}_1 \tilde{b}_2}^{\tilde{a}_1 \tilde{a}_2} \\
& \quad \times \left\{ -T \sum_n G_{\tilde{b}_4 \tilde{b}_1}(i\omega_n, \mathbf{p} - (\mathbf{k} + \mathbf{k}')) G_{\tilde{b}_2 \tilde{b}_3}(i\omega_n, \mathbf{p}) \right\} [W(\mathbf{p}, \mathbf{p} - (\mathbf{k} + \mathbf{k}'); -\mathbf{k}, \mathbf{k}', \delta_2)]_{\tilde{a}_3 \tilde{a}_4}^{\tilde{b}_3 \tilde{b}_4} \\
& \hspace{15em} \text{(C.9a)}
\end{aligned}$$

$$\begin{aligned}
&= \sum_{\delta_1, \delta_2} \sum_{\mathbf{p}} \sum_{\tilde{b}_i} \left([W_1(\delta_1)]_{\tilde{b}_1 \tilde{b}_2}^{\tilde{a}_1 \tilde{a}_2} e^{i(\mathbf{k} + \mathbf{k}') \cdot \delta_1} + [W_2(\delta_1)]_{\tilde{b}_1 \tilde{b}_2}^{\tilde{a}_1 \tilde{a}_2} e^{i(\mathbf{k} - \mathbf{p}) \cdot \delta_1} \right) \\
& \quad \times \sum_{\alpha, \beta} \frac{n_F(\xi_{\mathbf{p}}^\alpha) - n_F(\xi_{\mathbf{p} - (\mathbf{k} + \mathbf{k}')}^\beta)}{\xi_{\mathbf{p} - (\mathbf{k} + \mathbf{k}')}^\beta - \xi_{\mathbf{p}}^\alpha} \mathcal{F}_{\tilde{b}_3 \tilde{b}_4}^{\tilde{b}_1 \tilde{b}_2}(\alpha, \beta; \mathbf{p}, \mathbf{k} + \mathbf{k}') \\
& \quad \times \left([W_1(\delta_2)]_{\tilde{a}_3 \tilde{a}_4}^{\tilde{b}_3 \tilde{b}_4} e^{i(\mathbf{k} + \mathbf{k}') \cdot \delta_2} + [W_2(\delta_2)]_{\tilde{a}_3 \tilde{a}_4}^{\tilde{b}_3 \tilde{b}_4} e^{i(\mathbf{p} - \mathbf{k}') \cdot \delta_2} \right) \\
& \hspace{15em} \text{(C.9b)}
\end{aligned}$$

$$\begin{aligned}
&= \sum_{\delta_1, \delta_2} \sum_{\tilde{b}_i} \sum_{lm} \left[\begin{pmatrix} e^{i\mathbf{k} \cdot \delta_1} & 0 \\ 0 & e^{i\mathbf{k} \cdot \delta_1} \end{pmatrix} \begin{pmatrix} W_1(\delta_1) & 0 \\ 0 & W_2(\delta_1) \end{pmatrix} \right] \times \\
& \quad \underbrace{\sum_{\mathbf{p}} \sum_{\alpha, \beta} \frac{n_F(\xi_{\mathbf{p}}^\alpha) - n_F(\xi_{\mathbf{p} - (\mathbf{k} + \mathbf{k}')}^\beta)}{\xi_{\mathbf{p} - (\mathbf{k} + \mathbf{k}')}^\beta - \xi_{\mathbf{p}}^\alpha} \mathcal{F}_{\tilde{b}_3 \tilde{b}_4}^{\tilde{b}_1 \tilde{b}_2}(\alpha, \beta; \mathbf{p}, \mathbf{k} + \mathbf{k}') \begin{pmatrix} e^{i\mathbf{k}' \cdot \delta_1} & 0 \\ 0 & e^{-i\mathbf{p} \cdot \delta_1} \end{pmatrix} \begin{pmatrix} 1 & 1 \\ 1 & 1 \end{pmatrix} \begin{pmatrix} e^{i\mathbf{k} \cdot \delta_2} & 0 \\ 0 & e^{i\mathbf{p} \cdot \delta_2} \end{pmatrix}}_{[\chi(\mathbf{k}, -\mathbf{k}'; \delta_1, \delta_2)]_{\tilde{b}_3 \tilde{b}_4}^{\tilde{b}_1 \tilde{b}_2}} \\
& \quad \times \begin{pmatrix} W_1(\delta_2) & 0 \\ 0 & W_2(\delta_2) \end{pmatrix} \begin{pmatrix} e^{i\mathbf{k}' \cdot \delta_2} & 0 \\ 0 & e^{-i\mathbf{k}' \cdot \delta_2} \end{pmatrix} \Big]_{lm} \\
& \hspace{15em} \text{(C.9c)}
\end{aligned}$$

$$\begin{aligned}
&= \sum_{\delta_1, \delta_2} \sum_{\tilde{b}_i} \sum_{lm} \left[\begin{pmatrix} e^{i\mathbf{k} \cdot \delta_1} & 0 \\ 0 & e^{i\mathbf{k} \cdot \delta_1} \end{pmatrix} [\widetilde{W}(\delta_1)]_{\tilde{b}_1 \tilde{b}_2}^{\tilde{a}_1 \tilde{a}_2} \times [\chi(\mathbf{k}, -\mathbf{k}'; \delta_1, \delta_2)]_{\tilde{b}_3 \tilde{b}_4}^{\tilde{b}_1 \tilde{b}_2} \times [\widetilde{W}(\delta_2)]_{\tilde{a}_3 \tilde{a}_4}^{\tilde{b}_3 \tilde{b}_4} \begin{pmatrix} e^{i\mathbf{k}' \cdot \delta_2} & 0 \\ 0 & e^{-i\mathbf{k}' \cdot \delta_2} \end{pmatrix} \right]_{lm}. \\
& \hspace{15em} \text{(C.9d)}
\end{aligned}$$

Here, $[\chi(\mathbf{k}, -\mathbf{k}'; \delta_1, \delta_2)]_{\tilde{b}_3 \tilde{b}_4}^{\tilde{b}_1 \tilde{b}_2}$ is a generalized δ -dependent bare susceptibility matrix. $\mathcal{F}_{\tilde{b}_3 \tilde{b}_4}^{\tilde{b}_1 \tilde{b}_2}(\alpha, \beta; \mathbf{p}, \mathbf{q}) = \psi_{\tilde{b}_2}^\alpha(\mathbf{p}) [\psi_{\tilde{b}_3}^\alpha(\mathbf{p})]^* [\psi_{\tilde{b}_1}^\beta(\mathbf{p} - \mathbf{q})]^* \psi_{\tilde{b}_4}^\beta(\mathbf{p} - \mathbf{q})$, and is the form factor associated with the band-to-orbital transformations. In these equations, α and β are energy band labels (including the pseudospin). ξ_k^α is the α -th band dispersion, $\psi_b^\alpha(\mathbf{k})$ is the corresponding matrix element of the orbital-to-band transformation, and n_F is the Fermi-Dirac distribution function. $\widetilde{W}(\delta)$ and $\chi(\mathbf{k}, -\mathbf{k}'; \delta_1, \delta_2)$ are $N \times N$ matrices for given momenta with $N = 6 \times 6 \times 9 \times 2$, where 6×6 comes

from the two sets of composite indices $\{\tilde{a}_1, \tilde{a}_2\}$, each of which consists of 3 orbitals \otimes 2 spin species, 9 from the label of neighboring sites $\delta = \{0, \hat{x}, \hat{y}, -\hat{x}, -\hat{y}, \hat{x} + \hat{y}, -\hat{x} + \hat{y}, -\hat{x} - \hat{y}, \hat{x} - \hat{y}\}$, and 2 from the additional subspace label $l = \{1, 2\}$.

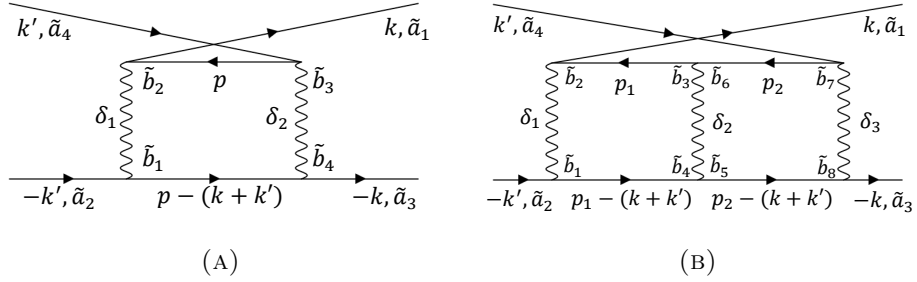


FIGURE A3.2: The second and the third order ladder diagrams. The internal momentum label, p , is a short-hand notation for frequency and momentum, both of which need to be summed over; on the other hand, for the external momenta, k and k' , we only consider zero frequency, i. e. retardation effect in the effective pairing interaction is neglected.

Similarly, the third-order ladder diagram (shown in Fig.A3.2 (B)) is,

$$\begin{aligned}
& [\Gamma_{lad}^{(3)}(\mathbf{k}, \mathbf{k}')]_{\tilde{a}_3 \tilde{a}_4}^{\tilde{a}_1 \tilde{a}_2} \\
&= \sum_{\delta_1, \delta_2, \delta_3} \sum_{\mathbf{p}_1, \mathbf{p}_2} \sum_{\tilde{b}_i} [W(\mathbf{k}, -\mathbf{k}'; \mathbf{p}_1 - (\mathbf{k} + \mathbf{k}'), \mathbf{p}_1, \delta_1)]_{\tilde{b}_1 \tilde{b}_2}^{\tilde{a}_1 \tilde{a}_2} \\
&\quad \times \left\{ -T \sum_n G_{\tilde{b}_4 \tilde{b}_1}(i\omega_n, \mathbf{p}_1 - (\mathbf{k} + \mathbf{k}')) G_{\tilde{b}_2 \tilde{b}_3}(i\omega_n, \mathbf{p}_1) \right\} \times [W(\mathbf{p}_1, \mathbf{p}_1 - (\mathbf{k} + \mathbf{k}'); \mathbf{p}_2 - (\mathbf{k} + \mathbf{k}'), \mathbf{p}_2, \delta_2)]_{\tilde{b}_5 \tilde{b}_6}^{\tilde{b}_3 \tilde{b}_4} \\
&\quad \times \left\{ -T \sum_n G_{\tilde{b}_8 \tilde{b}_5}(i\omega_n, \mathbf{p}_2 - (\mathbf{k} + \mathbf{k}')) G_{\tilde{b}_6 \tilde{b}_7}(i\omega_n, \mathbf{p}_2) \right\} \times [W(\mathbf{p}_2, \mathbf{p}_2 - (\mathbf{k} + \mathbf{k}'); -\mathbf{k}, \mathbf{k}', \delta_3)]_{\tilde{a}_3 \tilde{a}_4}^{\tilde{b}_7 \tilde{b}_8} \\
& \hspace{15em} \text{(C.10a)}
\end{aligned}$$

$$\begin{aligned}
&= \sum_{\delta_1, \delta_2, \delta_3} \sum_{\tilde{b}_i} \sum_{lm} \left[\begin{pmatrix} e^{i\mathbf{k} \cdot \delta_1} & 0 \\ 0 & e^{i\mathbf{k} \cdot \delta_1} \end{pmatrix} \times [\tilde{W}(\delta_1)]_{\tilde{b}_1 \tilde{b}_2}^{\tilde{a}_1 \tilde{a}_2} \times [\chi(\mathbf{k}, \mathbf{k}'; \delta_1, \delta_2)]_{\tilde{b}_3 \tilde{b}_4}^{\tilde{b}_1 \tilde{b}_2} \right. \\
&\quad \left. \times [\tilde{W}(\delta_2)]_{\tilde{b}_5 \tilde{b}_6}^{\tilde{b}_3 \tilde{b}_4} \times [\chi(\mathbf{k}, \mathbf{k}'; \delta_2, \delta_3)]_{\tilde{b}_7 \tilde{b}_8}^{\tilde{b}_5 \tilde{b}_6} \times [\tilde{W}(\delta_3)]_{\tilde{a}_3 \tilde{a}_4}^{\tilde{b}_7 \tilde{b}_8} \times \begin{pmatrix} e^{i\mathbf{k}' \cdot \delta_3} & 0 \\ 0 & e^{-i\mathbf{k}' \cdot \delta_3} \end{pmatrix} \right]_{lm}. \hspace{5em} \text{(C.10b)}
\end{aligned}$$

In summary, the ladder series can be calculated through a geometric sum form,

$$[\Gamma_{lad}^{RPA}(\mathbf{k}, \mathbf{k}')]_{\tilde{a}_3 \tilde{a}_4}^{\tilde{a}_1 \tilde{a}_2} \equiv \sum_{\delta_1, \delta_2} \sum_{l, m=\{1,2\}} \left[\begin{pmatrix} e^{i\mathbf{k}\cdot\delta_1} & 0 \\ 0 & e^{i\mathbf{k}\cdot\delta_1} \end{pmatrix} [\widetilde{W}(\delta_1) \chi^{RPA}(\mathbf{k}, -\mathbf{k}'; \delta_1, \delta_2) \widetilde{W}(\delta_2)]_{\tilde{a}_3 \tilde{a}_4}^{\tilde{a}_1 \tilde{a}_2} \begin{pmatrix} e^{i\mathbf{k}'\cdot\delta_2} & 0 \\ 0 & e^{-i\mathbf{k}'\cdot\delta_2} \end{pmatrix} \right]_{lm}, \quad (\text{C.11})$$

where χ^{RPA} is the generalized RPA spin susceptibility defined as,

$$\chi^{RPA}(\mathbf{k}, -\mathbf{k}'; \delta_1, \delta_2) = \chi(\mathbf{k}, -\mathbf{k}'; \delta_1, \delta_2) \frac{1}{1 - \widetilde{W} \chi(\mathbf{k}, -\mathbf{k}'; \delta_1, \delta_2)}. \quad (\text{C.12})$$

A2.3 Bubble diagrams

In a multi-orbital RPA calculation, as long as the bare interaction matrix vertex used is anti-symmetrized, there is a one-to-one correspondence between diagrams in the ladder and bubble series:

$$[\Gamma_{bubble}^{RPA}(\mathbf{k}, \mathbf{k}')]_{\tilde{a}_3 \tilde{a}_2}^{\tilde{a}_1 \tilde{a}_4} = -[\Gamma_{lad}^{RPA}(\mathbf{k}, -\mathbf{k}')]_{\tilde{a}_3 \tilde{a}_4}^{\tilde{a}_1 \tilde{a}_2}. \quad (\text{C.13})$$

In other words, the bubble sum is the anti-symmetrized ladder sum. This relation holds order by order in the bare interaction. To see that is the case for the 2nd order interaction, one can refer to Ref.[109]. This relation guarantees that the total effective interaction computed in the RPA is fully anti-symmetrized, as the bare interaction is.

A2.4 Summary

The total RPA effective interaction in Eq.10 of Chap. 5 can be obtained by summing up the bare interaction contribution in Eq. (C.8), and a geometric series of the ladder and bubble diagrams (in Eqs. (C.11) and (C.13)).

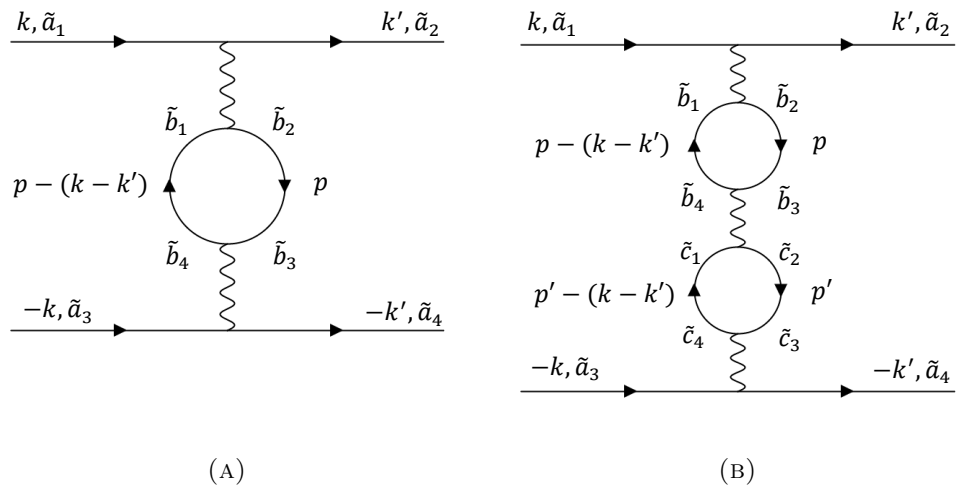


FIGURE A3.3: The second and the third order bubble diagrams.

Bibliography

- [1] H. Kamerlingh Onnes, “The resistance of pure mercury at helium temperatures,” *Commun. Phys. Lab. Univ. Leiden, b*, vol. 120, 1911.
- [2] J. Eisenstein, “Superconducting elements,” *Rev. Mod. Phys.*, vol. 26, pp. 277–291, Jul 1954.
- [3] J. Bardeen, L. N. Cooper, and J. R. Schrieffer, “Microscopic theory of superconductivity,” *Phys. Rev.*, vol. 106, pp. 162–164, Apr 1957.
- [4] L. N. Cooper, “Bound electron pairs in a degenerate fermi gas,” *Phys. Rev.*, vol. 104, pp. 1189–1190, Nov 1956.
- [5] D. D. Osheroff, R. C. Richardson, and D. M. Lee, “Evidence for a new phase of solid He^3 ,” *Phys. Rev. Lett.*, vol. 28, pp. 885–888, Apr 1972.
- [6] A. J. Leggett, “A theoretical description of the new phases of liquid ^3He ,” *Rev. Mod. Phys.*, vol. 47, pp. 331–414, Apr 1975.
- [7] D. Vollhardt and P. Wölfle, “The superfluid phases of ^3He ,” 1990.
- [8] J. G. Bednorz and K. A. Müller, “Possible high T_c superconductivity in the Ba-La-Cu-O system,” *Zeitschrift für Physik B Condensed Matter*, vol. 64, no. 2, pp. 189–193, 1986.
- [9] W. Hardy, D. Bonn, D. Morgan, R. Liang, and K. Zhang, “Precision measurements of the temperature dependence of λ in $\text{YBa}_2\text{Cu}_3\text{O}_{6.95}$: Strong evidence for nodes in the gap function,” *Physical Review Letters*, vol. 70, no. 25, p. 3999, 1993.
- [10] D. A. Wollman, D. J. Van Harlingen, W. C. Lee, D. M. Ginsberg, and A. J. Leggett, “Experimental determination of the superconducting pairing state

BIBLIOGRAPHY

- in YBCO from the phase coherence of YBCO-Pb dc SQUIDS,” *Phys. Rev. Lett.*, vol. 71, pp. 2134–2137, Sep 1993.
- [11] D. J. Van Harlingen, “Phase-sensitive tests of the symmetry of the pairing state in the high-temperature superconductors—evidence for $d_{x^2-y^2}$ symmetry,” *Rev. Mod. Phys.*, vol. 67, pp. 515–535, Apr 1995.
- [12] P. W. Anderson, “The resonating valence bond state in La_2CuO_4 and superconductivity,” *science*, vol. 235, no. 4793, pp. 1196–1198, 1987.
- [13] M. Sgrist and K. Ueda, “Phenomenological theory of unconventional superconductivity,” *Reviews of Modern physics*, vol. 63, no. 2, p. 239, 1991.
- [14] C. C. Tsuei and J. R. Kirtley, “Pairing symmetry in cuprate superconductors,” *Rev. Mod. Phys.*, vol. 72, pp. 969–1016, Oct 2000.
- [15] S. Raghu, S. A. Kivelson, and D. J. Scalapino, “Superconductivity in the repulsive hubbard model: An asymptotically exact weak-coupling solution,” *Phys. Rev. B*, vol. 81, p. 224505, Jun 2010.
- [16] M. R. Norman, “The challenge of unconventional superconductivity,” *Science*, vol. 332, no. 6026, pp. 196–200, 2011.
- [17] Y. Maeno, H. Hashimoto, K. Yoshida, S. Nishizaki, T. Fujita, J. Bednorz, and F. Lichtenberg, “Superconductivity in a layered perovskite without copper,” *nature*, vol. 372, no. 6506, pp. 532–534, 1994.
- [18] A. P. Mackenzie and Y. Maeno, “The superconductivity of Sr_2RuO_4 and the physics of spin-triplet pairing,” *Rev. Mod. Phys.*, vol. 75, pp. 657–712, May 2003.
- [19] Y. Maeno, T. M. Rice, and M. Sgrist, “The intriguing superconductivity of strontium ruthenate,” *Physics Today*, vol. 54, no. 1, pp. 42–47, 2001.
- [20] C. Bergemann, A. P. Mackenzie, S. R. Julian, D. Forsythe, and E. Ohmichi, “Quasi-two-dimensional fermi liquid properties of the unconventional superconductor Sr_2RuO_4 ,” *Advances in Physics*, vol. 52, no. 7, pp. 639–725, 2003.

BIBLIOGRAPHY

- [21] I. Eremin, D. Manske, S. Ovchinnikov, and J. Annett, “Unconventional superconductivity and magnetism in Sr_2RuO_4 and related materials,” *Annalen der Physik*, vol. 516, no. 3, pp. 149–174, 2004.
- [22] C. Kallin and A. J. Berlinsky, “Is Sr_2RuO_4 a chiral p-wave superconductor?,” *Journal of Physics: Condensed Matter*, vol. 21, p. 164210, mar 2009.
- [23] C. Kallin, “Chiral p-wave order in Sr_2RuO_4 ,” *Reports on Progress in Physics*, vol. 75, p. 042501, mar 2012.
- [24] Y. Maeno, S. Kittaka, T. Nomura, S. Yonezawa, and K. Ishida, “Evaluation of spin-triplet superconductivity in Sr_2RuO_4 ,” *Journal of the Physical Society of Japan*, vol. 81, no. 1, p. 011009, 2012.
- [25] C. Kallin and J. Berlinsky, “Chiral superconductors,” *Reports on Progress in Physics*, vol. 79, p. 054502, apr 2016.
- [26] A. P. Mackenzie, T. Scaffidi, C. W. Hicks, and Y. Maeno, “Even odder after twenty-three years: the superconducting order parameter puzzle of Sr_2RuO_4 ,” *npj Quantum Materials*, vol. 2, no. 1, pp. 1–9, 2017.
- [27] S. A. Kivelson, A. C. Yuan, B. Ramshaw, and R. Thomale, “A proposal for reconciling diverse experiments on the superconducting state in Sr_2RuO_4 ,” *npj Quantum Materials*, vol. 5, p. 43, Jun 2020.
- [28] A. J. Leggett and Y. Liu, “Symmetry properties of superconducting order parameter in Sr_2RuO_4 ,” *Journal of Superconductivity and Novel Magnetism*, vol. 34, no. 6, pp. 1647–1673, 2021.
- [29] Z. Mao, Y. Maeno, and H. Fukazawa, “Crystal growth of Sr_2RuO_4 ,” *Materials Research Bulletin*, vol. 35, no. 11, pp. 1813–1824, 2000.
- [30] A. Damascelli, D. H. Lu, K. M. Shen, N. P. Armitage, F. Ronning, D. L. Feng, C. Kim, Z.-X. Shen, T. Kimura, Y. Tokura, Z. Q. Mao, and Y. Maeno, “Fermi surface, surface states, and surface reconstruction in Sr_2RuO_4 ,” *Phys. Rev. Lett.*, vol. 85, pp. 5194–5197, Dec 2000.

BIBLIOGRAPHY

- [31] C. Bergemann, S. R. Julian, A. P. Mackenzie, S. Nishizaki, and Y. Maeno, “Detailed topography of the fermi surface of Sr_2RuO_4 ,” *Phys. Rev. Lett.*, vol. 84, pp. 2662–2665, Mar 2000.
- [32] A. Tamai, M. Zingl, E. Rozbicki, E. Cappelli, S. Riccò, A. de la Torre, S. McKeown Walker, F. Y. Bruno, P. D. C. King, W. Meevasana, M. Shi, M. Radović, N. C. Plumb, A. S. Gibbs, A. P. Mackenzie, C. Berthod, H. U. R. Strand, M. Kim, A. Georges, and F. Baumberger, “High-resolution photoemission on Sr_2RuO_4 reveals correlation-enhanced effective spin-orbit coupling and dominantly local self-energies,” *Phys. Rev. X*, vol. 9, p. 021048, Jun 2019.
- [33] A. P. Mackenzie, R. K. W. Haselwimmer, A. W. Tyler, G. G. Lonzarich, Y. Mori, S. Nishizaki, and Y. Maeno, “Extremely strong dependence of superconductivity on disorder in Sr_2RuO_4 ,” *Phys. Rev. Lett.*, vol. 80, pp. 161–164, Jan 1998.
- [34] G. M. Luke, Y. Fudamoto, K. M. Kojima, M. I. Larkin, J. Merrin, B. Nachumi, Y. J. Uemura, Y. Maeno, Z. Q. Mao, Y. Mori, H. Nakamura, and M. Sigrist, “Time-reversal symmetry-breaking superconductivity in Sr_2RuO_4 ,” *Nature*, vol. 394, pp. 558–561, aug 1998.
- [35] J. Xia, Y. Maeno, P. T. Beyersdorf, M. M. Fejer, and A. Kapitulnik, “High resolution polar kerr effect measurements of Sr_2RuO_4 : Evidence for broken time-reversal symmetry in the superconducting state,” *Phys. Rev. Lett.*, vol. 97, p. 167002, Oct 2006.
- [36] F. Kidwingira, J. D. Strand, D. J. V. Harlingen, and Y. Maeno, “Dynamical superconducting order parameter domains in Sr_2RuO_4 ,” *Science*, vol. 314, no. 5803, pp. 1267–1271, 2006.
- [37] J. R. Kirtley, C. Kallin, C. W. Hicks, E.-A. Kim, Y. Liu, K. A. Moler, Y. Maeno, and K. D. Nelson, “Upper limit on spontaneous supercurrents in Sr_2RuO_4 ,” *Phys. Rev. B*, vol. 76, p. 014526, Jul 2007.
- [38] C. W. Hicks, J. R. Kirtley, T. M. Lippman, N. C. Koshnick, M. E. Huber, Y. Maeno, W. M. Yuhasz, M. B. Maple, and K. A. Moler, “Limits on

BIBLIOGRAPHY

- superconductivity-related magnetization in Sr_2RuO_4 and $\text{PrOs}_4\text{Sb}_{12}$ from scanning SQUID microscopy,” *Phys. Rev. B*, vol. 81, p. 214501, Jun 2010.
- [39] P. J. Curran, S. J. Bending, W. M. Desoky, A. S. Gibbs, S. L. Lee, and A. P. Mackenzie, “Search for spontaneous edge currents and vortex imaging in Sr_2RuO_4 mesostructures,” *Phys. Rev. B*, vol. 89, p. 144504, Apr 2014.
- [40] S. Ray, A. Gibbs, S. Bending, P. Curran, E. Babaev, C. Baines, A. Mackenzie, and S. Lee, “Muon-spin rotation measurements of the vortex state in Sr_2RuO_4 : type-1.5 superconductivity, vortex clustering, and a crossover from a triangular to a square vortex lattice,” *Physical Review. B, Condensed matter and materials physics*, vol. 89, Mar. 2014.
- [41] C. Lupien, *Ultrasound attenuation in the unconventional superconductor Sr_2RuO_4* . PhD thesis, Univ. Toronto, 2002.
- [42] S. Ghosh, A. Shekhter, F. Jerzembeck, N. Kikugawa, D. A. Sokolov, M. Brando, A. P. Mackenzie, C. W. Hicks, and B. J. Ramshaw, “Thermodynamic evidence for a two-component superconducting order parameter in Sr_2RuO_4 ,” *Nature Physics*, vol. 17, pp. 199–204, Feb 2021.
- [43] S. Benhabib, C. Lupien, I. Paul, L. Berges, M. Dion, M. Nardone, A. Zitouni, Z. Mao, Y. Maeno, A. Georges, *et al.*, “Ultrasound evidence for a two-component superconducting order parameter in Sr_2RuO_4 ,” *Nature physics*, vol. 17, no. 2, pp. 194–198, 2021.
- [44] V. Grinenko, S. Ghosh, R. Sarkar, J.-C. Orain, A. Nikitin, M. Elender, D. Das, Z. Guguchia, F. Brückner, M. E. Barber, *et al.*, “Split superconducting and time-reversal symmetry-breaking transitions in Sr_2RuO_4 under stress,” *Nature Physics*, vol. 17, no. 6, pp. 748–754, 2021.
- [45] Y.-S. Li, N. Kikugawa, D. A. Sokolov, F. Jerzembeck, A. S. Gibbs, Y. Maeno, C. W. Hicks, J. Schmalian, M. Nicklas, and A. P. Mackenzie, “High-sensitivity heat-capacity measurements on Sr_2RuO_4 under uniaxial pressure,” *Proceedings of the National Academy of Sciences*, vol. 118, no. 10, p. e2020492118, 2021.

BIBLIOGRAPHY

- [46] J. F. Annett, G. Litak, B. L. Györfy, and K. I. Wysokiński, “Spin-orbit coupling and symmetry of the order parameter in strontium ruthenate,” *Phys. Rev. B*, vol. 73, p. 134501, Apr 2006.
- [47] M. W. Haverkort, I. S. Elfimov, L. H. Tjeng, G. A. Sawatzky, and A. Damascelli, “Strong spin-orbit coupling effects on the fermi surface of Sr_2RuO_4 and Sr_2RhO_4 ,” *Phys. Rev. Lett.*, vol. 101, p. 026406, Jul 2008.
- [48] C. M. Puetter and H.-Y. Kee, “Identifying spin-triplet pairing in spin-orbit coupled multi-band superconductors,” *EPL (Europhysics Letters)*, vol. 98, p. 27010, apr 2012.
- [49] C. N. Veenstra, Z.-H. Zhu, M. Raichle, B. M. Ludbrook, A. Nicolaou, B. Slomski, G. Landolt, S. Kittaka, Y. Maeno, J. H. Dil, I. S. Elfimov, M. W. Haverkort, and A. Damascelli, “Spin-orbital entanglement and the breakdown of singlets and triplets in Sr_2RuO_4 revealed by spin- and angle-resolved photoemission spectroscopy,” *Phys. Rev. Lett.*, vol. 112, p. 127002, Mar 2014.
- [50] C. G. Fatuzzo, M. Dantz, S. Fatale, P. Olalde-Velasco, N. E. Shaik, B. Dalla Piazza, S. Toth, J. Pellicciari, R. Fittipaldi, A. Vecchione, N. Kikugawa, J. S. Brooks, H. M. Rønnow, M. Grioni, C. Rüegg, T. Schmitt, and J. Chang, “Spin-orbit-induced orbital excitations in Sr_2RuO_4 and Ca_2RuO_4 : A resonant inelastic x-ray scattering study,” *Phys. Rev. B*, vol. 91, p. 199904, May 2015.
- [51] T. Scaffidi, J. C. Romers, and S. H. Simon, “Pairing symmetry and dominant band in Sr_2RuO_4 ,” *Phys. Rev. B*, vol. 89, p. 220510, Jun 2014.
- [52] Z. Wang, X. Wang, and C. Kallin, “Spin-orbit coupling and spin-triplet pairing symmetry in Sr_2RuO_4 ,” *Phys. Rev. B*, vol. 101, p. 064507, Feb 2020.
- [53] T. M. Rice and M. Sgrist, “ Sr_2RuO_4 : an electronic analogue of ^3He ?,” *Journal of Physics: Condensed Matter*, vol. 7, pp. L643–L648, nov 1995.
- [54] G. Baskaran, “Why is Sr_2RuO_4 not a high T_c superconductor? electron correlation, hund’s coupling and p -wave instability,” *Physica B: Condensed*

BIBLIOGRAPHY

- Matter*, vol. 223-224, pp. 490–495, 1996. Proceedings of the International Conference on Strongly Correlated Electron Systems.
- [55] K. Ishida, H. Mukuda, Y. Kitaoka, K. Asayama, Z. Mao, Y. Mori, and Y. Maeno, “Spin-triplet superconductivity in Sr_2RuO_4 identified by ^{17}O knight shift,” *Nature*, vol. 396, no. 6712, pp. 658–660, 1998.
- [56] K. Ishida, H. Mukuda, Y. Kitaoka, Z. Q. Mao, H. Fukazawa, and Y. Maeno, “Ru NMR probe of spin susceptibility in the superconducting state of Sr_2RuO_4 ,” *Phys. Rev. B*, vol. 63, p. 060507, Jan 2001.
- [57] J. A. Duffy, S. M. Hayden, Y. Maeno, Z. Mao, J. Kulda, and G. J. McIntyre, “Polarized-neutron scattering study of the cooper-pair moment in Sr_2RuO_4 ,” *Phys. Rev. Lett.*, vol. 85, pp. 5412–5415, Dec 2000.
- [58] K. D. Nelson, Z. Q. Mao, Y. Maeno, and Y. Liu, “Odd-parity superconductivity in Sr_2RuO_4 ,” *Science*, vol. 306, no. 5699, pp. 1151–1154, 2004.
- [59] N. Read and D. Green, “Paired states of fermions in two dimensions with breaking of parity and time-reversal symmetries and the fractional quantum hall effect,” *Phys. Rev. B*, vol. 61, pp. 10267–10297, Apr 2000.
- [60] M. Stone and R. Roy, “Edge modes, edge currents, and gauge invariance in $p_x + ip_y$ superfluids and superconductors,” *Physical Review B*, vol. 69, no. 18, p. 184511, 2004.
- [61] D. A. Ivanov, “Non-abelian statistics of half-quantum vortices in p -wave superconductors,” *Phys. Rev. Lett.*, vol. 86, pp. 268–271, Jan 2001.
- [62] C. Nayak, S. H. Simon, A. Stern, M. Freedman, and S. Das Sarma, “Non-abelian anyons and topological quantum computation,” *Rev. Mod. Phys.*, vol. 80, pp. 1083–1159, Sep 2008.
- [63] M. H. Fischer, T. Neupert, C. Platt, A. P. Schnyder, W. Hanke, J. Goryo, R. Thomale, and M. Sigrist, “Chiral d -wave superconductivity in SrPtAs ,” *Phys. Rev. B*, vol. 89, p. 020509, Jan 2014.

BIBLIOGRAPHY

- [64] R. Nandkishore, L. S. Levitov, and A. V. Chubukov, “Chiral superconductivity from repulsive interactions in doped graphene,” *Nature Physics*, vol. 8, no. 2, pp. 158–163, 2012.
- [65] L. Jiao, S. Howard, S. Ran, Z. Wang, J. O. Rodriguez, M. Sigrist, Z. Wang, N. P. Butch, and V. Madhavan, “Chiral superconductivity in heavy-fermion metal UTe_2 ,” *Nature*, vol. 579, no. 7800, pp. 523–527, 2020.
- [66] D. J. Thouless, M. Kohmoto, M. P. Nightingale, and M. den Nijs, “Quantized hall conductance in a two-dimensional periodic potential,” *Physical review letters*, vol. 49, no. 6, p. 405, 1982.
- [67] G. Volovik, “Fermion zero modes on vortices in chiral superconductors,” *Journal of Experimental and Theoretical Physics Letters*, vol. 70, no. 9, pp. 609–614, 1999.
- [68] W. Huang, E. Taylor, and C. Kallin, “Vanishing edge currents in non- p -wave topological chiral superconductors,” *Phys. Rev. B*, vol. 90, p. 224519, Dec 2014.
- [69] W. Huang, S. Lederer, E. Taylor, and C. Kallin, “Nontopological nature of the edge current in a chiral p -wave superconductor,” *Phys. Rev. B*, vol. 91, p. 094507, Mar 2015.
- [70] Y. Tada, W. Nie, and M. Oshikawa, “Orbital angular momentum and spectral flow in two-dimensional chiral superfluids,” *Phys. Rev. Lett.*, vol. 114, p. 195301, May 2015.
- [71] G. E. Volovik, “Orbital momentum of chiral superfluids and the spectral asymmetry of edge states,” *JETP letters*, vol. 100, no. 11, pp. 742–745, 2015.
- [72] W. Nie, W. Huang, and H. Yao, “Edge current and orbital angular momentum of chiral superfluids revisited,” *Phys. Rev. B*, vol. 102, p. 054502, Aug 2020.
- [73] A. Furusaki, M. Matsumoto, and M. Sigrist, “Spontaneous hall effect in a chiral p -wave superconductor,” *Phys. Rev. B*, vol. 64, p. 054514, Jul 2001.

BIBLIOGRAPHY

- [74] J. A. Sauls, “Surface states, edge currents, and the angular momentum of chiral p -wave superfluids,” *Phys. Rev. B*, vol. 84, p. 214509, Dec 2011.
- [75] M. Matsumoto and M. Sigrist, “Quasiparticle states near the surface and the domain wall in a $p_x \pm ip_y$ -wave superconductor,” *Journal of the Physical Society of Japan*, vol. 68, no. 3, pp. 994–1007, 1999.
- [76] H.-J. Kwon, V. M. Yakovenko, and K. Sengupta, “How to detect edge electron states in (TMTSF)₂X and Sr₂RuO₄ experimentally,” *Synthetic Metals*, vol. 133-134, pp. 27–31, 2003. Proceedings of the Yamada Conference LVI. The Fourth International Symposium on Crystalline Organic Metals, Superconductors and Ferromagnets (ISCOM 2001).
- [77] T. Scaffidi and S. H. Simon, “Large chern number and edge currents in Sr₂RuO₄,” *Phys. Rev. Lett.*, vol. 115, p. 087003, Aug 2015.
- [78] P. E. Ashby and C. Kallin, “Suppression of spontaneous supercurrents in a chiral p -wave superconductor,” *Physical Review B*, vol. 79, no. 22, p. 224509, 2009.
- [79] S. Lederer, W. Huang, E. Taylor, S. Raghu, and C. Kallin, “Suppression of spontaneous currents in Sr₂RuO₄ by surface disorder,” *Phys. Rev. B*, vol. 90, p. 134521, Oct 2014.
- [80] Y. Imai, K. Wakabayashi, and M. Sigrist, “Properties of edge states in a spin-triplet two-band superconductor,” *Phys. Rev. B*, vol. 85, p. 174532, May 2012.
- [81] Y. Imai, K. Wakabayashi, and M. Sigrist, “Topological and edge state properties of a three-band model for Sr₂RuO₄,” *Phys. Rev. B*, vol. 88, p. 144503, Oct 2013.
- [82] A. Bouhon and M. Sigrist, “Current inversion at the edges of a chiral p -wave superconductor,” *Phys. Rev. B*, vol. 90, p. 220511, Dec 2014.
- [83] S.-I. Suzuki and Y. Asano, “Spontaneous edge current in a small chiral superconductor with a rough surface,” *Phys. Rev. B*, vol. 94, p. 155302, Oct 2016.

BIBLIOGRAPHY

- [84] C. W. Hicks, D. O. Brodsky, E. A. Yelland, A. S. Gibbs, J. A. Bruin, M. E. Barber, S. D. Edkins, K. Nishimura, S. Yonezawa, Y. Maeno, *et al.*, “Strong increase of T_c of Sr_2RuO_4 under both tensile and compressive strain,” *Science*, vol. 344, no. 6181, pp. 283–285, 2014.
- [85] A. Steppke, L. Zhao, M. E. Barber, T. Scaffidi, F. Jerzembeck, H. Rosner, A. S. Gibbs, Y. Maeno, S. H. Simon, A. P. Mackenzie, and C. W. Hicks, “Strong peak in T_c of Sr_2RuO_4 under uniaxial pressure,” *Science*, vol. 355, no. 6321, p. eaaf9398, 2017.
- [86] C. A. Watson, A. S. Gibbs, A. P. Mackenzie, C. W. Hicks, and K. A. Moler, “Micron-scale measurements of low anisotropic strain response of local T_c in Sr_2RuO_4 ,” *Phys. Rev. B*, vol. 98, p. 094521, Sep 2018.
- [87] A. M. Clogston, “Upper limit for the critical field in hard superconductors,” *Phys. Rev. Lett.*, vol. 9, pp. 266–267, Sep 1962.
- [88] K. Deguchi, M. A. Tanatar, Z. Mao, T. Ishiguro, and Y. Maeno, “Superconducting double transition and the upper critical field limit of Sr_2RuO_4 in parallel magnetic fields,” *Journal of the Physical Society of Japan*, vol. 71, no. 12, pp. 2839–2842, 2002.
- [89] S. Yonezawa, T. Kajikawa, and Y. Maeno, “First-order superconducting transition of Sr_2RuO_4 ,” *Phys. Rev. Lett.*, vol. 110, p. 077003, Feb 2013.
- [90] S. Yonezawa, T. Kajikawa, and Y. Maeno, “Specific-heat evidence of the first-order superconducting transition in Sr_2RuO_4 ,” *Journal of the Physical Society of Japan*, vol. 83, no. 8, p. 083706, 2014.
- [91] S. Kittaka, A. Kasahara, T. Sakakibara, D. Shibata, S. Yonezawa, Y. Maeno, K. Tenya, and K. Machida, “Sharp magnetization jump at the first-order superconducting transition in Sr_2RuO_4 ,” *Phys. Rev. B*, vol. 90, p. 220502, Dec 2014.
- [92] A. Pustogow, Y. Luo, A. Chronister, Y.-S. Su, D. Sokolov, F. Jerzembeck, A. Mackenzie, C. Hicks, N. Kikugawa, S. Raghu, E. Bauer, and S. Brown, “Constraints on the superconducting order parameter in Sr_2RuO_4

BIBLIOGRAPHY

- from oxygen-17 nuclear magnetic resonance,” *Nature*, vol. 574, no. 7776, pp. 72–75, 2019.
- [93] K. Ishida, M. Manago, K. Kinjo, and Y. Maeno, “Reduction of the ^{17}O knight shift in the superconducting state and the heat-up effect by nmr pulses on Sr_2RuO_4 ,” *Journal of the Physical Society of Japan*, vol. 89, no. 3, p. 034712, 2020.
- [94] A. Chronister, A. Pustogow, N. Kikugawa, D. A. Sokolov, F. Jerzembeck, C. W. Hicks, A. P. Mackenzie, E. D. Bauer, and S. E. Brown, “Evidence for even parity unconventional superconductivity in Sr_2RuO_4 ,” *Proceedings of the National Academy of Sciences*, vol. 118, no. 25, p. e2025313118, 2021.
- [95] A. N. Petsch, M. Zhu, M. Enderle, Z. Q. Mao, Y. Maeno, I. I. Mazin, and S. M. Hayden, “Reduction of the spin susceptibility in the superconducting state of Sr_2RuO_4 observed by polarized neutron scattering,” *Phys. Rev. Lett.*, vol. 125, p. 217004, Nov 2020.
- [96] W. Huang and Z. Wang, “Possibility of mixed helical p -wave pairings in Sr_2RuO_4 ,” *Phys. Rev. Research*, vol. 3, p. L042002, Oct 2021.
- [97] A. T. Rømer, P. J. Hirschfeld, and B. M. Andersen, “Superconducting state of Sr_2RuO_4 in the presence of longer-range coulomb interactions,” *Phys. Rev. B*, vol. 104, p. 064507, Aug 2021.
- [98] J. Clepkens, A. W. Lindquist, X. Liu, and H.-Y. Kee, “Higher angular momentum pairings in interorbital shadowed-triplet superconductors: Application to Sr_2RuO_4 ,” *Phys. Rev. B*, vol. 104, p. 104512, Sep 2021.
- [99] A. J. Leggett *et al.*, *Quantum liquids: Bose condensation and Cooper pairing in condensed-matter systems*. Oxford university press, 2006.
- [100] M. Sigrist, D. Agterberg, A. Furusaki, C. Honerkamp, K. Ng, T. Rice, and M. Zhitomirsky, “Phenomenology of the superconducting state in Sr_2RuO_4 ,” *Physica C: Superconductivity*, vol. 317-318, pp. 134–141, 1999.

BIBLIOGRAPHY

- [101] K. K. Ng and M. Sigrist, “The role of spin-orbit coupling for the superconducting state in Sr_2RuO_4 ,” *EPL (Europhysics Letters)*, vol. 49, no. 4, p. 473, 2000.
- [102] K.-K. Ng and M. Sigrist, “The role of spin-orbit coupling for the superconductivity in Sr_2RuO_4 ,” *Physica B: Condensed Matter*, vol. 281-282, pp. 969–970, 2000.
- [103] Y. Yanase and M. Ogata, “Microscopic identification of the d-vector in triplet superconductor Sr_2RuO_4 ,” *Journal of the Physical Society of Japan*, vol. 72, no. 3, pp. 673–687, 2003.
- [104] S. Raghu, A. Kapitulnik, and S. A. Kivelson, “Hidden quasi-one-dimensional superconductivity in Sr_2RuO_4 ,” *Phys. Rev. Lett.*, vol. 105, p. 136401, Sep 2010.
- [105] Y. Yanase, S. Takamatsu, and M. Udagawa, “Spin-orbit coupling and multiple phases in spin-triplet superconductor Sr_2RuO_4 ,” *Journal of the Physical Society of Japan*, vol. 83, no. 6, p. 061019, 2014.
- [106] L.-D. Zhang, W. Huang, F. Yang, and H. Yao, “Superconducting pairing in Sr_2RuO_4 from weak to intermediate coupling,” *Phys. Rev. B*, vol. 97, p. 060510(R), Feb 2018.
- [107] A. T. Rømer, D. D. Scherer, I. M. Eremin, P. J. Hirschfeld, and B. M. Andersen, “Knight shift and leading superconducting instability from spin fluctuations in Sr_2RuO_4 ,” *Phys. Rev. Lett.*, vol. 123, p. 247001, Dec 2019.
- [108] H. S. Røising, T. Scaffidi, F. Flicker, G. F. Lange, and S. H. Simon, “Superconducting order of Sr_2RuO_4 from a three-dimensional microscopic model,” *Phys. Rev. Research*, vol. 1, p. 033108, Nov 2019.
- [109] T. Scaffidi, *Unconventional superconductivity in strontium ruthenate*. PhD thesis, University of Oxford, 2016.
- [110] R. Willa, “Symmetry-mixed bound-state order,” *Phys. Rev. B*, vol. 102, p. 180503(R), Nov 2020.

BIBLIOGRAPHY

- [111] K. Deguchi, Z. Q. Mao, H. Yaguchi, and Y. Maeno, “Gap structure of the spin-triplet superconductor Sr_2RuO_4 determined from the field-orientation dependence of the specific heat,” *Phys. Rev. Lett.*, vol. 92, p. 047002, Jan 2004.
- [112] E. Hassinger, P. Bourgeois-Hope, H. Taniguchi, S. René de Cotret, G. Grissonnanche, M. S. Anwar, Y. Maeno, N. Doiron-Leyraud, and L. Taillefer, “Vertical line nodes in the superconducting gap structure of Sr_2RuO_4 ,” *Phys. Rev. X*, vol. 7, p. 011032, Mar 2017.
- [113] R. Sharma, S. D. Edkins, Z. Wang, A. Kostin, C. Sow, Y. Maeno, A. P. Mackenzie, J. C. S. Davis, and V. Madhavan, “Momentum-resolved superconducting energy gaps of Sr_2RuO_4 from quasiparticle interference imaging,” *Proceedings of the National Academy of Sciences*, vol. 117, no. 10, pp. 5222–5227, 2020.
- [114] P. Steffens, Y. Sidis, J. Kulda, Z. Q. Mao, Y. Maeno, I. I. Mazin, and M. Braden, “Spin fluctuations in Sr_2RuO_4 from polarized neutron scattering: Implications for superconductivity,” *Phys. Rev. Lett.*, vol. 122, p. 047004, Feb 2019.
- [115] R. Willa, M. Hecker, R. M. Fernandes, and J. Schmalian, “Inhomogeneous time-reversal symmetry breaking in Sr_2RuO_4 ,” *Phys. Rev. B*, vol. 104, p. 024511, Jul 2021.
- [116] A. C. Yuan, E. Berg, and S. A. Kivelson, “Strain-induced time reversal breaking and half quantum vortices near a putative superconducting tetracritical point in Sr_2RuO_4 ,” *Phys. Rev. B*, vol. 104, p. 054518, Aug 2021.
- [117] J. Jang, D. Ferguson, V. Vakaryuk, R. Budakian, S. Chung, P. Goldbart, and Y. Maeno, “Observation of half-height magnetization steps in Sr_2RuO_4 ,” *Science*, vol. 331, no. 6014, pp. 186–188, 2011.
- [118] A. T. Rømer and B. M. Andersen, “Fluctuation-driven superconductivity in Sr_2RuO_4 from weak repulsive interactions,” *Modern Physics Letters B*, vol. 34, no. 19n20, p. 2040052, 2020.

BIBLIOGRAPHY

- [119] A. T. Rømer, T. A. Maier, A. Kreisel, P. J. Hirschfeld, and B. M. Andersen, “Leading superconducting instabilities in three-dimensional models for Sr_2RuO_4 ,” *Phys. Rev. Research*, vol. 4, p. 033011, Jul 2022.
- [120] Q. H. Wang, C. Platt, Y. Yang, C. Honerkamp, F. C. Zhang, W. Hanke, T. M. Rice, and R. Thomale, “Theory of superconductivity in a three-orbital model of Sr_2RuO_4 ,” *EPL (Europhysics Letters)*, vol. 104, p. 17013, oct 2013.
- [121] W.-S. Wang, C.-C. Zhang, F.-C. Zhang, and Q.-H. Wang, “Theory of chiral p -wave superconductivity with near nodes for Sr_2RuO_4 ,” *Phys. Rev. Lett.*, vol. 122, p. 027002, Jan 2019.
- [122] S. Raghu, E. Berg, A. V. Chubukov, and S. A. Kivelson, “Effects of longer-range interactions on unconventional superconductivity,” *Phys. Rev. B*, vol. 85, p. 024516, Jan 2012.
- [123] M. Sigrist, “Introduction to unconventional superconductivity,” in *AIP Conference Proceedings*, vol. 789, pp. 165–243, American Institute of Physics, 2005.
- [124] S. Ghosh, T. G. Kiely, A. Shekhter, F. Jerzembeck, N. Kikugawa, D. A. Sokolov, A. P. Mackenzie, and B. J. Ramshaw, “Strong increase in ultrasound attenuation below T_c in Sr_2RuO_4 : Possible evidence for domains,” 2021.
- [125] V. Sunko, E. Abarca Morales, I. Marković, M. E. Barber, D. Milosavljević, F. Mazzola, D. A. Sokolov, N. Kikugawa, C. Cacho, P. Dudin, *et al.*, “Direct observation of a uniaxial stress-driven lifshitz transition in Sr_2RuO_4 ,” *npj Quantum Materials*, vol. 4, no. 1, pp. 1–7, 2019.
- [126] S. Nishizaki, Y. Maeno, and Z. Mao, “Effect of impurities on the specific heat of the spin-triplet superconductor Sr_2RuO_4 ,” *Journal of Low Temperature Physics*, vol. 117, pp. 1581–1585, 1999.
- [127] S. Nishizaki, Y. Maeno, and M. Zhiqiang, “Changes in the superconducting state of Sr_2RuO_4 under magnetic fields probed by specific heat,” *Journal of the Physical Society of Japan*, vol. 69, pp. 572–578, Feb. 2000.

BIBLIOGRAPHY

- [128] K. Deguchi, Z. Q. Mao, and Y. Maeno, “Determination of the superconducting gap structure in all bands of the spin-triplet superconductor Sr_2RuO_4 ,” *Journal of the Physical Society of Japan*, vol. 73, no. 5, pp. 1313–1321, 2004.
- [129] S. Kittaka, S. Nakamura, T. Sakakibara, N. Kikugawa, T. Terashima, S. Uji, D. A. Sokolov, A. P. Mackenzie, K. Irie, Y. Tsutsumi, *et al.*, “Searching for gap zeros in Sr_2RuO_4 via field-angle-dependent specific-heat measurement,” *Journal of the Physical Society of Japan*, vol. 87, no. 9, p. 093703, 2018.
- [130] M. Suzuki, M. A. Tanatar, N. Kikugawa, Z. Q. Mao, Y. Maeno, and T. Ishiguro, “Universal heat transport in Sr_2RuO_4 ,” *Phys. Rev. Lett.*, vol. 88, p. 227004, May 2002.
- [131] C. Lupien, W. MacFarlane, C. Proust, L. Taillefer, Z. Mao, and Y. Maeno, “Ultrasound attenuation in Sr_2RuO_4 : An angle-resolved study of the superconducting gap function,” *Physical review letters*, vol. 86, no. 26, p. 5986, 2001.
- [132] J. F. Dodaro, Z. Wang, and C. Kallin, “Effects of deep superconducting gap minima and disorder on residual thermal transport in Sr_2RuO_4 ,” *Phys. Rev. B*, vol. 98, p. 214520, Dec 2018.
- [133] N. Schopohl and K. Maki, “Quasiparticle spectrum around a vortex line in a d-wave superconductor,” *Phys. Rev. B*, vol. 52, pp. 490–493, Jul 1995.
- [134] M. Ichioka, N. Hayashi, N. Enomoto, and K. Machida, “Vortex structure in d-wave superconductors,” *Phys. Rev. B*, vol. 53, pp. 15316–15326, Jun 1996.
- [135] M. Ichioka, A. Hasegawa, and K. Machida, “Vortex lattice effects on low-energy excitations in d-wave and s-wave superconductors,” *Phys. Rev. B*, vol. 59, pp. 184–187, Jan 1999.
- [136] M. Ichioka and K. Machida, “Field dependence of the vortex structure in chiral p-wave superconductors,” *Phys. Rev. B*, vol. 65, p. 224517, Jun 2002.
- [137] M. Roig, A. T. Rømer, A. Kreisel, P. J. Hirschfeld, and B. M. Andersen, “Superconductivity in multiorbital systems with repulsive interactions: Hund’s pairing vs. spin-fluctuation pairing,” 2022.

BIBLIOGRAPHY

- [138] X. Wang, Z. Wang, and C. Kallin, “Higher angular momentum pairing states in Sr_2RuO_4 in the presence of longer-range interactions,” *Phys. Rev. B*, vol. 106, p. 134512, Oct 2022.
- [139] O. Gingras, R. Nourafkan, A. M. S. Tremblay, and M. Côté, “Superconducting symmetries of Sr_2RuO_4 from first-principles electronic structure,” *Phys. Rev. Lett.*, vol. 123, p. 217005, Nov 2019.
- [140] J. Clepkens, A. W. Lindquist, and H.-Y. Kee, “Shadowed triplet pairings in hund’s metals with spin-orbit coupling,” *Phys. Rev. Research*, vol. 3, p. 013001, Jan 2021.
- [141] A. T. Rømer, T. A. Maier, A. Kreisel, I. Eremin, P. J. Hirschfeld, and B. M. Andersen, “Pairing in the two-dimensional hubbard model from weak to strong coupling,” *Phys. Rev. Research*, vol. 2, p. 013108, Jan 2020.
- [142] M. Tsuchiizu, Y. Yamakawa, S. Onari, Y. Ohno, and H. Kontani, “Spin-triplet superconductivity in Sr_2RuO_4 due to orbital and spin fluctuations: Analyses by two-dimensional renormalization group theory and self-consistent vertex-correction method,” *Phys. Rev. B*, vol. 91, p. 155103, Apr 2015.
- [143] S.-O. Kaba and D. Sénéchal, “Group-theoretical classification of superconducting states of strontium ruthenate,” *Phys. Rev. B*, vol. 100, p. 214507, Dec 2019.
- [144] A. Ramires and M. Sigrist, “Superconducting order parameter of Sr_2RuO_4 : A microscopic perspective,” *Phys. Rev. B*, vol. 100, p. 104501, Sep 2019.
- [145] W. Huang, Y. Zhou, and H. Yao, “Exotic cooper pairing in multiorbital models of Sr_2RuO_4 ,” *Phys. Rev. B*, vol. 100, p. 134506, Oct 2019.
- [146] H. G. Suh, H. Menke, P. M. R. Brydon, C. Timm, A. Ramires, and D. F. Agterberg, “Stabilizing even-parity chiral superconductivity in Sr_2RuO_4 ,” *Phys. Rev. Research*, vol. 2, p. 032023(R), Jul 2020.
- [147] A. A. Abrikosov, L. P. Gorkov, and I. E. Dzyaloshinski, *Methods of quantum field theory in statistical physics*. Courier Corporation, 2012.

BIBLIOGRAPHY

- [148] N. Kopnin, *Theory of nonequilibrium superconductivity*, vol. 110. Oxford University Press, 2001.
- [149] T. Kita, *Statistical Mechanics of Superconductivity*. Springer, 2015.
- [150] A. Andreev, “The thermal conductivity of the intermediate state in superconductors,” vol. 46, no. 5, pp. 1823–1828, 1964.
- [151] C. Bruder, “Andreev scattering in anisotropic superconductors,” *Phys. Rev. B*, vol. 41, pp. 4017–4032, Mar 1990.
- [152] N. Schopohl, “Transformation of the Eilenberger equations of superconductivity to a scalar Riccati equation,” 1998.
- [153] X. Wang, Z. Wang, and C. Kallin, “Spontaneous edge current in higher chirality superconductors,” *Phys. Rev. B*, vol. 98, p. 094501, Sep 2018.
- [154] D. F. Agterberg, “Vortex lattice structures of Sr_2RuO_4 ,” *Phys. Rev. Lett.*, vol. 80, pp. 5184–5187, Jun 1998.
- [155] J. A. Sauls, H. Wu, and S. B. Chung, “Anisotropy and strong-coupling effects on the collective mode spectrum of chiral superconductors: application to Sr_2RuO_4 ,” *Frontiers in Physics*, vol. 3, p. 36, 2015.
- [156] A. Chubukov, “Pairing mechanism in Fe-based superconductors,” *Annu. Rev. Condens. Matter Phys.*, vol. 3, no. 1, pp. 57–92, 2012.